OSMOTIC SWELLING BEHAVIOR OF IONIC MICROGELS

A Dissertation
Submitted to the Graduate Faculty
of the
North Dakota State University
of Agriculture and Applied Science

By

Mohammed Obaid Alziyadi

In Partial Fulfillment of the Requirements
for the Degree of
DOCTOR OF PHILOSOPHY

Major Department:
Physics

November 2020

Fargo, North Dakota

NORTH DAKOTA STATE UNIVERSITY

Graduate School

Title

OSMOTIC SWELLING BEHAVIOR OF IONIC MICROGELS

By

Mohammed Obaid Alziyadi

The supervisory committee certifies that this dissertation complies with North Dakota State University's regulations and meets the accepted standards for the degree of

DOCTOR OF PHILOSOPHY

SUPERVISORY COMMITTEE:

Prof. Alan Denton
Chair

Prof. Sylvio May

Prof. Andrew B. Croll

Prof. Andriy Voronov

Approved:

November 19, 2020
Date

Prof. Sylvio May
Department Chair

ABSTRACT

This dissertation studies the thermodynamic and structural properties of aqueous dispersions of ionic microgels – soft colloidal particles composed of cross-linked polymer gels that swell in a good solvent. Starting from a coarse-grained model of microgel particles, we perform computer simulations and theoretical calculations using two complementary implementations of Poisson-Boltzmann (PB) theory. Within the framework of a cell model, the nonlinear PB equation is exactly solved and used to compute counterion distributions and osmotic pressures. By varying the free energy with respect to microgel size, we obtain exact statistical mechanical relations for the electrostatic component of the single-particle osmotic pressure. Explicit results are presented for equilibrium swelling ratios of charged microcapsules and of charged cylindrical and spherical microgels with fixed charge uniformly distributed over the surface or volume of the particle. Molecular dynamics simulations validate the theoretical findings. In the second method, within a one-component model framework, based on a linear-response approximation for effective electrostatic interactions, we develop Monte Carlo (MC) simulations to compute the equilibrium swelling ratio, bulk osmotic pressure, radial distribution function, and static structure factor.

Results presented in this dissertation demonstrate that swelling of ionic microgels increases with increasing microgel charge and decreases with increasing concentration of salt and microgels. In addition, results demonstrate that the microion distributions and osmotic pressure determine equilibrium swelling of microgels. Cell model predictions for bulk osmotic pressure agree well with data from MC simulations of the one-component model. The MC simulations also provide access to structural properties and to swelling behavior of microgels in highly concentrated suspensions. Taken together, results obtained in this work provide insight into factors of importance for practical use of microgels as drug delivery systems, in tissue engineering, and for other biomedical applications.

ACKNOWLEDGEMENTS

I would like to express my deep and sincere gratitude to my research supervisor, Prof. Alan Denton, for his guidance, patience, and support throughout the years of my Ph.D. I came with no programming experience, but because of his guidance, I was able to learn several computer languages. Prof. Denton has been a source of constant advice to me in the development of this Ph.D., and to whom I will continue to seek input from in my future research. He has been exceedingly generous with his time and expertise in the process of developing this dissertation. It has been a great pleasure and honor to have Prof. Denton as a research advisor.

I am also thankful to my committee members: Prof. Sylvio May, Prof. Andriy Voronov, and Dr. Andrew B. Croll. I thank them for being willing to be a part of the committee for my Doctoral dissertation and for their support and advice. I would also like to thank my group of colleagues who have been a source of vibrant discussions. I would also like to expand my deepest gratitude to my supportive family: my parents, my wife, brothers, and sisters who kept me always in their prayers. Lastly, I am grateful to Dr. Hassan Alsuhabi, Dr. Sultan Kadasah, Dr. Mohammed Alshareef, Dr. Fouad Khalawi, Dr. Faez Alotaibi, Dr. Marran Aldossri, and Dr. Fasial Alotaibi for the unceasing encouragement, support, and attentiveness.

DEDICATION

I dedicate this dissertation to my late grandfather, who passed away 11 years ago, yet whose encouraging words have remained to be my inspiration to chase my dreams. I am indebted to the foundation he has laid in my life.

TABLE OF CONTENTS

LIST OF TABLES

LIST OF FIGURES

1. INTRODUCTION AND BACKGROUND

1.1. Ionic Microgels

Microgels are soft colloidal particles, with dimensions < 1 μm, each comprised of a cross-linked polymer network, as shown in Figure 1.1. Common examples of microgels are found in inks, cosmetics, and paints. When microgels are dispersed in a polar solvent, such as water, their structural properties, such as equilibrium swelling and elasticity, can be tuned by adjusting pH, temperature, magnetic and electric fields, flow rates, or osmotic pressure [1–3]. Many advanced methods have been developed to synthesize a wide range of sophisticated morphologies of microgels, including spherical microgels [4–7], core-shell structures [8–10], microgels containing nanoparticles or microcapsules [11–13], and cylindrical microgels [14, 15]. These microgel particles exhibit significantly different mechanical, optical, and swelling properties relative to bulk gels, thus appearing promising in designing particles for biomedical and environmental applications. In particular, temperature-responsive microgels, such as poly(N-isopropylacrylamide) (PNIPAM) microgels, have attracted significant research interest due to their ability to change their size and surface charge as a function of temperature [16, 17]. These thermally switchable properties have been applied in drug delivery systems (to easily access small areas of the human body, e.g., the cytoplasm of cells) [18, 19]. These rich thermodynamic properties are the heart of why microgels are important materials in science and technology [2, 20].

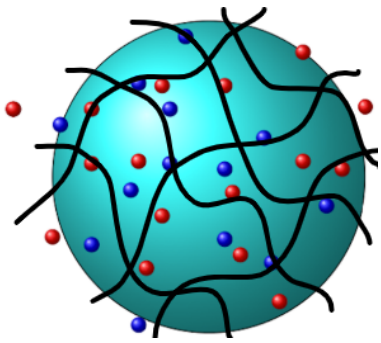

Figure 1.1. Schematic drawing of an ionic microgel (large cyan sphere), with cross-linked polymer chains shown to suggest internal structure, surrounded by oppositely charged counterions (small red spheres) and coions (small blue spheres).

Ionic microgels are polyelectrolytes or ionizable polymers that dissolve in a solvent, through dissociation of small-ions, called counterions, leaving the polymer chains with negative charges. Equilibrium swelling of microgels is influenced by several interparticle interactions. Besides van der Waals, hydrophobic, and hydrogen bonding, electrostatic interactions play a very important role in determining ionic microgel equilibrium size [2]. A charged microgel tends to swell not only from absorbing solvent, but also because of the repulsive interactions between bare fixed charges along its polymer chains (backbones). The fixed charges, whether positive or negative, cause an imbalance between the ion distributions inside and outside the microgel, thereby inducing swelling or deswell. Changing the salt concentration or the pH level in the system affects the dissociation, and therefore changes the fractional charge of the polymer chain. In brief, one can control the ionic microgel size by controlling the counterion distribution, salt concentration, and the pH in the system. It is worth noting that the correlations between multivalent counterions may be important in studying the swelling of some ionic microgels. However, the focus of this work is on modeling ionic microgels with monovalent counterions only.

Aside from electrostatic interactions, elastic properties of microgels also play an essential role in the swelling process since, type and density of cross-linked influence the equilibrium polymer network size [21]. In a swollen state, microgel particles are soft and easily deformed, while in a dry state, microgels behave very much like hard spheres. The cross-links of microgel particles are formed either by chemical or physical interactions. Chemical cross-linked are usually covalent bonds, while physical cross-links are hydrogen bonds, hydrophobic, or ionic interactions. Physical cross-links are more sensitive to external stimuli. Poly(N-isopropylacrylamide) (PNIPAM) microgels are perhaps the most well-known and well-characterized microgel particles [2]. They were first synthesized in the 1950s [22] and has attracted considerable research interest because of several advantages: hydrophilicity, flexibility, high water absorptivity, and their volume phase transition temperature close to human body temperature, which makes them an ideal smart drug delivery system [2, 23].

1.2. Osmotic Pressure

The concept of osmotic pressure has long been used to explain the swelling behavior of ionic microgels [2]. It is best to describe the concept of osmotic pressure through the osmosis phenomenon. Generally, osmosis is defined as the flow of solution across a semipermeable membrane that blocks the transport of solute through it, so only smaller solvent molecules are allowed to flow

through. Osmosis is an important phenomenon in the biological systems, as well as in water purification, desalination, and many other biochemical processes.

Figure 1.2 illustrates the principle of the osmosis phenomenon. Consider a beaker containing a homogeneous mixture solution of both macromolecules and solvent (water) and a semipermeable membrane that prevents macromolecules, such as microgel particles, from passing through. Solvent molecules and ions (counterion and coions) can penetrate through the semipermeable membrane freely. If only macromolecules exist on one side of the membrane, the surrounding solvent will diffuse across the membrane due to the difference in concentrations. The solvent flow will continue until it reaches its limit due to the pressure difference across the membrane. Under these conditions, equilibrium is established, and pressure is exerted on the macromolecules-rich side of the membrane to stop the flow of solvent. This additional pressure exerted on the membrane is called osmotic pressure [24].

The effect of the microions through the osmotic pressure they exert strongly influences the swelling of ionic microgel particles. In Chapter 4, we drive an exact expression for the electrostatic contribution to the osmotic pressure across the periphery of a microcapsule and of spherical and cylindrical ionic microgels.

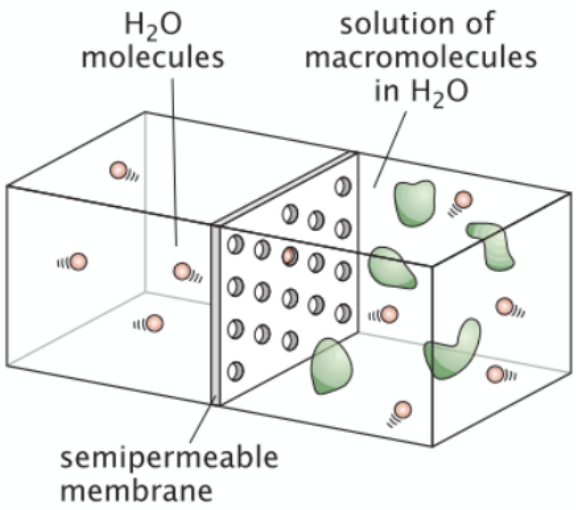

Figure 1.2. Illustration of the osmosis phenomenon. Reprinted with permission from ref. [25].

1.3. Swelling Behavior of Ionic Microgels

The cross-linked polymer network structure of microgels is responsible for their unique ability to undergo abrupt volume changes in response to changes in external stimuli, which include temperature, pH, ionic strength, and solvent composition [26–30]. This volume phase transition of these microgels is thermodynamically similar to that of bulk microgels, which may range in size from a millimeter to a few centimeters. Since the transition occurs on much shorter timescales, however, it opens the door to an important potential industrial application [20,31–33]. The swelling behavior of microgels was first experimentally observed by Tanaka [34], whereas it was theoretically predicted by Dusek and Patterson [35]. Since then, the swelling behavior of microgels has become a fundamental problem in polymer physics and has been studied by a variety of experimental techniques, including neutron scattering [12, 36, 37], electrophoresis [28], and by many statistical mechanical theories and simulation methods [38–46].

The degree of swelling is governed by four types of interactions that compete within microgel particles. These are van der Waals interactions, hydrophobic interactions, hydrogen bonding interactions, and electrostatic interactions [2]. Van der Waals interactions are attractive interactions that occur between the network chains of microgel particles. This interaction depends on the solvent's composition. Hydrophobic interactions are noncovalent attractive forces and occur between nonpolar parts of polymer chains (occur only for physically cross-linked microgels). Hydrogen bonding interactions arise when a hydrogen atom is close to an atom of high electronegativity (the tendency of an atom to attract a bonding pair of electrons), such as oxygen. These interactions are relevant in the study of the swelling behavior of nonionic microgels, but do not play a significant role in ionic microgel solutions, except at high concentrations. Finally, electrostatic interactions between counterion and coions and ionic microgels in the solution result in increased swelling or deswelling of the microgel network. The strength of the electrostatic interaction depends on the concentration of charges in the microgel solution. Table. 1.1 shows the magnitudes of these four interparticle interactions.

Table 1.1. The magnitude of van der Waals, hydrophobic, hydrogen bonding, and electrostatic interparticle interactions [2].

Interaction	**Value ($\sim$ eV/atom)**
Electrostatic interaction	10^{-1}
Hydrogen bonding	10^{-1}
Hydrophobic	10^{-3}
van der Waals	10^{-2}

As stated earlier, microgels are very sensitive to pH, temperature, and ionic strength. These microgels are called "stimulus-responsive" or smart microgels. Amongst the smart microgels, ionic microgels have attracted much attention due to their unique properties. Below, a discussion of the influence of some external stimuli on the swelling of charged microgels is summarized.

The effect of temperature: Thermoresponsive microgels, such as Poly(N-isopropylacrylamide) (PNIPAM) are, some of the more interesting and commonly studied types of microgel. These microgels possess the ability to respond to changes in temperature by undergoing reversible swelling or deswelling transitions. In 1986, Pelton and Chibante prepared the first microgels based on PNIPAM that exploit the lower critical temperature behavior of PNIPAM to generate volume phase transitions (VPT) in microgels. In a VPT, a microgel decreases in size above a critical temperature (T_c), but can reversibly re-swell to its original size at room temperature [1]. The temperature dependence of the swelling behavior of thermoresponsive microgels is displayed in Figure 1.3. As seen, below the temperature $T_c = 32°C$, which is the lower critical temperature, the PNIPAM microgel increases in size but, when $T > 32°C$, the microgel shrinks in size. This behavior is due to interactions of microgels with solvent in a temperature-dependent fashion. At $T < T_c$, the interactions between the solvent and polymer are weakened. Therefore, the microgel absorbs water and swells. When $T > T_c$, the polymer-polymer interactions are strengthened; thus, the water is expelled from the microgel interior, resulting in a deswelling of the microgel. Finally, this swelling process is mainly due to hydrophobic interactions.

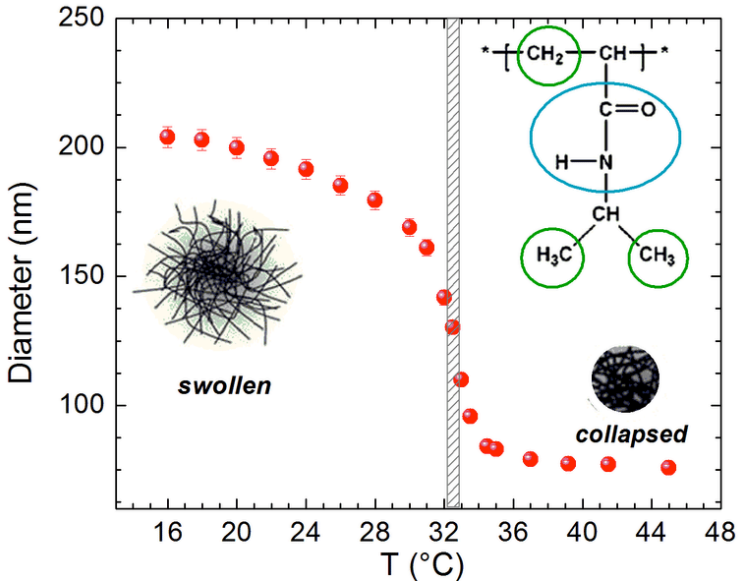

Figure 1.3. Hydrodynamic diameter of PNIPAM microgel particles as a function of temperature. Reprinted with permission from ref. [47].

The effect of pH and ionic strength: The structure of a microgel can be easily influenced by the addition of charged monomers, such as acrylic acid (AAc) methacrylic acid (MAAc), due to the local electrostatic repulsion [48]. The local charge density can be controlled by the number of monomers, the pH, or the ionic strength of the solution. It has been shown that the swelling or deswelling of PNIPAM microgels strongly depends on the charged monomer concentration and pH [16, 48].

The swelling behavior of ionic microgel particles is very sensitive to pH level. Changing the pH level, either increasing or decreasing, can cause a sharp increase or decrease in microgel size. This dependence of microgel swelling behavior on pH arises from electrostatic interactions between the ionic species. For example, interpenetrating polymer network (IPN) microgels, which are formed by adding poly(Acrylic Acid) (PAAc)5, usually known as PAA or PAAc, to a PNIPAM network via precipitation polymerization, exhibit an additional sensitivity to pH and ionic strength, compared to pure PNIPAM microgel particles, and also have a lower swelling degree [5]. Figure 1.4 shows a comparison between hydrodynamic radius for PNIPAM and IPN microgels as a function of pH. A sharp drop in the hydrodynamic radius of IPN microgels is observed as the value of pH decreases below 5, which can be attributed to the strong hydrophobic interactions [5]. At this acidic

pH value, the water molecules extrude from the microgel interior. This causes the deswelling of the IPN microgel at low pH value. Between pH = 5 and pH = 10, the size of IPN microgel remains almost unchanged. Indeed, it is well known that PAAc is hydrophilic in this range of pH [5]. In contrast, the PNIPAM microgel is relatively insensitive to pH in the range of pH between 5 and 10. It is clear that the synthesis procedure plays a crucial role in the swelling of the microgels.

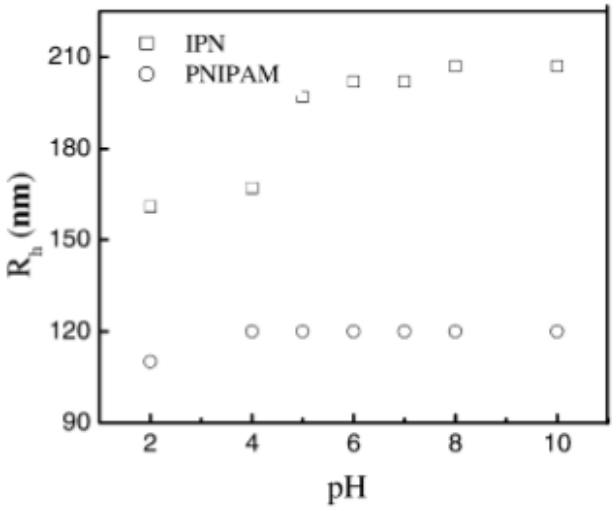

Figure 1.4. pH-induced change in hydrodynamic radius R_h for PNIPAM and IPN microgels. Reprinted with permission from ref. [5].

The incorporation of charges into the polymer network of a microgel affects not only the sensitivity to pH, but also the response to changes in ionic strength, which affect the Debye screening length. The swelling of microgels thus can be controlled by the simple addition of salt to the solution. An increase in the ionic strength of the solution causes a decrease in microgel size, due to the screening of charges. In the case of PNIPAM microgels with high charge, the swelling process is relatively sensitive to the addition of salt, while a weakly charged microgel is nearly unaffected by changes in ionic strength at a temperature lower than the critical temperature [16].

The effect of particle concentration: Another factor influencing the swelling behavior of microgels is particle concentration, changes of which affect the volume fraction and phase behavior of a suspensions. For highly diluted microgel suspensions (low volume fraction), the interaction between particles can be neglected. In this limit, the suspensions is in a colloidal gas state. As

the volume fraction of microgels is increased, the thermodynamic phase of the suspensions changes from a colloidal gas to a colloidal liquid and eventually to a colloidal solid. For example, a stable FCC crystalline solid can occur for sufficiently monodisperse particles. Crystallization in microgel suspensions depends on the charges, salt concentration, temperature, and pH, and many studies have investigated the transition from a fluid to a crystal state, relating the phase behavior of neutral or charged microgel suspensions to that of the hard-sphere system [49–53]. Some of these studies are reviewed in Chapter 2.

1.4. Electrostatic Interactions of Ionic Microgels

Consider a polymer solution consisting of negatively charged macromolecules, such as a microgel, and smaller mobile ions (microions). Charged microgels attract oppositely charged mobile ions, counterions, and repel mobile ions of the same charge, called coions. In this system, microions are distributed with a total charge density

$$\rho(r) = e[n_+(r) - n_-(r) - n_f(r)], \tag{1.1}$$

where, e is the elementary charge and $n_+(r)$, $n_-(r)$, $n_f(r)$ are the number densities of the mobile counterions, coions and fixed charges on the microgel, respectively. The charge density $\rho(r)$ creates an electrostatic potential $\psi(r)$ at a distance r away from a charged surface. In a medium of uniform dielectric permittivity ϵ, the electrostatic potential $\psi(r)$ can be expressed as

$$\nabla^2\psi(r) = \frac{-4\pi}{\epsilon}\rho(r), \tag{1.2}$$

where ∇^2 is the Laplacian operator, which relates the second derivatives of the electrostatic potential to the total charge density. The distributions of microions are controlled by the electrostatic (Coulomb) energy of interaction. The presence of counterions in the solution shields the electric repulsion between the ionic polymer chains, thus reducing the electrostatic potential.

The distribution of fixed charge $n_f(r)$ of the microgels affects particle swelling. As it turns out, the main role of this charge is to generate Donnan potential across the periphery of the microgel particle that influences the counterion distribution. This potential creates an electrostatic pressure difference between the inside and the outside of the microgel particle, causing the gel to

either swell or deswell to balance the electostatic pressure difference by a gel pressure difference. Understanding the effects of electrostatic interactions on the equilibrium swelling behavior of ionic microgel solutions requires calculating the electrostatic contribution to the osmotic pressure of single microgel. For that, the Poisson-Boltzmann (PB) theory, which combines Poisson's equation with the Boltzmann distribution for the microion densities, is used in this study. Futher details are given in the methods's chapter.

1.5. Applications of Microgels

Microgels are considered to be one of the most exciting and promising classes of polymeric materials, especially for biomedical applications, due to their unique, stimuli-responsive swelling behavior. Microgel particles can be used in various industrial applications, such as controlled drug delivery systems and bio-sensors, as well as in imaging applications, and tissue engineering applications [2, 20, 31, 54, 55].

Microgels have received considerable attention for their potential use as drug delivery systems, among many alternative, including nanoparticles, liposomes, micelles, and polymersomes. They offer two distinct advantages over other biomaterials. First, the rate of drug release can be controlled in many ways, such as by changing the crosslinking density, temperature, pH, and electrostatic interactions [20, 54, 56, 57]. Second, microgels may interact less strongly with drugs, consequently reducing the side effects and dramatically improving medical treatments [56]. Microgels can be loaded with nanodrugs using electrostatic interactions, hydrophobic interactions, and hydrogen bonding [20, 56]. A variety of microgels have been designed for controlling drug release, PNIPAM polymer microgels being the most commonly study candidates, since they exhibt a volume phase transition temperature above normal body temperature (see Figure 1.3). Microgels having this property are very attractive for drug carrier systems, as the temperature in cancer cells is usually elevated [20].

Aside from changing the temperature to release drug molecules from microgel particles, the drug can also be released by controlling the pH. The pH value in our body varies from neutral to acidic. For example, the pH value of blood is about 7.4, but in the stomach it is about pH=2. Normal tissues, such as brain tissues and subcutaneous tissues (hypodermis), have a pH in the range of 7.2 to 7.5 [58]. However, the pH value of cancerous cells in tumors is more acidic than in normal cells, typically in the range of 6.4 to 7.0 [58]. Thus, pH differences between these tissues

provide a potential trigger for intracellular drug release. Therefore, pH-sensitive microgels have been considered as promising anticancer drug carriers [56, 59].

In addition to drug delivery applications, microgels have also been used in tissue engineering applications. Microgels exhibit good biodegradability, biocompatibility, and cell adhesion properties, which allow design of injectable microgels for improving the mechanical properties of degenerated intervertebral disks or for soft-tissue repair [60]. Microgels also have many applications to biosensing [54]. For example, they can be used to determine or sense the levels of blood glucose, since microgels are very sensitive to an increase in the concentration of specific biomolecules. Also, they can act as contrast image agents in magnetic resonance imaging (MRI) devices, which can improve sensitivity and quality of MRI images [61].

1.6. Objectives

The main objective of this work is to develop and investigate physical models and simulation methods that could make a suitable basis for the prediction of the equilibrium swelling and thermodynamic phase behavior of swollen ionic microgels. This study has these specific objectives:

To develop an accurate model for the equilibrium thermodynamic behavior of a swollen *single* ionic microgel in the presence of counterions and salt ions.

To develop an accurate model for the equilibrium thermodynamic behavior of *suspensions* of swollen ionic microgels.

The specific issues that arise in modeling ionic microgels are

1. Influence of ion distributions on the swelling of ionic microgels.
2. Role of osmotic pressure in the equilibrium swelling of ionic microgels.
3. Influence of salt and particle concentration change on the microgel size.

1.7. Contributions

The fundamental goal of any ionic microgel study is to understand the thermodynamic and structural properties in terms of particle interactions, which is generally done within the framework of statistical mechanics [62]. Denton and Tang [39] studied the equilibrium swelling and osmotic pressure of volume-charged microgels. However, they did not consider spherical microgels with

uniform surface-charged microgels or different shapes of ionic microgels. Therefore, we have modeled various charge distributions over spherical, microcapsule, and cylindrical microgels. By running molecular dynamics simulations of these microgel systems and determining their equilibrium swelling ratios, we characterized the influence of particle geometry and fixed charge distributions on osmotic pressure and swelling of microgels. We have compared our results for swelling behavior of surface-charged microgels with those for volume-charged microgels presented in ref. [39]. By running Monte Carlo simulations of surface-charged microgels and determining the radial distribution functions and static structure factors, we characterized the ability of the ionic microgel particles to form a crystal phase and showed that microgels can deform at high concentrations by forming facets at the contact area. Also, we calculated the bulk osmotic pressure from the MC method for surface-charged microgel suspensions and compared our results with the predictions of Poisson-Boltzmann theory in the cell model. Finally, our theoretical models and computer simulations will allow for a better description of the role of ion distributions and the shapes of microgels on swelling. These methods could also be extended to model hollow ionic cylindrical microgels and could potentially be used to guide the design of smart, responsive particles based on the increased understanding of microgel swelling behavior. Parts of this dissertation have been published [12, 63] and other parts are in preparation for publication.

1.8. Outline

After the general introduction and background discussion on microgels in Chapter 1, this dissertation continues in Chapter 2 with a brief literature review on ionic microgels and their relevant properties. This chapter serves to introduce foundational relationships discussed throughout the dissertation, including the swelling behavior, osmotic pressure, and counterion distributions of ionic microgels. It also covers recent work on the osmotic swelling behavior of ionic microgels. Chapter 3 presents a description of the physical models. Chapter 4 introduces key theories and background frameworks to model ionic microgels. This chapter includes the Poisson-Boltzmann theory, exact statistical mechanical relations in the cell model, linear response theory of effective electrostatic interactions, and the Flory-Rehner theory of polymer networks. Chapter 5 introduces the principles of molecular dynamics (MD) and Monte Carlo (MC) simulations and describes the simulation setup for microgel systems. Chapter 6 is dedicated to discussing the obtained results and suggestions for future work.

2. LITERATURE REVIEW

Physical properties of microgel particles have long been the subject of intense research, due to the wide range of their technological applications. Thus, scientists have released several thousand publications on "non-ionic microgels" and "ionic microgels" since the term "microgel" was introduced in 1949 by Baker to describe a network of polymeric chains forming a particle suspended in a solvent [3]. Many experimental techniques and theoretical approaches have been used to study different aspects of microgel particles, such as swelling behavior, osmotic pressure, structural phases of microgel particles of different geometries, e.g., spherical, capsule, and cylindrical microgels, and modeling equilibrium swelling of non-ionic and ionic microgels. The goal of this chapter is to outline some experimental techniques used to synthesize microgel particles and characterization tools to study the properties of microgel particles and suspensions as well as to inform the reader of the work that has been completed to study osmotic pressure and swelling behavior of ionic microgels and their interactions with one another. However, since we cannot cover the entire field, we instead focus on the topics relevant to the work described in this dissertation.

2.1. Microgel Synthesis and Characterization

Numerous reviews on the preparation, characterization, and modification of microgel particles have been published. For example, Pich and Richtering [37] and Pelton [1] provide excellent overviews of microgels and their synthesis and behavior in dispersed media. There are various strategies and methods for the preparation and the characterization of microgels, and here the most common standard methods to synthesize and characterize polymeric microgels are reviewed.

2.1.1. Microgel Synthesis

Generally, the techniques used to prepare bulk hydrogel can be applied to microgel synthesis [64]. In such methods, bulk microgels are mechanically ground using a high shear mechanical cutter to form microgel particles. However, when synthesizing microgels, some essential aspects need to be considered. First, it is of interest to control the shape, the size, and particle size distribution of microgels during the preparation process. Second, the stability of microgel systems is a very important aspect to avoid aggregation and precipitation. When it comes to techniques for preparing microgel particles, free-radical polymerisation is one of the most common

reactions to synthesize microgels [65–67]. This technique was first utilized by Philip Chibante in 1978 for preparation of PNIPAM microgels [1, 68, 69], and has been widely used for the synthesis of thermosensitive PNIPAM [70–74]. In addtion, this technique has been successfully used for the preparation of hollow microgels (microcapsules) [75–77] and PNIPAM cylindrical microgels [14]. In this fabrication technique, all ingredients, including the NIPAM monomers, crosslinker agent (e.g., N,N'-methylenebisacrylamide (MBA)), and initiator molecules (e.g., potassium sulfate), are dissolved in a solvent to drive microgel particle formation. The formation of microgel particles occurs by nucleation mechanism. Besides precipitation polymerization techniques, there are several other techniques. For example, emulsification techniques are useful to prepare highly monodisperse microgel particles. There has been growing interest in these techniques because of the simplicity of design and better control of the droplet size. Another approach is microfluidic techniques. In these techniques, microfluidic devices are used to produce microgel particles with a size of about 1–30 micrometers via the emulsification of polymer solutions.

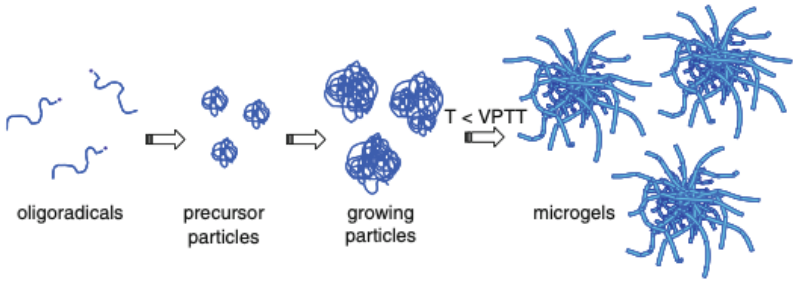

Figure 2.1. Microgel formation by precipitation polymerization [37].

Finally, precipitation polymerization is a unique and powerful technique for synthesizing microgel particles with homogeneous size and shape, and the resulting microgel particles are free of any stabilizer or surfactant [37, 78]. In this technique, it easy to (1) control the size of microgel particles over a broad range from 100 nm to 3 μm, (2) obtain a narrow particle size distribution, and (3) integrate different types of monomers into the microgel network [37]. However, this technique has some limitations. For example, only thermally stable materials can be used since the polymerization occurs at high temperatures, and it is hard to form very small microgels with size below 50 nm without the use of additional stabilizing agents [37].

2.1.2. Microgel Characterization

2.1.3. Dynamic Light Scattering

Dynamic light scattering (DLS) is the most standard technique for characterizing the sizes of microgel particles dispersed in an aqueous solvent [4, 10, 38, 79]. It can also be used to obtain measurements of several parameters, such as molecular weight, viscosity of the dispersion medium, and translational diffusion coefficient [80]. Dynamic light scattering has become a standard technique because it provides rapid, accurate, and reproducible results [79, 80]. Figure 2.2 shows a typical set-up of a dynamic light scattering instrument. A vertically polarized light beam, such as a laser, is passed through the sample. A lens (L) is used to focus the light beam into the measurement area. The detector is placed at a certain angle (often at 90 degrees). The scattered light intensity (number of photons per time) is collected and relayed to a digital correlator to extract the correlation function. A computer is then used to convert the decay of this correlation function into a diffusion coefficient and a particle size [80].

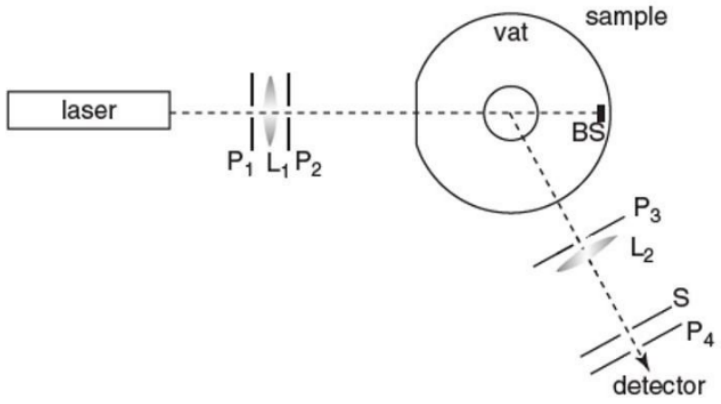

Figure 2.2. Schematic diagram of the set-up for a dynamic light scattering (DLS) instrument [80].

When laser light is passed into a low concentration (dilute) solution of microgels, the incident light is scattered in all directions by the particles in the solution (due to Brownian motion). Fluctuations of the scattered light intensity are converted to the mean translational diffusion coefficient, which can be further converted into particle size by means of the Stokes–Einstein equation [80],

$$D = \frac{k_B T}{6\pi\eta R_h}, \tag{2.1}$$

where D is the translational diffusion coefficient, k_B is the Boltzmann constant, η is the viscosity of the medium, and R_h is the hydrodynamic particle radius. Note that the surface of a microgel particle contains an attached layer of molecules and ions. This attached layer moves with the particle in the solvent. Therefore, the hydrodynamic particle radius is larger than the actual radius of the particle [80]. It has been found that the size of a microgel particle measured by dynamic light scattering is larger than the corresponding size obtained by static light scattering, which can be attributed to the brushes on microgels [10]. Finally, static light scattering, small-angle X-ray scattering, and small-angle neutron scattering are further techniques used to measure particle size. Static light scattering (SLS) is used to measure radius of gyration. For microgel particles diffusing in an aqueous solvent, the given hydrodynamic radius alone cannot be relied on to accurately represent particle geometries, which should, therefore, be inferred by the ratio of R_g/R_h [80].

2.1.4. Conductometric and Potentiometric Titration Methods

The charge content of microgel particles can be measured as a function of pH by a combination of conductometric and potentiometric titration methods [33, 81]. Conductometric titration is used to measure the total charge of ionic microgel particles. The principle behind the conductometric titration method is that counterions and coions have different conductance values. Therefore, during the titration, one of the ions is exchanged by the other and these two ions will change the ionic conductivity of the solution. The degree of ionization of microgel particles can be measured by potentiometric titration technique [81], which is based on the potential across the polymer solution.

2.2. Osmotic Pressure and Swelling of Ionic Microgels

In recent years, considerable attention has been drawn to the study of ionic microgels, where the network is formed by either amidinium groups or charged monomers [4, 28, 39, 42]. The amidinium groups arise from the initiator, located at the surface of the particles. Charged monomers are distributed inside the particle network and are expected to be uniformly distributed throughout the particle. Examples of ionic microgels are ones obtained by copolymerization of monomers of N-isopropylacrylamide (NIPAM) with an ionizable monomer [82]. There has been a growing interest in understanding the swelling behavior and structure of single ionic microgels and also a suspension of ionic microgels to encapsulate active molecules for controlled release purposes [2, 83]. In such applications, charged molecules would be attached to the network structure by electrostatic attraction. This kind of process strongly depends on the penetration of the ions and the value of

the charges of the particle. Indeed, charges control the net osmotic pressure and the swelling of ionic microgels, and this is one of the main factors responsible for the equilibrium swelling of ionic microgels.

Fernández-Nieves et al. [4] prepared a volume-charged microgel using experimental techniques to show that swelling behavior and osmotic pressure of ionic microgel particle depends on charge. They found that the swelling process is controlled by the counterion contribution to the osmotic pressure, and the transition from the deswollen state to the swollen state is continuous. By using the Flory-Huggins model, they were able to explain the effect of the counterion distribution caused by the presence of fixed charges on the microgel. It was found that the microgel starts to swell below about pH = 4.2, then desewlls above pH = 4.2. This means that below 4.2, the microgel becomes increasingly more ionized, thus its volume increases [4]. In other work done by Fernández-Nieves et al. [28], they looked at the effect of external osmotic pressure on the deswelling behavior of an ionic microgel suspension. Combining experimental techniques with the Flory thermodynamic theory of polymer networks, they showed that ionic microgels start to deswell at a certain value of the external osmotic pressure. Below this value, the ionic microgel swells with decreasing osmotic pressure. This certain value of pH depends on the charge density of the microgel particles [28].

A similar study on the influence of pH completed by Karg et al. [16] demonstrated that different pH values and salt concentrations can induce a change in the size of PNIPAM-Poly(allylacetic acid) copolymer microgels. By varying the pH values from pH = 8 to pH = 10, amounts of charged comonomer, and temperature of the system, the authors characterized the influence of pH and ionic strength on the swelling behavior of the microgel particle and determined whether this would cause a significant shift of the volume phase transition temperature toward higher values [16].

Obeso-Vera et al. [21] have studied the influences of crosslink density and crosslink type on the size and swelling behavior of N-isopropylacrylamide (NIPAAm) microgels. The authors prepared microgel particles by the dispersion polymerization technique and used different types of crosslinkers, such as N,N'-methylenebisacrylamide (MBA), ethylene glycol dimethacrylate (EGDMA) an 3,9-divinyl-2,4,8,10-tetra-oxaspiro[5.5] undecane (DVA), to study the swelling properties of the microgel [21]. Through this work, it was found that the microgel that was synthesized using an MBA crosslinker produced a larger particle size and had a higher swelling ratio, followed by the microgel that was synthesized using EGDMA and DVA crosslinkers [21]. This observation can be

related to the hydrophilic or hydrophobic characteristics of the crosslinkers. The results of this work indicated that the material used for crosslinking in microgel formulations plays a significant role in controlling microgel swelling. Also, some studies have shown that increasing the initiator amount can accelerate deswelling for PNIPAM microgels [6, 84, 85]

The study of Karg et al. [16] also observed that the PNIPAAm-co-allylacetic microgels synthesized using 5 mol% MBA crosslinker have a higher degree of swelling than the PNIPAAm-co-vinylacetic acid microgel synthesized using 2 mol% MBA crosslinker from Hoare and Pelton [86]. This is a remarkable result, since according to the swelling theory of gels, an increase in crosslinker density increases the elastic entropy, at the same time the swelling degree of microgel decreases [43].

As stated in the previous chapter, particle concentrations and ion distributions influence the swelling and the osmotic pressure of ionic microgels. Aside from experimental studies of these physical properties, there has also been a focus on developing analytical theories in recent years. Indeed, many analytical theories have studied the thermodynamic properties of ionic microgels [39, 63, 87–89]. The structure of ionic microgel dispersions has also been of interest, and various shapes of microgels have been studied [36, 90–92]. Corresponding computer simulations, either molecular dynamics simulations or Monte Carlo simulations, have also been performed [40, 45, 46, 93–95].

Ion distributions play an important role in changing the size of a microgel and osmotic pressure. The location of microgel charges spread over the surface or the volume of microgel particles can induce variations in ion densities and swelling [39, 96]. Thus, determining the counterion distribution inside and around the microgel is an important aspect of microgel research. For example, Irene et al. [97] studied equilibrium distributions of ions around ionic microgel particles dispersed in a solvent using coarse-grained Monte Carlo simulations and the Ornstein–Zernike integral equation theory. The authors found that valence of counterions affected the internal structure of the microgel and shifted the volume transition to lower temperatures [98]. As reported in the literature, increasing the particle charge shifts the swelling ratio to larger values [39]. A study by Denton and Tang [39] explored the influences of volume fraction on counterion distributions. The authors found that the fraction of confined counterions increases rapidly as the volume fraction increases [39]. This means that an increase in size of the microgel tendes to a neutralize the microgel, whereas smaller microgels tend to possess a net charge.

In addition, Claudio et al. [40] have performed numerous works aimed at investigating how much the mean-field Poisson-Boltzmann theory deviates from the results of simulations for a single ionic microgel in the cell model. In this work, the authors studied the influence of excluded volume effect, charge correlations, ion distribution, and thermal fluctuations in the polymer chain of the microgel and compared the predictions of a Poisson–Boltzmann cell model with molecular dynamic simulation data for the case of good solvent and monovalent ions [40]. Under this assumption, the authors concluded that the ion distributions predicted by the Poisson–Boltzmann theory in the spherical cell model agreed very well with those obtained from simulations [40].

The work described in Denton and Tang [39] studied the swelling and osmotic pressure of single ionic microgels with uniform volume charges in the spherical cell model by considering the solvent as a dielectric continuum with a uniform dielectric constant. The study developed an exact statistical mechanical theorem in the canonical ensemble (fixed number of particles, system volume, and temperature) based on the partition function and Helmholtz free energy for computing swelling and osmotic pressure [39]. Additionally, the authors validated their results by comparing calculations from nonlinear Poisson-Boltzmann theory with data from molecular dynamics simulations. Denton and Tang [39] found that the deswelling of ionic microgel particles with increasing particle concentration can be enhanced via redistribution of microions. The authors also found that increases in salt concentration caused a shrink in the size of the microgel, and also weakened the variation of swelling with particle density [39].

Nojd et al. [38] prepared ionic hydrogenated PNIPAM particles and deuterated PNIPAM particles to investigate the swelling of these ionic microgel particles from very low concentrations to high concentrations using a combination of light, X-ray and neutron scattering techniques. The authors also modeled the swelling and osmotic pressure by solving the Poisson–Boltzmann equation for the electrostatic potential within a spherical cell model. Their system was a spherical fuzzy microgel. Thus, to investigate whether the electric field generated by the core is strong enough to induce significant stretching of microgel dangling ends, they performed a Monte-Carlo simulation. The authors found a significant increase in the size of the microgel at very low concentrations, which can be attributed to the presence of a charge in the polymer chain, and also at concentrations above shell overlap [38]. Interestingly, there was no change in the microgel size at intermediate concentrations. Finally, the authors described the reasons for discrepancies between small-angle

neutron scattering and dynamic light scattering measurements, and how configurational changes in the dangling ends seem unlikely to be visible in static light scattering, and also that their model is not able to explain the plateau in the microgel size at intermediate concentrations.

In the same scope, Scotti et al. [36] considered non-ionic ultra-low cross-linked pNIPAM microgel and non-ionic capsule "hollow" microgels. By varying crosslink densities and the architecture of a microgel, and using X-ray and neutron scattering and molecular simulation methods to analyze the results, the authors measured and modeled the response of microgels in overcrowded environments to describe how the swelling behavior of these system varied. In other words, the authors investigated how the interplay between the microgel particles and the cross-link concentration within the polymer network affected the swelling behavior of microgels when they are squeezed by their neighbors. It was observed that [36] capsule microgels were more compressed than spherical crosslinked microgels. The authors also found that introducing a cavity filled with a solvent significantly decreased the size of the hollow microgel in overcrowded environments compared to spherical microgels. From this analysis, it follows that the amount of crosslinkers is not sufficient to predict the swelling behavior of microgels in overcrowded environments, and therefore the architecture of a microgel must be considered together with the amount of crosslinkers in order to predict whether one microgel is softer than another and whether it interpenetrates or is compressed by its neighbors [36]. Finally, the authors state that having a cavity filled with a solvent can enhance the deswelling of microgels rather than reducing the crosslinker densities in overcrowded environments.

The swelling, structure, and permeability of hollow charged microgels have been studied theoretically [30,99], computationally [45], and experimentally [8,11,12,100]. For example, Wypysek et al. [12] demonstrated how the size and structure of a hollow ionic microgel can be tunable by varying the level of pH and ionic strength. The authors systematically investigated the influence of pH and salt on the structure and swelling behavior of charged hollow microgels by using small-angle neutron and light scattering experimental techniques and interpreted their results via the Poisson–Boltzmann theory in the cell model. Interestingly, the authors found that increasing the ionic strength decreases the thickness of the fuzzy layer at the outer surface of the microgels. In contrast, with increasing ionic strength, the fuzzy layer grew thicker at the cavity wall. In other words, the ionic strength reduces the local Debye screening length; therefore, the charged polymers encounter a weaker electrostatic repulsion from neighboring polymers. The electrostatic osmotic

pressure was found to decrease throughout the hollow microgel. As a result, the polymer chains near the cavity surface are free to expand, which shrinks the cavity size. In contrast, the outward dangling chains collapse onto the hollow microgel surface, leading to a more homogeneous and compact external structure [12].

In studying a suspension of ionic microgel particles, it has been found that ionic microgels at low concentrations interact via an effective pair potential. At large separation distances, the effective pair potential has been found to be a form of Yukawa potential, and at shorter distances, a soft-core interaction [62,93,101–103]. For example, Chung and Denton [101] computed the effective electrostatic interactions between two species of charged colloids via linear response theory in the framework of the primitive model. To validate their theory, the authors performed molecular dynamics simulations of the coarse-grained model in the canonical ensemble (fixed particle numbers, system volume, and temperature). Their work provided a characterization of the effective electrostatic interactions, and explored the osmotic pressure and structure of polydisperse suspensions and helped to motivate our model of a mixture of surface-charged microgels.

More recently, Weyer and Denton [104] studied the swelling and structural properties of ionic microgel suspensions using Monte Carlo simulation and thermodynamic perturbation theory for a coarse-grained model of compressible, permeable, charged spheres governed by effective interparticle interactions [104]. The authors considered a microgel with a uniform volume charge dispersed in a solvent with counterions that were allowed to penetrate the microgel particles freely. The counterions in the solution screened electrostatic interactions between the charged microgels, which were modeled using the Yukawa potential. The Yukawa potential accounts for the screening of interactions by including an exponentially decaying factor. It was found that for strongly charged microgels (high valence number) theory and simulations gave equilibrium swelling ratios in close agreements [104]. Therefore, simulations and theories of coarse-grained models can be very useful to study particle swelling and interpret future experiments of suspensions of ionic microgels.

In another theoretical approach based on Ornstein-Zernike (OZ) integral equations, Moncho-Jordá [46] studied the effective charge of ionic microgel particles in the presence of monovalent salt. In this work, the ionic density profiles, effective interaction between microgel particles, and the excluded-volume repulsion between the microgel particles and the ions were investigated from the extreme dilute limit to highly concentrated suspensions [46]. The study shows that steric inter-

actions do not have a significant effect on the counterion/coion penetration when the microgel particle is in the swollen state, indicating that only the electrostatic interaction governs the ion density profiles [46]. Indeed, many other theoretical studies have pointed out that penetration of microions is affected only by the electrostatic interactions in the swollen state [46, 98]. Finally, the study also pointed out that steric interactions between monomers show a significant contribution when the microgel is in the deswollen state [46], due to the excluded volume repulsive force, which prevents counterions and coions from penetrating the microgel particles [46, 98].

3. MODELS

The aim of this chapter is to describe the physical models. This chapter is divided into three sections. In the first section, we present the so-called primitive model, where the coions and counterions are taken into account explicitly while the solvent is implicit. The next section aims to address the use of the cell model and its limitations. In the third section, we discuss the one-component model that is standardly used to describe the suspension of ionic microgels, where the coions and counterions are taken into account implicitly.

3.1. Ionic Microgels Solutions

When charged microgels are dispersed in a polar solvent, the polymer chains of the microgels acquire a net charge, due to the dissociation of counterions, leaving the microgels with a negative charge. Dependence on the synthesis of the microgels, the charge can be spread over the surface or the volume of the particles [4, 96]. In addition to the counterions, the presence of salt in solution contributes to coions and additional counterions. For example, a solvent like water at room temperature and neutral acidity contains about 10^{-7} M of H^+ and hydroxyl OH^- ions. The total excess amount of coions and counterions contribute to "added salt". The salt concentration can be lowered by deionizing the solvent.

Consider an aqueous suspension in (Donnan equilibrium with an electrolyte reservoir) of N_m ionic microgels in a volume V at temperature T. As illustrated in Figure 3.1, microgel particles, which are suspended by Brownian motion in a fluid phase (usually water for ionic microgels), are much larger in size than the microions (counterions and coions). Microions can move through a semi-permeable membrane with the reservoir, while the microgels are confined to the volume of the suspension. The salt concentration of the suspension is determined by the reservoir concentration. For a closed suspension, all particles, including microgels and microions, are confined to the same volume V and the number of salt ion pairs N_s is equal to the number of coions. In the bulk suspension illustrated in Figure 3.1, the number of counterions N_c is given by $zN_c = ZN_m + zN_s$ as required by electroneutrality, and the total number of microions is $N_c + 2N_s$.

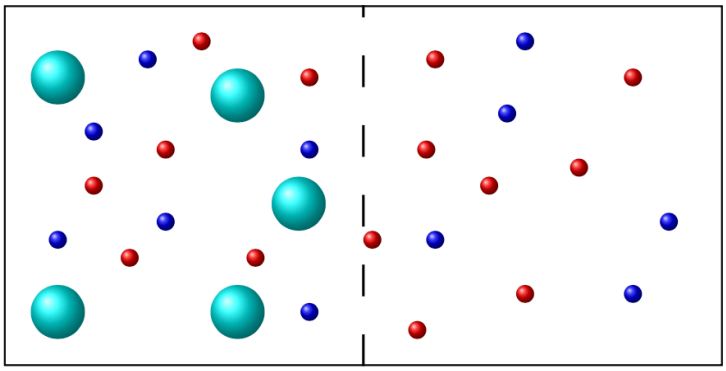

Figure 3.1. Primitive model of charged spherical macroions(large cyan spheres) and point microions (small red/blue spheres) dispersed in a dielectric continuum.

In Figure 3.2, the microgel itself acts like a semi-permeable membrane, allowing microions to diffuse between the interior and exterior microgel regions, but holding the fixed charge within the microgel. The fixed charge on the polyelectrolyte chains creates a nonuniform distribution of microions, which causes an electrostatic osmotic pressure. In addtion, the self-repulsion of the fixed charge within the microgel generates an outward electrostatic pressure that acts to swell the microgel. Equilibrium swelling is reached when the sum of the outward electrostatic pressure and the inward elastic pressure, which is a restoring force exerted by the cross-linked gel, is equal to zero. It is important to note that the swelling of ionic microgels is limited in our model by elastic forces exerted by the cross-link polymer network.

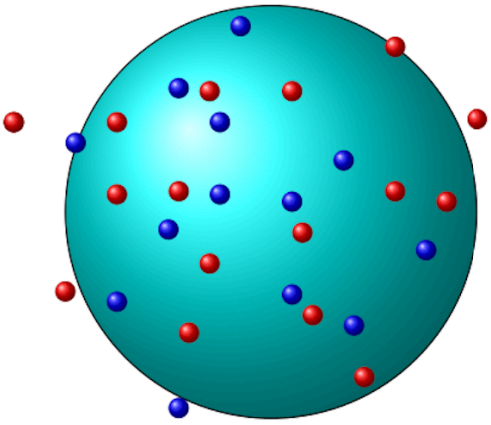

Figure 3.2. A single spherical ionic microgel of valence Z in water. The microgel is permeable to water and small ions (smaller spheres (red counterions) and (blue coions)).

Explicit molecular modeling of ionic polymer solutions, micellar solutions, and aqueous solutions containing charged membranes is a very challenging computational problem, complicated by the many degrees of freedom of the solvent [105–107]. A solution containing a solute requires an additional understanding of the solvent-solute interaction, the degree of dissociation of counterions, and the conformation of the solute (e.g., microgels). The primitive model of charged colloids and polyelectrolytes is a practical basis for qualitatively describing such systems.

3.2. Primitive Model

A detailed theoretical description of ionic microgel suspensions is possible within the primitive model of charged colloids, which is illustrated in Figure 3.1. In this model, the microgels are modeled as permeable charged spheres or cylinders with valence Z (charge $-Ze$) and the microions as point charges with valence $-z$ and z, respectively. The solvent is treated as a uniform continuum with dielectric constant ϵ, which reduces the strength of the bare Coulomb interaction between a pair of ions at separation r to

$$\beta v(r) = \frac{\lambda_B}{r}, \tag{3.1}$$

where $\beta = 1/(k_B T)$ and $\lambda_B = e^2/(\epsilon k_B T)$ defines the Bjerrum length, which is the distance at which the Coulomb energy between two unit charges is equal to the thermal energy of $k_B T$ of temperature T. Each microgel is assumed to carry a fixed charge, uniformly distributed over its surface or volume, fluctuations being ignored.

Although the primitive model is considered to capture most of the features of real ionic microgel suspensions, it is an idealization. For example, systems that include solvation effects cannot be studied with the primitive model. Thus, much of our understanding of charged microgels has come from studying simpler models, either by reducing the system into subvolumes (cells), each containing one microgel together with its neutralizing counterions or by coarse-graining out the microions. The most famous of these models is the cell model, which focuses on a single microgel and the one-component model, which reduces a suspension of microgels to a suspension of pseudo-particles governed by effective interactions. The term pseudo-particle implies that the microgels are not bare and are governed by effective interactions (effective Hamiltonian). The following sections describe these two models that are used to study the swelling and osmotic pressure of ionic microgel particles.

3.3. Ionic Microgels: Cell Model

In 1955, Marcus [108] realized that the cell model method of Wigner and Seitz, which in solid-state physics is a method to calculate important electronic properties of a solid, can be applied to colloidal particles [109]. The cell model can be seen as an attempt to reduce a many-microgels (bulk suspension) problem to a single microgel problem dispersed in an electrolyte solution (see Figure 3.3). Additionally, the microgel is assumed to be uniformly charged and to have the same shape as the cell. In this simple model, the interactions between the small, mobile ions and between the microgel and the small ions in the same cell are explicitly taken into account.

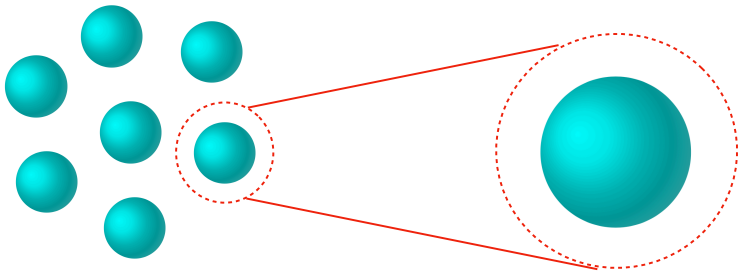

Figure 3.3. Schematic representation of cell model.

In the cell model, the electrostatic potential $\psi(r)$ and microion densities depend only on the distance r from the center. Therefore, the Poisson-Boltzmann equation reduces to an ordinary differential equation for $\psi(r)$. More details about the Poisson-Boltzmann equation in the cell model are given in section 4.3. Gauss's law implies the boundary condition that the electric field vanishes on the surface of the electroneutral cell, i.e.

$$\left(\frac{d\psi(r)}{dr}\right)_{r=R} = 0, \tag{3.2}$$

where R is the radius of the cell. For a closed suspension, the arbitrary location of the reference point of the electrostatic potential is often chosen as the cell boundary: $\psi(R) = 0$, whereas for a suspension in Donnan equilibrium, the potential is conventionally chosen to vanish in the reservoir.

Although the combination of the cell model with the primitive model gives a significant abstraction from a bulk suspension of ionic microgels, the cell model has proven accurate, compared

with multi-microgel simulations and experiments, in predicting osmotic pressures and swelling behavior of ionic microgels.

In this study, cell models are used for three different geometries of ionic microgel particles. In the spherical cell model (see Figure 3.4), a spherical of ionic microgel of swollen radius a with spherically symmetric fixed charge distribution is centered in a spherical cell, representing a suspension of spherical microgels of volume fraction (the fraction of the total sample volume which is occupied by the particles) $\phi = (a/R)^3$.

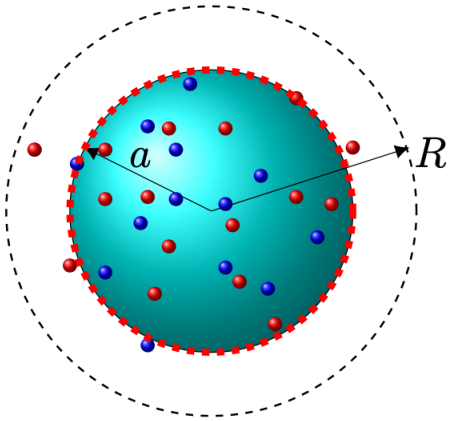

Figure 3.4. Schematic representation of the cell model with spherical ionic microgel of swollen radius a (dry radius a_0) and valence Z centered in a spherical cell of radius R along with microions. The radius R of the cell is fixed, and both counterions (small red spheres) and coions (small blue spheres) are free to move throughout the cell volume.

In the spherical cell model (see Figure 3.5), a spherical shell (capsule) of ionic microgel of inner swollen radius a and outer swollen radius b with spherically symmetric fixed charge distribution is centered in a spherical cell of radius R that is determined by the concentration of microgels inside the suspension $\phi = (b/R)^3$.

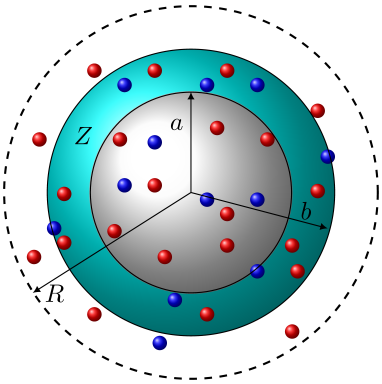

Figure 3.5. A microcapsule of inner swollen radius a, and outer swollen radius b containing $N_{\pm}$ microions is placed at the center of a spherical cell. The radius R of the cell is fixed by the overall microcapsule concentration inside the solution, $R = (\frac{b}{\phi^{1/3}})$. Both counterions (small red spheres) and coions (small blue spheres) are free to throughout over the cell volume.

In the cylindrical cell model (see Figure 3.6), an infinitely long cylinder of ionic gel of cross-sectional radius a with axially symmetric fixed charge distribution is centered in a cylindrical cell of radius R, representing a suspension of cylindrical microgels of volume fraction $\phi = (a/R)^3$.

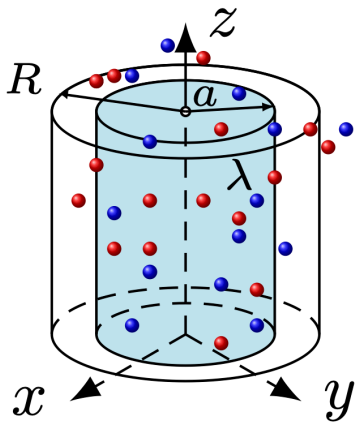

Figure 3.6. Schematic representation of the cell model cylindrical microgels of swollen radius a (dry radius a_0) and linear charge density λ centered in a cylindrical cell of radius R along with microions. The radius R of the cell is fixed, and both counterions (small red spheres) and coions (small blue spheres) are free to move throughout the cell volume.

The linear swelling ratio of a microgel is defined as a ratio of the swollen microgel volume v to the dry microgel volume v_0:

$$\alpha \equiv \left(\frac{v}{v_0}\right)^{1/3} = \left(\frac{\phi}{\phi_0}\right)^{1/3}. \tag{3.3}$$

where ϕ_0 denotes the dry volume fraction of the microgel in a reference swelling state. Assuming uniform swelling of the microgels (swelling ratio does not vary in space), the swelling ratio α can be expressed as the ratio of the actual (swollen) radius a to the dry radius a_0:

$$\alpha = a/a_0. \tag{3.4}$$

To determine the swelling ratio of microcapsule particles, we assumed a uniform swelling of the microcapsule, although the inner and outer swollen radii of a microcapsule are, in principle, independent. For the sake of simplicity, the swelling ratio is defined as

$$\alpha = a/a_0 = b/b_0, \tag{3.5}$$

where b_0 is the outer dry radius of microcapsules. Similarly, the swelling of a cylindrical microgel is assumed to be uniform with radial and axial swelling ratios defined as

$$\alpha_r = a/a_0,\ \alpha_a = h/h_0, \tag{3.6}$$

where α_r is the radial equilibrium swelling ratio and α_a is the axial equilibrium swelling ratio, and h and h_0 are the swollen and dry radii of cylindrical microgels, respectively. It is important to note that these swelling ratios are not constant, since they depend on many parameters such as temperature, salt concentration, and microgel charge. Since a cylindrical microgel, does not swell equally in three dimensions (anisotropic swelling), the linear swelling ratios, may differ in the x, y, and z directions. By assuming two dimensional isotropy swelling, where $\alpha_x = \alpha_y \neq \alpha_z$, the volume swelling ratio may be expressed as

$$\frac{ha^2}{h_0 a_0^2} = \alpha_a \alpha_r^2. \tag{3.7}$$

Due to these differing swelling ratios, a cylinderical microgel has distinct radial and axial osmotic pressures. In order to utilize α_r and α_a to compute the gel contribuations to osmotic pressures, the original Flory-Rehner theory of gel swelling [43] must be modified. More details are presented in the Chapter 4.

As stated earlier, cell models, involving a single microgel, prove useful to study concentrated dispersions. Cell models provide a simple analytic relation between the bulk pressure and the microion densities at the cell boundary ($r = R$). The osmotic pressure of a suspension Π, i.e., the difference in pressure between suspension and reservoir, in the cell model is exactly given by k_BT times the microion density at the outer cell boundary:

$$\Pi = k_BT \left[n_+(R) + n_-(R) \right]. \tag{3.8}$$

This equation is well-known as the cell theorem for the osmotic pressure of a bulk suspension [17]. Even if the particles are strongly correlated, equation 3.8 is still valid. It is important to note that the electrostatic contribution to the osmotic pressure of a single charge cylindrical or spherical microgel is not determined by the difference in ion density between the center and wall of the cell but instead is determined by the difference in pressure between the inside and outside of the gel at the microgel surface [63]. The difference can be attributed to the work required to move counterions and coions between the exterior and interior regions of the microgel. Determining the osmotic pressure of an ionic microgel will allow us to determine the equilibrium swelling behavior of microgels.

3.4. Ionic Microgels: One-Component Model

It is clear that electrostatic interactions in such charged microgel systems play a crucial role in determining the physical properties of bulk suspensions, such as swelling behavior and osmotic pressure [1,2]. The behavior of these systems is extremely complex due to the long-range Coulomb interactions. The first simplifying assumption is to treat the solvent as a dielectric continuum. In addition to that, the short-range ion-ion excluded-volume is modeled by a hard-sphere interaction. A further simplification can be achieved using the cell model, where the system is reduced to only one macroion, along with its neutralizing counterions and coions, as described in section 3.3. Therefore, modeling a bulk solution with high salt concentration is very challenging [110]. For

that purpose, the concept of a one-component model or effective-interaction model, which maps a macroion-microion mixture onto a suspension of pseudo-macroions, as illustrated in Figure 3.7, is a very powerful technique in modeling of colloidal suspensions. In other words, we integrate out all the microscopic degrees of freedom in the partition function in a fixed microgel configuration. Such a coarse-grained description allows predicting bulk thermodynamic and structural properties of the system.

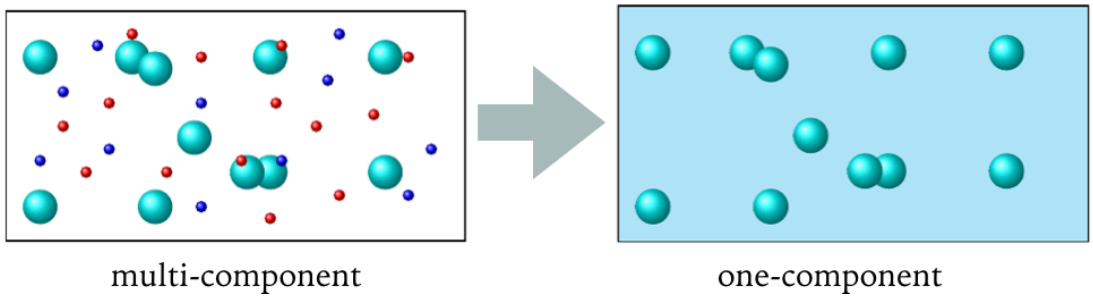

Figure 3.7. An illustration of the one-component model concept.

Within the primitive model of ionic colloidal, the system of interest is modeled as a suspension of N_m, surface-charged spherical microgels of charge $-Ze$, and N_c point counterions of charge ze in solvent in volume V at temperature T (see Figure 3.7). As shown in the illustration, the counterions (small red spheres) and coions (small blue spheres) can freely penetrate the microgel surface and the microgel particles can overlap (interpenetrate). The microions and solvent are implicit (solvent is taken to be a structureless continuum of uniform dielectric constant) in our Monte Carlo simulations, and two different systems were considered in this study. The first system contains only one species of ionic microgel, while the second system contains two species of ionic microgels, as shown in Figure 3.8. The role of electrostatic interactions in the interpenetration and compression of these two models will be described in Chapter 4.

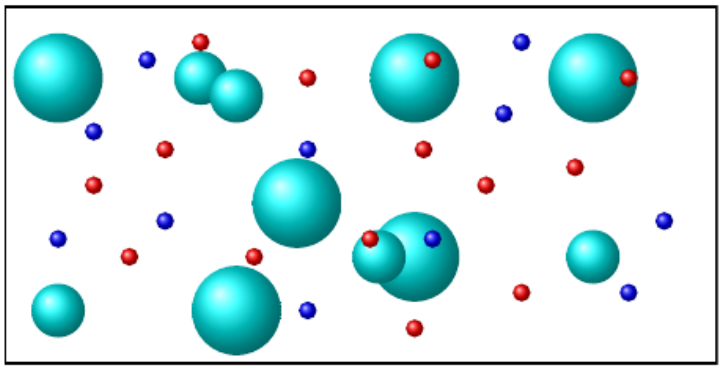

Figure 3.8. Primitive model of binary mixture of charged microgels: two species of charged macroion of valences Z_m (big cyan spheres) and Z_n (small cyan shperes), microions (counterions and coions), and implicit solvent.

From a theoretical viewpoint, different aspects of ionic microgels have attracted the attention of theorists, who have developed several statistical mechanical frameworks and computer simulations methods [41, 46, 101, 111, 112]. The following chapter represents two statistical mechanical frameworks based on the primitive model developed to investigate the structural and thermodynamic properties of these systems described in sections 3.3 and 3.4.

4. THEORETICAL METHODS

4.1. Exact Statistical Mechanical Relations in the Cell Model

For a restricted primitive model electrolyte, some exact statistical mechanical relations in the cell model have been derived for ionic microgels. Using the cell model, the electrostatic component of the total osmotic pressure is determined through an explicit evaluation of a volume derivative of the partition function. Ionic microgels with different geometries and fixed charge distributions, e.g., microcapsule, cylindrical, and spherical, are considered. The derivations start from the Hamiltonian:

$$H = H_e + H_g, \tag{4.1}$$

where H_e is the electrostatic component and H_g is gel component, including the elastic and mixing degrees of freedom of a polymer gel. The electrostatic part can be expressed as

$$H_e = U_m(a) + U_{m\mu}(\{\mathbf{r}\}; a) + U_{\mu\mu}(\{\mathbf{r}\}), \tag{4.2}$$

where U_m(a) is the microgel self-energy and $U_{m\mu}(\{\mathbf{r}\}; a)$ and $U_{\mu\mu}(\{\mathbf{r}\})$ is the microgel-microion and microion-microion interaction energies, respectively. The last two terms in Equation (4.2) depend on the coordinates of all N microions, $\{\mathbf{r_1}, ..., \mathbf{r_N}\} = \{\mathbf{r}\}$. Note that only the first two terms in Equation (4.2) are needed to compute the electrostatic contribution to osmotic pressure since the last term is independent of the microgel radius. To determine the equilibrium ionic density profiles inside and around an ionic microgel particle, the microgel-microion interaction energy can be expressed in the form

$$U_{m\mu}(\{\mathbf{r}\}; a) = \sum_{i=1}^{N} v_{m\mu}(\mathbf{r}_i; a), \tag{4.3}$$

where $v_{m\mu}(\{\mathbf{r}\}; a)$ is the pair potential between the fixed charge of the microgel and microions in the cell. The microgel-microgel correlations are completely neglected in the cell model (see section 3.3), and contributions of such interparticle correlations to the osmotic pressure are known to be weakest in the low-salt limit [113]. For a suspension in which the number of particles N, volume

V, and temperature T are fixed, the Helmholtz free energy F can be expressed as

$$F = -k_B T \ln \mathcal{Z}(N, V, T), \tag{4.4}$$

where $\mathcal{Z}(N, V, T)$ is the canonical partition function. The Helmholtz free energy F decomposes into

$$F = F_e + F_g, \tag{4.5}$$

where F_e is the contribution from electrostatic effects and F_g is the gel contribution. Consequently, the internal osmotic pressure of a single ionic microgel splits into two contributions:

$$\pi_{\text{in}} = \pi_e + \pi_g, \tag{4.6}$$

where π_e and π_g is the electrostatic and gel components of the osmotic pressure of a single ionic microgel, respectively. The electrostatic component of the osmotic pressure of ionic microgel π_{e}, can be defined via a derivative of the Helmholtz free energy F with respect to the microgel volume v. For a spherical microgel with volume $v = 4\pi a^3/3$, the electrostatic pressure is defined as

$$\pi_{\text{e}} = -\left(\frac{\partial F}{\partial v}\right)_{N,T} = -\frac{1}{4\pi a^2}\Big(\frac{\partial U_m(a)}{\partial a} + \Big\langle \frac{\partial U_{m\mu}(a)}{\partial a} \Big\rangle\Big), \tag{4.7}$$

where angular brackets $\langle .. \rangle$ denote an ensemble average over microion configurations. Since the cylindrical microgel can swell in both radial and axial directions, there are two contributions to the total electrostatic osmotic pressure, namely, the as radial osmotic pressure ($\pi_{r,e}$) and the axial osmotic pressure ($\pi_{a,e}$). For a cylindrical microgel with $v = \pi a^2 h$, the radial electrostatic osmotic pressure is defined as

$$\pi_{r,e} = -\frac{1}{2\pi a h}\Big(\frac{\partial U_m(a,h)}{\partial a} + \Big\langle \frac{\partial U_{m\mu}(a,h)}{\partial a} \Big\rangle\Big) \tag{4.8}$$

while for axial electrostatic osmotic pressure

$$\pi_{a,e} = -\frac{1}{\pi a^2}\Big(\frac{\partial U_m(a,h)}{\partial h} + \Big\langle \frac{\partial U_{m\mu}(a,h)}{\partial h} \Big\rangle\Big). \tag{4.9}$$

At equilibrium, the total contribution (electrostatic and gel) to the internal osmotic pressure $\pi_{in} = \pi_e + \pi_g = 0$, implying that the free energy of the system is a minimum with respect to the variation of swelling ratio. Within the spherical and cylindrical cell models, these equations for the electrostatic contribution to the osmotic pressure of a permeable ionic microgel are formally exact. The following sections present derivations of exact statistical mechanical expressions for the single-microgel osmotic pressure for three microgel geometries: microcapsule, infinite cylinders, and spheres.

4.1.1. Ionic Microcapsules

As stated in Section 3.3, the microcapsule swelling is assumed to be uniform. Therefore, the osmotic pressure across the inner interface is related to the osmotic pressure across the outer interface by

$$\pi_{\text{inner}} = -\left(\frac{b}{a}\right)^3 \pi_{\text{out}}. \tag{4.10}$$

Holding the ratio between a and b radii ($\gamma = a/b$) fixed, the electrostatic component of the osmotic pressure of an ionic microcapsule, π_{e}, can be defined via a derivative of the Helmholtz free energy F with respect to the microcapsule volume $v_m = 4\pi b^3/3$:

$$\pi_{\text{e}} = -\left(\frac{\partial F}{\partial v_m}\right)_{\gamma} = -\frac{1}{4\pi b^2}\Big(\frac{\partial U_m(b,\gamma)}{\partial b} + \Big\langle\frac{\partial U_{m\mu}(b,\gamma)}{\partial b}\Big\rangle\Big). \tag{4.11}$$

From Gauss's law, the pair potential between microions and microcapsule is:

$$v_{m\mu}(r;a,b) = \begin{cases} \frac{3Zze^2}{2\epsilon(b^3-a^3)}(b^2-a^2), & 0 < r \leqslant a \\ \\ \frac{3Zze^2}{\epsilon(b^3-a^3)}\left(\frac{b^2}{2} - \frac{1}{3}(\frac{r^2}{2} + \frac{a^3}{r})\right), & a < r < b, \end{cases} \tag{4.12}$$

where, r represents the distance between the microion and the microcapsule center. The microcapsule self-energy, which is the energy stored in the system of charges to be assembled continuously throughout its volume, can be expressed as

$$\beta U_m(a,b) = \frac{3Z^2\lambda_B}{(b^3-a^3)^2}\left(\frac{2b^5 - 5b^2a^3 + 3a^5}{10}\right). \tag{4.13}$$

Rewriting Equation (4.13) in term of γ, Equation (4.13) becomes

$$\beta U_m(b,\gamma) = \frac{3Z^2\lambda_B}{b}\left(\frac{2-5\gamma^3+3\gamma^5}{10(1-\gamma^3)^2}\right). \tag{4.14}$$

The term in Equation (4.11) that involves the microcapsule self-energy is (in k_BT units)

$$\beta\frac{\partial U_m(b,\gamma)}{\partial b} = -\frac{3Z^2\lambda_B}{b^2}\left(\frac{2-5\gamma^3+3\gamma^5}{10(1-\gamma^3)}\right). \tag{4.15}$$

The term that involves the energy of interaction between a microcapsule and a microion of valence Z (in units of k_BT) divids into two contributions, one from the cavity region ($r \leqslant a$),

$$\beta\left\langle\frac{\partial U_{m\mu}(b,\gamma)}{\partial b}\right\rangle_{\rm cav} = \frac{3Z\lambda_B}{2}\frac{1}{b^2}\left(\frac{1-\gamma^2}{1-\gamma^3}\right)\sum_{i=1}^{N} z_i, \tag{4.16}$$

and the other from the shell region ($a < r < b$),

$$\beta\left\langle\frac{\partial U_{m\mu}(b,\gamma)}{\partial b}\right\rangle_{\rm sh} = -\frac{Z\lambda_B}{1-\gamma^3}\frac{\partial}{\partial b}\left\langle\sum_{i=1}^{N} z_i\left(\frac{3}{2b}-\frac{r^2}{2b^3}-\frac{\gamma^3}{r}\right)\right\rangle. \tag{4.17}$$

Substituting the self-energy and interaction energy contributions, namely Equations (4.15)-(4.17) into the electrostatic osmotic pressure in Equation (4.11) yields

$$\begin{aligned}\beta\pi_e v_{\rm sh} \;=\; & \frac{Z^2\lambda_B}{b}\,\frac{2-5\gamma^3+3\gamma^5}{10(1-\gamma^3)} - \frac{Zz\lambda_B}{2b}\Big[\left(1-\gamma^2\right)\left(\langle N_+\rangle_{\rm cav}-\langle N_-\rangle_{\rm cav}\right)\\ & +\langle N_+\rangle_{\rm sh}-\langle N_-\rangle_{\rm sh}-\frac{1}{b^2}\left(\langle r_+^2\rangle_{\rm sh}-\langle r_-^2\rangle_{\rm sh}\right)\Big],\end{aligned} \tag{4.18}$$

where $v_{\rm sh} = \frac{4\pi}{3}(b^3-a^3)$ is the volume of the shell,

$$\langle N_\pm\rangle_{\rm cav} = 4\pi\int_0^a r^2 n_\pm(r)dr \tag{4.19}$$

are mean numbers of microions inside the cavity,

$$\langle N_\pm\rangle_{\rm sh} = 4\pi\int_a^b r^2 n_\pm(r)dr \tag{4.20}$$

are mean numbers of microions inside the shell, and

$$\langle r_{\pm}^2 \rangle_{\rm sh} = 4\pi \int_a^b r^4 n_{\pm}(r) dr \tag{4.21}$$

is second moments of the microion density profiles inside the shell. These Equations (4.19)-(4.21) were used as input in Equation (4.18) to compute the electrostatic pressure, as discussed later in the use of Poisson-Boltzmann theory to compute the microions density in section 4.3.

4.1.2. Surface-Charged Microgels

For a microgel with uniform surface charge, whose fixed charge density is described by

$$n_f(r) = \frac{Z}{4\pi a^2}\,\delta(r-a), \tag{4.22}$$

the pair potential between microions and microgel is:

$$v_{m\mu}(r;a) = \begin{cases} -\frac{Zze^2}{4\pi\epsilon r}, & r > a \\ -\frac{Zze^2}{4\pi\epsilon a}, & r \leq a. \end{cases} \tag{4.23}$$

The Dirac-delta function $\delta(r-a)$ in Equation (4.22) is defined such that when the argument of the function is equal to a, $\delta = \infty$, and when the argument is not equal to a, $\delta = 0$. Mathematically, $\delta(r-a)$ can be defined as

$$\delta(r-a) = \begin{cases} \infty, & \text{if } r = a \\ 0, & \text{if } r \neq a. \end{cases} \tag{4.24}$$

The microgel self-energy and radius derivative of the microgel-microion interaction energy inside the gel ($r \leqslant a$) are (in k_BT units)

$$\beta U_m(a) = Z^2 \frac{\lambda_B}{2a} \tag{4.25}$$

and

$$\beta \left\langle \frac{\partial U_{m\mu}(a)}{\partial a} \right\rangle = \frac{Z\lambda_B}{a^2} \sum_{i(r_i \leq a)} z_i. \tag{4.26}$$

Substituting Equations (4.25) and (4.26) into Equation (4.7) yields

$$\beta\pi_e v = -\frac{\lambda_B}{3a}\left(\frac{-Z^2}{2} + Z\left(\langle N_+\rangle - \langle N_-\rangle\right)\right), \tag{4.27}$$

where $v = \frac{4\pi}{3}a^3$ is the volume of the microgel and

$$\langle N_\pm\rangle = 4\pi\int_0^a r^2 n_\pm(r)dr \tag{4.28}$$

are mean counterion/coion numbers inside the microgel.

4.1.3. Cylindrical Ionic Microgels

The cylindrical cell model has been used to model polyelectrolyte solutions and suspensions of charged rodlike colloidal particles [108, 114]. In this study, two permeable cylindrical ionic microgels systems are considered: cylindrical gel of cross-sectional radius a and fixed charge per unit length $-\lambda$ ($\lambda = -Z/h$) uniformly spread over the surface with number density,

$$n_f(r) = \frac{\lambda}{2\pi a}\,\delta(r-a) \tag{4.29}$$

and a cylindrical microgel with fixed charge per unit length uniformly distributed over its volume with number density

$$n_f(r) = \frac{\lambda}{\pi a^2}\theta(r-a). \tag{4.30}$$

The $\theta(r-a)$ in Equation (4.30) represents the Heaviside function (also known as the step function) and formally can be expressed as

$$\theta(r-a) = \begin{cases} 0, & \text{if } r < a \\ 1, & \text{if } r > a. \end{cases} \tag{4.31}$$

Following the approach developed previously to spherical microgel and considering that the cylinder swells in axial and radial directions. The following subsections represent some exact statistical mechanical relations for the electrostatic contribution to the osmotic pressure of an ionic cylindrical microgel in the cell model.

4.1.3.1. Surface-Charged Cylindrical Microgels

The pair potential between microions and a cylindrical microgels can be expressed as (in k_BT units)

$$v_{m\mu}(r) = \begin{cases} 2\lambda\lambda_B z \ln(r/R), & r > a \\ \\ 2\lambda\lambda_B z \ln(a/R), & r \leqslant a \end{cases} \tag{4.32}$$

For a cylindrical microgel with uniform surface charge density, whose fixed charge is described by Equation (4.29), the self-energy and microgel-microion interaction energy inside the microgel ($r \leqslant a$) per unit length are (in k_BT units)

$$U_m = -\lambda_B \lambda^2 \ln\left(\frac{a}{R}\right), \tag{4.33}$$

and

$$U_{m\mu} = 2\lambda\lambda_B \ln\left(\frac{a}{R}\right) \sum_{i(r_i \leq a)} z_i. \tag{4.34}$$

Substituting Equations (4.33) and (4.34) into Equation (4.8) yields the electrostatic contribution to the osmotic pressure in the radial direction

$$\pi_r = \frac{\lambda\lambda_B}{2\pi a^2}\left(\lambda - 2\left(\langle N_+\rangle - \langle N_-\rangle\right)\right), \tag{4.35}$$

where

$$\langle N_\pm\rangle = 2\pi \int_0^a r\, n_\pm(r) dr \tag{4.36}$$

are the mean numbers of counterions/coions per unit length inside the microgel and $n_\pm(r)$ are the mean number densities of of counterions/coions inside the microgel. From Equation (4.9), the electrostatic osmotic pressure in the axial direction is

$$\pi_a = -\frac{\lambda\lambda_B}{\pi a^2} \ln\left(\frac{a}{R}\right)\left(\lambda - 2\Big(\langle N_+\rangle - \langle N_-\rangle\Big)\right). \tag{4.37}$$

Note that the main difference between the radial and axial pressure equations is that the axial pressure equation involves a logarithmic function. However, this difference palys a significant role in determining the equilibrium swollen size of a microgel.

4.1.3.2. Volume-Charged Cylindrical Microgels

For a cylindrical microgel with fixed charge uniformly distributed over its volume, the pair potential between microions and the microgel is given by (in k_BT units),

$$v_{m\mu}(r) = \begin{cases} 2\lambda\lambda_B z \ln(r/R), & r > a \\ 2\lambda\lambda_B z(\frac{R^2}{a^2} - 1), & r \leq a. \end{cases} \tag{4.38}$$

The self-energy for a cylindrical microgel with charge number density described by Equation (4.30) and microgel-microion interaction energy per unit length are (in k_BT units)

$$U_m = \lambda^2 \lambda_B \left[\frac{1}{4} - \ln\left(\frac{a}{R}\right) \right] \tag{4.39}$$

$$U_{m\mu} = 2\lambda\lambda_B \sum_{i(r_i \leq a)} z_i \left[\ln\left(\frac{a}{R}\right) + \frac{r_i^2}{2a^2} \right]. \tag{4.40}$$

Substituting Equations (4.39) and (4.40) into Equation (4.8) yields the electrostatic contribution to the osmotic pressure in the radial direction

$$\pi_r = \frac{\lambda\lambda_B}{\pi a^2} \left(\frac{\lambda}{2} - \langle N_+ \rangle + \langle N_- \rangle + \frac{\langle r^2 \rangle_+ - \langle r^2 \rangle_-}{a^2} \right). \tag{4.41}$$

From Equation (4.9), the electrostatic osmotic pressure in the axial direction is

$$\pi_a = \frac{\lambda\gamma}{\pi a} \left(\lambda \left(\frac{1}{4} - \ln\left(\frac{a}{R}\right) \right) + 2\ln\left(\frac{a}{R}\right) \left(\langle N_+ \rangle - \langle N_- \rangle \right) + \frac{\langle r^2 \rangle_+ - \langle r^2 \rangle_-}{a^2} \right) \tag{4.42}$$

where

$$\langle r^2 \rangle_\pm = 2\pi \int_0^a r^3 n_\pm(r) dr \tag{4.43}$$

are second moments of $n_\pm(r)$ inside the microgel.

4.2. Flory-Rehner Theory

The aim of using Flory-Rehner theory is to compute the gel contribution to the osmotic pressure of the microgel particles. Flory-Rehner theory combines the Flory-Huggins theory of

solution thermodynamics with rubber elasticity theory. The theory rests on two basic assumptions: the interactions between the constituent chains are independent of the state of deformation, and microgel chains exhibit a Gaussian distribution (excluded volume interactions are ignored) [115]. Although the Flory-Rehner theory was originally developed to describe the equilibrium swelling characteristics of macroscopic (bulk) gels [43, 115–117], the theory has been proven to model the swelling behavior of microgel particles [4, 26, 44, 118]. More recently, Lopez and Richtering [118] discussed the use of Flory-Rehner theory for studying the swelling of thermoresponsive microgels. The authors conclude that the Flory-Rehner model succeeds in describing microgel swelling well at high cross-linking densities, but fails to give a quantitative description of experimental data at low cross-linking densities [118]. Nevertheless, the theory provides a basis for understanding microgel swelling and deswelling.

The Flory-Rehner theory assumes linear superposition of the free energy associated with the swelling of a neutral gel network:

$$F_g = F_{\text{mix}} + F_{\text{elastic}}, \tag{4.44}$$

where F_{mix} and F_{elastic}, represent the free energies of mixing and of rubber elasticity, respectively. The mixing free energy accounts for the attraction of solvent molecules to the polymer network and can be described by the Flory–Huggins equation,

$$F_{mix} = U_{\text{mix}} - TS_{\text{mix}} \tag{4.45}$$

or (in k_BT unit)

$$\beta F_{\text{mix}} = N_{\text{s}}[(1-\phi_p)\ln(1-\phi_p) + \chi\phi_p(1-\phi_p)], \tag{4.46}$$

where N_{s} is the number of solvent molecules, ϕ_p is volume fraction of polymer gel, and χ is the Flory or Flory–Huggins solvency parameters derived from polymer-polymer, the polymer-solvent, and solvent-solvent interactions. The volume fraction of polymer gel can be expressed as

$$\phi_p = \frac{a_0^3}{a^3} = \frac{1}{\alpha^3}, \tag{4.47}$$

and Flory–Huggins solvency parameters has the form (in k_BT units)

$$\chi = z\left(w_{12} - \frac{w_{11} + w_{22}}{2}\right), \tag{4.48}$$

where. This quantity is very important to model experimental data accurately since χ depends on temperature and concentration through,

$$\chi = \frac{1}{2} - A\left(1 - \frac{\theta}{T}\right) + C\phi_p + D\phi_p^2, \tag{4.49}$$

where θ is the theta temperature and A, C, and D are fit parameters. The Flory solvency parameter for PNIPAM microgels is $\chi < 0.5$ in water [118]. If $\chi > 0$, polymer-slovent mixing is not energetically favorable. In contrast, if $\chi < 0$, polymer-slovent mixing is energetically favorable. Depending on the value of χ, the polymer may behave like an athermal or ideal Gaussian chain. When $\chi = 0$, the polymer conformation depends only on the excluded-volume interactions between the monomers, so the polymer behaves athermally. When $\chi = 1/2$, the polymer behaves like an ideal Gaussian chain, due to a blance between the excluded-volume repulsion and the hydrophobic attraction between the polymer chains. For larger values of χ, the polymer tends to be more hydrophobic, so the microgel shrinks expelling, the solvent molecules from inside. The larger χ is, the smaller the microgel size becomes.

The elastic free energy can be expressed as

$$F_{elastic} = H_{elastic} - TS_{elastic} \tag{4.50}$$

where $H_{elastic}$ are the enthalpy of the network which is negligible (due to no change in internal free energy of the network) and $S_{elastic}$ is the entropy due to configurationl change of the network. From the statistical theory of rubber elasticity [43],

$$\beta F_{el} = -TS_g = \frac{\nu_v}{2}\left[\alpha_x^2 + \alpha_y^2 + \alpha_z^2 - 3 - \ln(\alpha_x\alpha_y\alpha_z)\right], \tag{4.51}$$

where α_x is the linear swelling ratio in the x-direction, α_y is the linear swelling ratio in the y-direction, and α_z linear swelling ratio in z-direction, and ν_v is the effective number of chains in

the network. For an isotropic network, where the swelling is independent of the orientation of the polymer, $\alpha_x = \alpha_y = \alpha_z = \alpha$, as in the spherical microgel case, the elastic free energy can be expressed as

$$F_{elastic} = \frac{3}{2} N_{\rm ch}(\alpha^2 - \ln\alpha - 1). \tag{4.52}$$

For an anisotropic swelling network, where the swelling is dependent on the orientation of the polymer (where $\alpha_r = \alpha_x{=}\alpha_y \neq \alpha_z = \alpha_a$) as in the cylindrical microgel case, the elastic free energy can be expressed as

$$\beta F_{elastic} = \frac{1}{2} N_{\rm ch}\left(2\alpha_r^2 + \alpha_a^2 - 3 - \ln(\alpha_r^2\alpha_a)\right), \tag{4.53}$$

where $N_{\rm ch}$ is the number of cross-linked chains. Finally, the gel free energy associated with the isotropic swelling of a polymer network, obtained by the addition of Equations (4.46) and (4.52) can be written as

$$\beta F_g = N_{\rm mon}\left[(\alpha^3 - 1)\ln\left(1 - \alpha^{-3}\right) + \chi\left(1 - \alpha^{-3}\right)\right] + \frac{3}{2} N_{\rm ch}\left(\alpha^2 - \ln\alpha - 1\right), \tag{4.54}$$

while the gel free energy associated with the anisotropic swelling of a cylindrical polymer network, obtained by the addition of Equations (4.46) and (4.53), can be written as

$$\beta F_g = N_{\rm mon}\left[(\alpha_a\alpha_r^2 - 1)\ln\left(1 - \alpha_a^{-1}\alpha_r^{-2}\right) + \chi\left(1 - \alpha_a^{-1}\alpha_r^{-2}\right)\right] + \frac{1}{2} N_{\rm ch}\left(2\alpha_r^2 + \alpha_a^2 - 3 - \ln(\alpha_r^2\alpha_a)\right). \tag{4.55}$$

The first term on the right-hand side accounts for mixing contribution between solvent and polymer, the second term interaction of solvent/polymer, and the last term elastic contributions. The elasticity of microgel particles strongly depends on the average chain length. Short chains imply that the particle has a larger cross-linker concentration, and so it is more difficult to stretch. On the contrary, for long chains, the microgel is likely to be deformed by any external stimuli with a relatively small elastic free energy cost. The internal structure of the microgel and the elastic response depends on the number of monomers $N_{\rm mon}$. Assuming that monomers have a spherical shape of radius $r_{\rm mon}$, the number of monomers is given by

$$N_{\rm mon} = 0.61\frac{v_0}{v_{\rm mon}}, \tag{4.56}$$

where v_0=$4\pi a_0^3/3$ is the dry volume of the microgel, and v_{mon}= $4\pi r_{\text{mon}}^3/3$ is the volume of a monomer, and (0.61) is used to ensure that the volume fraction of the monomers is below the volume fraction for random-close-packing of hard spheres, which is 0.64.

The total gel osmotic pressure π_g is expressed as

$$\pi_g = \pi_{\text{mix}} + \pi_{\text{elastic}}, \tag{4.57}$$

where π_{mix} denotes the osmotic pressure due to mixing, and π_{elastic} that due to rubber elasticity. The gel osmotic pressure π_g is obtained from the gel free energy via

$$\pi_g = -\left(\frac{\partial}{\partial v} F_g\right). \tag{4.58}$$

From Equations (4.54) and (4.55) and using Equation (4.58), the gel pressure of a spherical microgel is expressed as

$$\beta\pi_g(\alpha)v = -N_{\text{mon}}\left[\alpha^3 \ln\left(1-\alpha^{-3}\right) + \chi\alpha^{-3} + 1\right] - N_{\text{ch}}\left(\alpha^2 - \frac{1}{2}\right), \tag{4.59}$$

and for a cylindrical microgel the radial and axial gel pressures are, respectively,

$$\beta\pi_g(\alpha_r,\alpha_a)v = -N_{\text{mon}}\left[\alpha_a\alpha_r^2 \ln\left(1-\alpha_a^{-1}\alpha_r^{-2}\right) + \chi\alpha_a^{-1}\alpha_r^{-2} + 1\right] - N_{\text{ch}}\left(\alpha_r^2 - \frac{1}{2}\right) \tag{4.60}$$

and

$$\beta\pi_g(\alpha_r,\alpha_a)v = -N_{\text{mon}}\left[\alpha_a\alpha_r^2 \ln\left(1-\alpha_a^{-1}\alpha_r^{-2}\right) + \chi\alpha_a^{-1}\alpha_r^{-2} + 1\right] - N_{\text{ch}}\left(\alpha_a^2 - \frac{1}{2}\right). \tag{4.61}$$

As mentioned before, the condition of thermodynamic equilibrium is that the total osmotic pressure vanishes. It is seen from Equations (4.59) and (4.60) that, within the framework of the present theory, the cross-link concentration and the Flory solvency parameter determine the swelling ratio of a neutral microgel, and only χ responds to changes in external conditions.

4.3. Poisson-Boltzmann Theory

Computing the electrostatic osmotic pressure of an ionic microgel requries knowing the mean numbers of interior counterions/coions $\langle N_{\pm} \rangle$ and second moments of the interior microion density profiles $\langle r^2 \rangle_{\pm}$. We used Poisson-Boltzmann (PB) theory to computed the microion density profiles, from which $\langle N_{\pm} \rangle$, $\langle r^2 \rangle_{\pm}$, and the corresponding electrostatic osmotic pressure are obtained. PB theory has been widely applied to model interfaces between charged surfaces and ionic solutions, including ionic microgel solutions [40, 108, 119, 120]. It is a good approximation at ionic strengths about 0.1M and for monovalent (weakly correlated) electrolytes [121]. The theory is a mean-field theory and its derivation is based on several assumptions as follows: the charge densities are represented as smoothly varying functions. The nature of the ions is not taken into account, and no other molecular interaction between the ions and solvent is considered. The ion-ion correlations are also neglected. The ion distributions are represented by their thermal averages. Despite all of these limitaions, the theory provides reasonable quantitative results. A good review of the scope and impact of these deviations from PB theory can be found in [122].

There are several derivations of the Poisson-Boltzmann equation based on statistical mechanics. The simplest derivation starts with Poisson's Equation (1.2),

$$\nabla^2 \phi(r) = -\frac{n(r)}{\epsilon}. \tag{4.62}$$

In a mean-field approximation, the distributions of all ions in the solution follow a Boltzmann distribution:

$$f(r) = Ae^{-\beta U(r)}, \tag{4.63}$$

where A is a normalization constant and U is the electrostatic potential energy. With electrostatic potential energy ($ze\phi(r)$), the Boltzmann distribution becomes

$$n_i = n_0 e^{-z_i e\phi(r)/k_B T}. \tag{4.64}$$

Combining Poisson's equation for the electrostatic potential with the Boltzmann distributions for ion densities yields the Poisson-Boltzmann equation in spherical ($d = 3$) and cylindrical ($d = 2$)

polar coordinates,

$$\psi''(r) + \frac{d-1}{r}\psi'(r) = \kappa^2 \sinh\psi(r) + 4\pi\lambda_B n_f(r), \tag{4.65}$$

which is a second-order nonlinear elliptic partial differential equation. Here $\psi(r) = e\phi(r)/k_BT$, is a dimensionless potential and $\kappa = \sqrt{8\pi\lambda_B n_0}$ is the Debye screening constant, which is proportional to the square-root of ionic strength of the solution. Through this parameter, the effects of electrolyte ions on the electrostatic potential are captured. For weak electric fields, Equation (4.65) is simplified to the linearized PB equation by replacing the $\sinh\psi(r)$ term with its first-order approximation, $\sinh\psi(r) = \psi(r)$, to give (in spherical ($d = 3$) polar coordinates)

$$\psi''(r) + \frac{2}{r}\psi'(r) = \kappa^2\psi(r) + 4\pi\lambda_B n_f(r). \tag{4.66}$$

In general, solving the Poisson-Boltzmann equation for the electrostatic potential requries specifying suitable boundary conditions. The cell model is a good approximation, whose boundary conditions are relatively simple. The Poisson-Boltzmann equation for a microcapsule microgel, whose fixed charge is described by

$$n_f(r) = \begin{cases} 0, & r \leqslant a \\ \frac{3Z}{4\pi(b^3-a^3)}, & a < r \leqslant b \\ 0, & b < r \leqslant R, \end{cases} \tag{4.67}$$

can be expressed as

$$\psi''(r) + \frac{2}{r}\psi'(r) = \begin{cases} \kappa^2 \sinh\psi(r), & 0 < r \leqslant a \\ \kappa^2 \sinh\psi(r) + \frac{3Z\lambda_B}{b^3-a^3}, & a < r \leqslant b \\ \kappa^2 \sinh\psi(r), & b < r \leqslant R. \end{cases} \tag{4.68}$$

Substituting Equation (4.22) into Equation (4.65) yields a Poisson-Boltzmann equation for a surface-charged spherical microgel,

$$\psi''(r) + \frac{2}{r}\psi'(r) = \kappa^2 \sinh\psi(r) + \frac{Z\lambda_B}{a^2}\,\delta(r-a). \tag{4.69}$$

Substituting Equation (4.30) into Equation (4.65) yields a Poisson-Boltzmann equation for a cylindrical microgel with fixed charge per unit length $(-\lambda e)$ uniformly distributed over its volume,

$$\psi''(r) + \frac{1}{r}\psi'(r) = \kappa^2 \sinh \psi(r) + \frac{\lambda}{\pi a^2}\theta(r-a). \tag{4.70}$$

Similarly, substituting Equation (4.29) into Equation (4.65) yields a Poisson-Boltzmann equation for a surface-charged cylindrical microgel

$$\psi''(r) + \frac{1}{r}\psi'(r) = \kappa^2 \sinh \psi(r) + \frac{\lambda}{2\pi a}\,\delta(r-a). \tag{4.71}$$

Equations (4.68), (4.69), (4.70), and (4.71) are subject to the boundary conditions: the electric field must vanish at the center of the cell $\psi'(0) = 0$ (by symmetry) and on the cell boundary $\psi'(R) = 0$ (by electroneutrality). In the microcapsule case, Equation (4.68) also is subjected to the continuity conditions of the shell interfaces, $\psi_{cav}(a) = \psi_{sh}(a), \psi_{sh}(b) = \psi_{out}(b)$. The subscripts "$cav$", "$sh$", and "$out$" label the solutions in the cavity, shell, and outer regions, respectively. Within the cell model implementation, and using these boundary conditions, the PB Equations (4.68), (4.69), (4.70), and (4.71) are numerically solved by using the ParametricNDSolve solver in Mathematica, from which the ion density profiles, and the corresponding electrostatic osmotic pressures are computed.

Finally, it is important to emphasize that our PB theoretical calculations are well below the threshold for Manning condensation onto polyelectrolyte chains ($\frac{\lambda_B}{l} < 1$), where l is the distance between neighboring charged monomers. If $\lambda_B/l > 1$, the Coulomb interactions dominate over the thermal fluctuations and counterion condensation is favored. In the case of surface-charged spherical microgels, the counterion condensation condition is defined as

$$\left(\frac{4\pi a^2}{Z}\right)^{1/2} > \lambda_B \tag{4.72}$$

or

$$\frac{Z\lambda_B^2}{4\pi a^2} < 1. \tag{4.73}$$

In the case of surface-charged cylindrical microgels, the distance between neighboring charged monomers can be expreesed as

$$l = \left(\frac{2\pi ah}{Z}\right)^{1/2} > \lambda_B. \tag{4.74}$$

By using ($Z/h = \lambda$), the threshold for counterion condensation onto surface-charged cylindrical microgels would be

$$\frac{\lambda\lambda_B^2}{2\pi a} < 1. \tag{4.75}$$

Similarly, the counterion condensation limit for volume-charged cylindrical microgels is

$$l = \left(\frac{\pi a^2 h}{Z}\right)^{1/3} > \lambda_B \tag{4.76}$$

or

$$\frac{\lambda\lambda_B^3}{\pi a^2} < 1. \tag{4.77}$$

For example, if $\lambda_B = 0.7$ nm, $Z = 1000$, and $a = 30$ nm, the counterion condensation limit for spherical microgels with uniformm surface charge (Equation (4.73)) would be $0.043 < 1$. For a surface-charged cylindrical microgel with $\lambda = 500$, Equation (4.75) gives 1.29 and for a volume-charged cylindrical microgel with same parameters, Equation (4.77) gives $0.06 < 1$.

4.4. Effective Interactions of Ionic Microgel Suspensions

Suspensions of ionic colloidal particles are multi-component mixtures of microscopic particles, macroions, counterion, coions, and solvent molecules. It is often practical to view microgel suspensions as one-component "microgel-only" systems described by effective microgel interactions in which the presence of microions appears only through medium properties, such as the dielectric constant and the Debye screening constant. For the model suspension described in Chapter 3, the goal is to derive a statistical-mechanical approach based on the one-component model and linear response theory to describe effective electrostatic interactions between the penetrable spherical microgels. The elastic contribution to the effective interaction potential was modeled using the Hertzian model of the theory of elasticity, allowing studying the interplay between the electrostatic and the elastic contributions to the effective interaction potential. Combing the theory of effective interactions with Monto Carlo simulations gives access to radial distribution functions, static struc-

ture factors, and phase behavior of ionic microgels, which cannot be obtained from the cell model. Finally, the theory with Monto Carlo simulations aims at the understanding of phase behavior of ionic microgel solutions.

By following Denton's statistical mechanical framework of charged colloidal suspensions [42], the Hamiltonian of a model system containing only one species of surface-charged microgels suspended in a solvent with only counterions (no salt), as described in 3.4, can be expressed as

$$H = H_{mm} + H_{cc} + H_{mc}, \tag{4.78}$$

where H_{mm} is the electrostatic energy of interaction between microgels, H_{mc} describes the microgel–counterion interaction energy, and H_{cc} is the counterion-counterion interaction energy. Explicitly, these terms are of the form

$$H_{mm} = K_{\mathrm{m}} + \frac{1}{2} \sum_{i \neq j=1}^{N_m} v_{mm}\left(r_{ij}\right) \tag{4.79}$$

$$H_{cc} = K_c + \frac{1}{2} \sum_{i \neq j=1}^{N_c} v_{cc}\left(r_{ij}\right) \tag{4.80}$$

$$H_{mc} = \sum_{i=1}^{N_m} \sum_{j=1}^{N_c} v_{mc}\left(r_{ij}\right), \tag{4.81}$$

where K_{m} and K_c are the microgel and counterion kinetic energies, respectivlty, and v_{mm} is the bare Coulomb pair interaction potential between two microgels at center-center separation r_{ij}, which reads as

$$v_{mm}(r_{ij}) = \frac{Z^2 e^2}{\epsilon r_{ij}}, \quad r_{ij} > a_i + a_j \tag{4.82}$$

Since the counterions are modeled as point particles, they interact via the Coulomb potential expressed as

$$v_{cc}(r_{ij}) = \frac{z^2 e^2}{\epsilon r_{ij}}. \tag{4.83}$$

The electrostatic potential energy between a microgel and a counterion $v_{mc}(r)$ will be considered in detail later.

The partition function $\mathcal{Z}$ of the mixture is the canonical double trace over microgel and counterion coordinates. By integrating out the counterion coordinates, the mixture is reduced to an equivalent one-component system. The canonical partition function can be expressed as

$$\mathcal{Z} = \langle\langle \exp(-\beta H)\rangle_c\rangle_m = \langle \exp\left(-\beta H_{\text{eff}}\right)\rangle_m \,, \tag{4.84}$$

where H_{eff} is the effective Hamiltonian, which depends only on microgel degrees of freedom and $\langle\rangle_m$ and $\langle\rangle_c$ denote traces over microgel and counterion coordinates, respectively. The effective Hamiltonian can be expressed as

$$H_{\text{eff}} = H_{mm} + F_c, \tag{4.85}$$

where F_c is the free energy of the counterions in the presence of the microgels:

$$F_c = -k_B T \ln \langle \exp\left[-\beta\left(H_{cc} + H_{mc}\right)\right]\rangle_c \,. \tag{4.86}$$

Evaluating the trace over counterion coordinates is technicaly difficult since $(H_{cc} + H_{mc})$ contains counterion–microgel and counterion–counterion Coulombic interactions and violates the charge neutrality of the system. Therefore, the self-energy of a uniform, neutralizing background,

$$E_b = -N_c n_c \hat{v}_{cc}(0)/2, \tag{4.87}$$

is added to H_{mc} and subtracted from H_{cc}, where $n_c = N_c/V$ is the average density of counterions and $\hat{v}_{cc}(0)$ is the $k \longrightarrow 0$ limit of the Fourier transform of $v_{cc}(r)$. By using this technique, the counterion system in the presence of the frozen microgels can be treated as a perturbation around the one-component plasma (OCP) [123–125]. Equation (4.86) then can be calculated via an expansion around this reference state,

$$F_c = F_0 + \int_0^1 \mathrm{d}\lambda \, \langle H_{mc}\rangle_\lambda \tag{4.88}$$

or

$$F_c = F_{\text{OCP}} + \int_0^1 \mathrm{d}\lambda \, \langle H_{mc}\rangle_\lambda - E_b, \tag{4.89}$$

where $F_0 = -k_B T \ln \langle \exp(-\beta H_c) \rangle_c$ is the reference free energy of the unperturbed counterions, $F_{\mathrm{OCP}} = F_0 + E_b$ is is the free energy of a homogeneous OCP excluded from the colloidal hard cores and λ is a charging parameter that scales the charge of the microgels, whereas the expectation value $\langle ... \rangle$ is carried over the counterions' degrees of freedom. Additional progress is now made by employing linear response theory [62], which allows to calculate the counterion response to the microgel density. The counterions are assumed to respond linearly to the macroion external potential:

$$\hat{\rho}_c(\mathbf{k}) = \chi(k)\hat{v}_{mc}(k)\hat{\rho}_m(\mathbf{k}), \quad k \neq 0, \tag{4.90}$$

where the ($\hat{}$) denotes a Fourier transform, $\hat{\rho}_c(\mathbf{k})$ and $\hat{\rho}_m(\mathbf{k})$ are the density operators of the counterions and the microgels in inverse space, $\hat{v}_{mc}(k)$ is the Fourier transform of the microgel-counterion interaction, and $\chi(k)$ is the linear response function of the OCP. In Equation (4.90), the term $k = 0$ is excluded since the counterion number density at $k = 0$ is fixed by the number of counterions, $N_c = \hat{\rho}_c(0)$. Therefore, there is no response to the microgel charge when $k = 0$, and $\hat{\rho}_c(0)$ is fixed by the constraint of global charge neutrality. The linear response function $\chi(k)$ is defined as

$$\chi(k) = -\beta n_{\mathrm{c}} S(k), \tag{4.91}$$

where $S(k)$ is static structure factor. Using the Ornstein-Zernike relation, the static structure factor can be sxpressed as

$$S(k) = 1/\left[1 - n_c \hat{c}(k)\right], \tag{4.92}$$

where $\hat{c}(k)$ is the Fourier transform of the direct correlation function $c(r)$. For a weakly-coupled plasma, a reasonable approximation for $c(r)$ can be made by setting $c(r)$ equal to its asymptotic ($r \to \infty$) limit $\hat{c}(k) \cong -\beta \hat{v}_{\mathrm{cc}}(k)$ for all r. Therefore,

$$\hat{c}(k) \simeq -\beta \hat{v}_{\mathrm{cc}}(k) = -\frac{4\pi\beta z^2 e^2}{\epsilon k^2}. \tag{4.93}$$

Substitution of EquationS (4.92) and (4.93) into Equation (4.91) then yields [126]

$$\chi(k) = -\frac{\beta n_{\mathrm{c}}}{1 + \kappa^2/k^2}, \tag{4.94}$$

where κ is the inverse Debye screening length, which plays an important role in the microion density profiles and in the effective pair interaction. It has the form

$$\kappa = \sqrt{4\pi n_c z^2 \lambda_B}. \tag{4.95}$$

Returning to the effective Hamiltonian [Equation (4.85)], the full form of the effective Hamiltonian of a one-component system then is

$$H_{\text{eff}} = K_{\text{m}} + \frac{1}{2} \sum_{i \neq j=1}^{N_m} v_{\text{eff}}\left(r_{ij}\right) + E_0, \tag{4.96}$$

where $v_{\text{eff}}(r_{ij})$ is an effective electrosatic microgel-microgel pair interaction potential, which is described by two different mathematical expressions, one for overlaps particles and one for non-overlapping particles,

$$v_{\text{eff}}(r) = \begin{cases} v_Y(r), & r > a_i + a_j \\ \\ v_{\text{ov}} + v_{\text{H}}(r), & r \leqslant a_i + a_j, \end{cases} \tag{4.97}$$

where $v_Y(r)$ is an effective Yukawa (screened-Coulomb) pair potential for non-overlapping microgels, which can be expressed as

$$v_Y(r) = A\frac{e^{-\kappa r}}{r}, \quad r > a_i + a_j, \tag{4.98}$$

where the prefactor A depends on microgel charge and size. The Yukawa potential has been widely used in simulation studies of charged colloids. The $v_{\text{ov}}(r)$ term of Equation (4.97) denotes the effective electrostatic pair potential for overlapping microgels and $v_{\text{H}}(r)$ is the elastic Hertz potential, which will be discussed later in this section. The effective electrostatic pair potential for overlapping microgels $v_{\text{ov}}(r)$ splits into

$$v_{\text{ov}}(r) = v_{mm}(r) + v_{\text{ind}}(r), \tag{4.99}$$

where $v_{\text{ind}}(r)$ is an induced interaction acting between the microgels caused by the presence of the counterions. The counterion-induced interaction takes the form

$$\hat{v}_{\text{ind}}(k) = \chi(k) \left[\hat{v}_{mc}(k)\right]^2 . \tag{4.100}$$

The last term in the effective Hamiltonian in Equation (4.96) is the volume energy, which takes the form

$$E_0 = F_{\text{OCP}} + \frac{N_m}{2} \lim_{r\to 0} v_{\text{ind}}(r) + N_m \lim_{k\to 0} \left[-\frac{1}{2} n_m \hat{v}_{\text{ind}}(k) + n_c \hat{v}_{mc}(k) + \frac{Z}{2z} n_c \hat{v}_{cc}(k) \right], \tag{4.101}$$

where $n_m = N_m/V$ and $n_c = N_c/V$ are number densities of microgels, and counterions respectively. The volume energy is a one-body property, which arises naturally from the one-component reduction and has no explicit dependence on microgel coordinates. It evidently depends on the average microgel density and therefore has the potential to significantly influence thermodynamics properties. Such a quantity is quite common when tracing out microscopic degrees of freedom. It appears for metallic systems as a result of integrating out the electrons [127] and for other classical charged systems, such as charge hard colloids and polyelectrolyte stars [91, 101, 128, 129]. It is very important to point out that a crucial difference between microgels and charge hard colloids is that counterions can penetrate inside the charged microgel, whereas they cannot penetrate charge hard colloids.

Although salt ions have been taken into consideration in this study, they can be easily incorporated by introducing additional response functions [41]. Then, the effective pair interaction and volume energy E_0 are adapted only through a redefinition of the inverse Debye screening length to take into account the effects of added salt ions [41]:

$$\kappa = \sqrt{4\pi \left(n_c + 2n_s\right) z^2 \lambda_B}. \tag{4.102}$$

Finally, the nonlinear effect of microion response in the response theory is not taken into consideration, since it is only significant in concentrated, deionized suspensions of highly charged microgels [41, 130].

Returning to the elastic contribution of microgels, the effective elastic interactions can be modeled using the Hertz potential [43], which reads as

$$v_{\mathrm{H}}(r) = \begin{cases} B_{ij}\left(1 - \frac{r}{a_i + a_j}\right)^{5/2}, & r \leq a_i + a_j \\ 0, & r > a_i + a_j, \end{cases} \tag{4.103}$$

where B_{ij} is the Hertz amplitude:

$$B_{ij} = \frac{8}{15}\left(\frac{1-\nu_i^2}{Y_i} + \frac{1-\nu_j^2}{Y_j}\right)^{-1}(a_i + a_j)^2\sqrt{a_i a_j}. \tag{4.104}$$

B_{ij} depends on the elastic properties of the microgel through Young's modulus Y and Poisson's ratio ν [43]. The Young's modulus and Poisson's ratio are related to each other via

$$Y = 3K(1 - 2\nu), \tag{4.105}$$

where K is the bulk modulus. In the case of microgel suspensions of equal radii and equal elastic constants (Y, ν), the Hertz amplitude simplifies to

$$B = \frac{16Ya^3}{15\,(1-\nu^2)}. \tag{4.106}$$

With these considerations, the presentation of the effective coarse-grained description of ionic microgel suspensions is completed. Bulk thermodynamic and structural properties, such as microgel-microgel radial distribution functions, static structure factors, and microgel contributions to the osmotic pressure can then be calculated by inputting the effective interactions [Equation (4.97)] and volume energy [Equation (4.101)] into statistical mechanical theories or simulations of the one-component model.

4.4.1. Effective Interactions between Similar Ionic Microgels

Using the theoretical framework derived above, the effective interactions and volume energy between two spherical microgels of equal size are derived. The model of interest is described in

section 3.4. For such a model, The electric field of a uniformly charged sphere is

$$E(r) = \begin{cases} -\frac{Ze}{\epsilon r^2}, & r > a \\ \\ -\frac{Zer}{\epsilon a^3}, & r \leqslant a, \end{cases} \tag{4.107}$$

which yields the microgel-counterion interaction

$$v_{\mathrm{mc}}(r) = \begin{cases} -\frac{Zze^2}{\epsilon r}, & r > a \\ \\ -\frac{Zze^2}{\epsilon a}, & r \leqslant a. \end{cases} \tag{4.108}$$

Fourier transformating Equation (4.108) gives

$$\hat{v}_{mc}(\mathbf{k}) = -\frac{4\pi Zze^2}{\epsilon k^3 a}\sin(ka). \tag{4.109}$$

The inverse-space counterion density profile $\hat{\rho}_c(\mathbf{k})$ around a single microgel (in the dilute limit, where $\hat{\rho}_m(\mathbf{k})$=1) may be determined from Equations (4.90), (4.94), and (4.108):

$$\hat{\rho}_c(\mathbf{k}) = \frac{\beta n_c}{(1+\kappa^2/k^2)}\frac{4\pi Zze^2}{\epsilon k^3 a}\sin(ka), \quad k \neq 0. \tag{4.110}$$

Now inverse Fourier transforming Equation (4.110) yields the real-space counterion density profile,

$$\rho_c(r) = \frac{Zze^2\beta n_c}{\epsilon\kappa a}\frac{e^{-\kappa r}}{r}\sinh(\kappa a), \quad r > a. \tag{4.111}$$

From Equations (4.108) and (4.100), the induced electrostatic pair interaction is given by

$$\hat{v}_{\mathrm{ind}}(k) = -\frac{\beta n_c}{(1+\kappa^2/k^2)}\left[\frac{4\pi Zze^2}{\epsilon k^3 a}\sin(ka)\right]^2. \tag{4.112}$$

By inverse Fourier transforming Equation (4.112), the real-space counterion-induced pair potential between two nonoverlapping ($r \geq 2a$) or overlapping ($r < 2a$) uniformly surface-charged ionic

microgels is (in units of k_BT)

$$\beta v_{\text{ind}}(r) = \begin{cases} Z_{\text{eff}}^2 \lambda_B \frac{e^{-\kappa r}}{r} - \beta v_{mm}(r), & r \geqslant 2a \\ \frac{Z^2 \lambda_B}{2\kappa^2 a^2 r}\left[1 + \frac{\kappa^2}{2}\left(r^2 - 4ra\right) - e^{-\kappa r} + e^{-2\kappa a}\sinh(\kappa r)\right], & 0 < r < 2a, \end{cases} \tag{4.113}$$

where

$$Z_{\text{eff}} \equiv Z\frac{\sinh(\kappa a)}{\kappa a} \tag{4.114}$$

represents an effective microgel valence (as $a \to 0, Z_{\text{eff}} \to Z$). The effective charges as a function of the bare microgel charge go to Z for low bare charges. Substituting this result for the induced pair potentials into Equation (4.99), the effective between nonoverlapping microgels pair potential is obtained as

$$\beta v_{\text{eff}}(r) = Z_{\text{eff}}^2 \lambda_B \frac{e^{-\kappa r}}{r}, \quad r \geqslant 2a. \tag{4.115}$$

Beyond the effective pair potential, the one-body volume energy can be determined from substituting Equations (4.109), (4.112), (4.113), and the Fourier transform of Equation (4.83),

$$\beta E_0 = \beta F_{\text{OCP}} + \frac{\lambda_B}{4\kappa a^2} N_m Z^2 \left(1 - 2\kappa a - e^{-2\kappa a}\right) - \frac{N_m^2 Z^2}{2 z_c^2 N_c}. \tag{4.116}$$

For the surface-charged microgel suspension model, the OCP is weakly correlated since the coupling parameter is

$$\Gamma = \lambda_B / a_c \ll 1, \tag{4.117}$$

where $a_c = (3/4\pi n_c)^{1/3}$ is the counterion sphere radius. To see that, for microgel of radius $a = 50\,\text{nm}$, valence $Z = 100$, and volume fraction $\phi = 0.01$, $\lambda_B = 0.714\,\text{nm}$, the coupling parameter is $\Gamma = 0.014$. Therefore, the first term on the right-hand side of Equation (4.116) can be approximated as the free energy of an ideal gas of counterions:

$$\beta F_{OCP} \simeq N_c \left[\ln\left(n_c \Lambda_c^3\right) - 1\right], \tag{4.118}$$

Λ_c being the thermal wavelength of the counterions. The second term of Equation (4.116) depends implicitly on the microgel density through the inverse Debye screening length κ, and may be given

a physical interpretation as self the electrostatic energy associated with a single pseudo-microgel. The third term of Equation (4.116) corresponds to the $k \to 0$ limit in Equation (4.101), and it has no influence on thermodynamic phase transitions when the salt concentration is zero.

The bare electrostatic Coulomb energy of interaction between two overlapping, uniformly surface-charged microgels is calculated as follows:

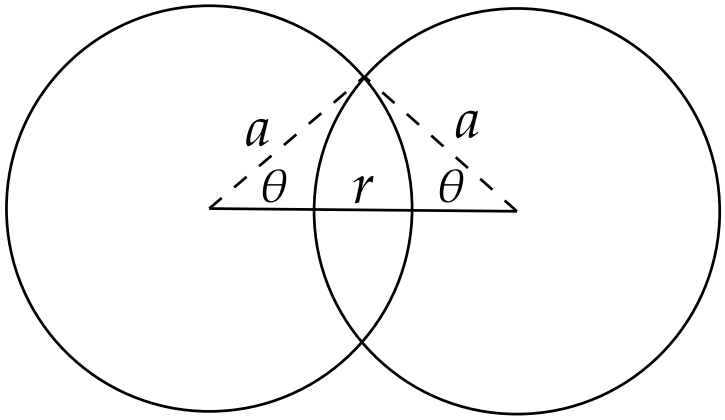

Figure 4.1. A representation of overlapping surface-charged microgels.

From the geometry of spheres (Figure 4.1), the area of the spherical cap, which is the portion of the surface of one microgel that intersects a second microgel, can be expressed as

$$A_{cap} = 2\pi a^2(1 - \cos\theta) \tag{4.119}$$

or, since $(\cos\theta = r/2a)$,

$$A_{cap}(r) = 2\pi a^2(1 - r/2a). \tag{4.120}$$

The bare electrostatic interaction between this portion of the surface of one microgel and the whole of the other microgel can then be obtained by multiplying $A_{cap}(r)$ by the surface charge density of the right sphere $\frac{Ze}{4\pi a^2}$, and the Coulomb potential of the left sphere $\frac{Ze}{a\epsilon}$ giving finally the interaction energy,

$$v_{mm}(r) = \frac{Z^2e^2}{2\epsilon a}(1 - r/2a), \quad r \leqslant 2a. \tag{4.121}$$

The contribution of the portion that lies outside the first microgel to the bare (Coulomb) energy of interaction between two microgels can be determined as following:

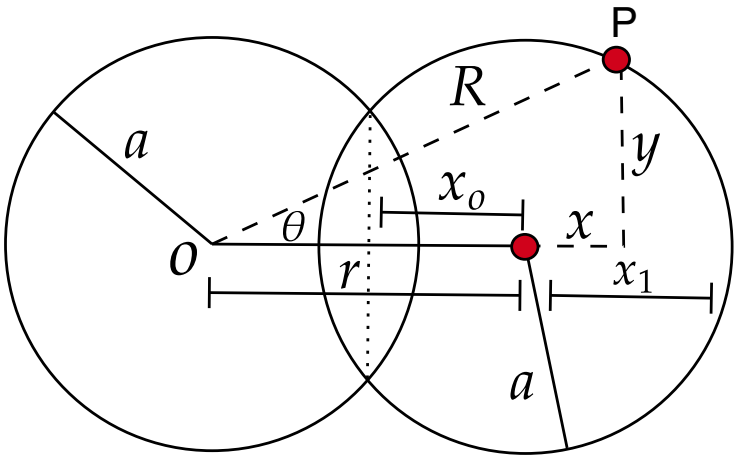

Figure 4.2. A representation of overlapping surface-charged microgels, where the y is the vertical distance between P and the line joining the centers of the two microgels, x is the horizontal distance between P and the ring of intersection of the two microgel surfaces, $x_0 = -r/2$, and $x_1 = a$.

From Figure 4.2, the area of the portion of the surface that lies outside the first microgel can be expressed by the integral,

$$A_{out} = \int_{x0}^{x1} 2\pi a dx. \tag{4.122}$$

The electrostatic (Coulomb) potential energy of a charge e at a point P on the surface of one microgel a distance R ($R > a$) from the center of a second microgel is

$$v_{mm}(r) = \frac{Z^2 e^2}{2a\epsilon} \int_{x0}^{x1} \frac{1}{R} dx. \tag{4.123}$$

After some substitutions, the above integral can be expressed as

$$v_{mm}(r) = \frac{Z^2 e^2}{2a\epsilon} \int_{-r/2}^{+a} \frac{1}{\sqrt{(r+x)^2 + a^2 - x^2}} dx, \tag{4.124}$$

whose solution is simply

$$v_{mm}(r) = \frac{Z^2 e^2}{2a\epsilon}. \tag{4.125}$$

Finally, the full bare (Coulomb) energy of interaction between fixed charges on the surfaces of a pair of spherical, uniformly surface-charged microgels can be expressed (in k_BT units) as

$$\beta v_{mm}(r) = \begin{cases} \frac{Z^2\lambda_B}{r}, & r \geq 2a \\ \\ \frac{Z^2\lambda_B}{2a}(1 - r/2a) + \frac{Z^2\lambda_B}{2a}, & 0 < r < 2a. \end{cases} \tag{4.126}$$

After adding to Equation (4.113) the bare Coulomb potential between the spherical microgels Equation (4.126), the effective pair interaction is

$$\beta v_{\text{eff}}(r) = \begin{cases} Z_{\text{eff}}^2\lambda_B\frac{e^{-\kappa r}}{r}, & r \geq 2a \\ \\ \frac{Z^2\lambda_B}{2\kappa^2a^2r}\left[1 - e^{-\kappa r} - e^{-2\kappa a}\sinh(\kappa r)\right], & 0 < r < 2a. \end{cases} \tag{4.127}$$

Note that the effective pair potential Equation (4.127) depends on the bulk densities of all microions. Finally, these explicit analytical expressions for the effective pair potential and one-body volume energy of a monodisperse suspension of surface-charged spherical microgels can significantly modify bulk thermodynamic properties, such as osmotic pressure, which is the subject of the next section.

4.4.2. Osmotic Pressure of Monodisperse Suspensions of Charged Sphere Microgels

The bulk osmotic pressure of suspensions surface-charged microgels of equal radii was calculated from Monto Carlo simulations. In the one-component model, the total osmotic pressure can be expressed as

$$\Pi = \Pi_{\text{id}} + \Pi_0 + \Pi_m, \tag{4.128}$$

where the first term on the right-hand side accounts for a microgel ideal-gas pressure, the second term is associated with the microion volume energy, and the last term accounts for the effective interactions and correlations between microgels.

The microgel ideal-gas is simply given by

$$\Pi_{\text{id}} = n_m k_B T. \tag{4.129}$$

The microion volume energy contribution to the osmotic pressure is calculated using the volume energy of Equation (4.116) via

$$\Pi_0 = -\left(\frac{\partial E_0}{\partial V}\right)_{N_s,N_m} \tag{4.130}$$

or (by chain rule)

$$\Pi_0 = -\left(\frac{\partial \kappa}{\partial V}\right)\left(\frac{\partial E_0}{\partial \kappa}\right), \tag{4.131}$$

where the subscripts N_m and N_s denote fixing of all microgel and salt ion numbers, respectively. Finally, the corresponding volume pressure is given by

$$\beta\Pi_0 = -\frac{n_m}{2}\frac{e^{-2\kappa a}Z^2\lambda\left(-1+e^{2\kappa a}-2\kappa a\right)}{4\kappa a^2}. \tag{4.132}$$

The microgel contribution to the total osmotic pressure was calculated from simulations of the one-component model of microgel dispersions via the virial theorem,

$$\Pi_m = \left\langle \frac{\mathcal{V}_{\text{int}}}{3V} \right\rangle - \left\langle \left(\frac{\partial U}{\partial V}\right)_{N_s,N_m} \right\rangle. \tag{4.133}$$

Where $\mathcal{V}_{\text{int}}$ is the internal virial and U is internal potential energy, which can be expressed as a sum over microgel pairs of the effective pair potential v_{eff}:

$$U = \left\langle \sum_{i<j=1}^{N_m} v_{\text{eff}}\left(r_{ij}\right) \right\rangle. \tag{4.134}$$

The angular brackets denote an ensemble average over configurations since the pressure fluctuates during the simulation.

Simulations with periodic boundary conditions require the definition of a certain cut-off radius beyond which the interactions between pairs of particles are neglected. However, this truncation of the potential removes a contribution to the total potential energy and pressure. To remedy this truncation of the potential, one can approximately add the interactions beyond the cut-off radius back into the total energy or pressure by assuming that the radial distribution function, $g(r)$, is equal to one. This implies that beyond the cut-off, the correlations between particles are neglected, and particles are randomly displaced. Then, the tail correction of the energy U_{tail}

can be evaluated analytically by

$$U_{\text{tail}} = \frac{2\pi N^2}{V} \int_{r_c}^{\infty} r^2 u(r) \mathrm{d}r. \tag{4.135}$$

A similar approach can be applied to the tail pressure,

$$\pi_{\text{tail}} = -\frac{2\pi}{3} n_m^2 \int_{r_c}^{\infty} r^3 v'_{\text{eff}}(r) \mathrm{d}r. \tag{4.136}$$

Adding the tail pressure contribution [Equation (4.136)] to Equation (4.133) yields

$$\Pi_m = \left\langle \frac{\mathcal{V}_{\text{int}}}{3V} \right\rangle - \left\langle \left(\frac{\partial U}{\partial V} \right)_{N_s, N_m} \right\rangle + \pi_{\text{tail}}. \tag{4.137}$$

In statistical mechanics, the internal virial term in Equation (4.137) is given by

$$\mathcal{V}_{\text{int}} = \sum_{i=1}^{N_m} \mathbf{r}_i \cdot \mathbf{f}_i = \sum_{i<j=1}^{N_m} r_{ij} \mathrm{f}_{\text{eff}}\left(r_{ij}\right), \tag{4.138}$$

where f_i is the effective force on microgel i due to all other microgels within the cutoff radius r_c, r_{ij} is is the center-center distance between particles i and j, and $\mathbf{f}_{\text{eff}}$ is the effective force exerted on particle i by particle j, expressed as

$$\mathrm{f}_{\text{eff}}\left(r_{ij}\right) = -v'_{\text{eff}}\left(r_{ij}\right). \tag{4.139}$$

Differentiating Equation (4.127) with respect to r to compute the effective force exerted on surface-charged microgel i by microgel j, for the case of nonoverlaping microgels,

$$\mathrm{f}_{\text{eff}}\left(r\right) = (\kappa + \frac{1}{r}) v_{\text{eff}}(r), \quad r > 2a. \tag{4.140}$$

For overlapping microgls, an explicit expression for the effective electrostatic force between overlapping microgls can be obtained by

$$\mathrm{f}_{\text{ov,eff}}(r) = -v'_{\text{ov}}(r) = \mathrm{f}_{mm}(r) + \mathrm{f}_{\text{ind}}(r), \tag{4.141}$$

where $\mathrm{f_{mm}(r)}$ is the bare electrostatic force and $\mathrm{f_{ind}(r)}$ is the microion-induced electrostatic force. Differentiating Equation (4.127) with respect to r (in the case of $r < 2a$), the $\mathrm{f_{ov,eff}(r)}$ for overlaping surface-charged ionic microgel pairs is

$$\beta \mathrm{f_{ov,eff}}(r) = \frac{Z^2 \lambda_B \left[-1 + e^{-\kappa r}(1+\kappa r) + e^{-2\kappa a}(-\kappa r \cosh(\kappa r) + \sinh(\kappa r))\right]}{2a^2 r^2 \kappa^2}. \tag{4.142}$$

Returning to the second term of Equation (4.133), this term is obtained from taking the volume derivative of the partial internal potential energy in Equation (4.134) for a fixed configuration of microgels $\{\mathbf{r}\}$. Since U depends implicitly on the volume through κ, the partial derivative of the internal potential energy in Equation (4.134) can be expressed as

$$\left(\frac{\partial U}{\partial V}\right)_{x_m, x_s, \{\mathbf{r}\}} = \left(\frac{\partial U}{\partial \kappa}\right)_{\{\mathbf{r}\}} \left(\frac{\partial \kappa}{\partial V}\right)_{N_m, N_s}, \tag{4.143}$$

where $x_m = N_m/V$ is the concentration of microgels and $x_s = N_s/V$ is the salt concentration. The quantity $\left(\frac{\partial \kappa}{\partial V}\right)_{N_m, N_s}$ is given by

$$\left(\frac{\partial \kappa}{\partial V}\right)_{N_m, N_s} = -\frac{\kappa}{2V} \tag{4.144}$$

or

$$\left(\frac{\partial \kappa}{\partial n_m}\right) = \frac{\kappa}{2n_m}. \tag{4.145}$$

The quantity $\left(\frac{\partial U}{\partial \kappa}\right)_{\{\mathbf{r}\}}$ can be rewrite as

$$\sum_{i<j=1}^{N_m} \frac{\partial v_{\mathrm{eff}}(r_{ij})}{\partial \kappa} = \frac{2n_m}{\kappa} \sum_{i<j=1}^{N_m} \frac{\partial v_{\mathrm{eff}}(r_{ij})}{\partial n_m}, \tag{4.146}$$

where $\left(\frac{\partial v_{\mathrm{eff}}(r_{ij})}{\partial n_m}\right)$ represents a density derivative of the effective electrostatic pair potential between microgels. For nonoverlapping microgel pairs, the effective Yukawa potential [Equation (4.127)] yields

$$\begin{aligned} \beta n_m \left(\frac{\partial v_{\mathrm{eff}}(r)}{\partial n_m}\right) =& e^{-\kappa r} Z^2 \lambda_B \\ & \times \left(\frac{\cosh(\kappa a)\sinh(\kappa a)}{\kappa a r} - \frac{\sinh(\kappa a)^2}{r\kappa^2 a^2} - \frac{\sinh(\kappa a)^2}{2\kappa a^2}\right). \end{aligned} \tag{4.147}$$

For overlapping microgels (the second regime of Equation (4.127), $r < 2a$), the partial derivative of the effective pair potential [Equation (4.127)] with respect to κ yields

$$\beta n_m \left(\frac{\partial v_{\text{eff}}(r)}{\partial n_m} \right) = - Z\lambda_B \left(\frac{1 - e^{-\kappa r} - e^{-2\kappa a} \sinh(\kappa r)}{2\kappa^2 r a^2} - \frac{e^{-\kappa r} r - e^{-2\kappa a} r \cosh(\kappa r) + 2a e^{-2\kappa a} \sinh(\kappa r)}{4\kappa r a^2} \right). \tag{4.148}$$

Finally, the tail pressure term of Equation (4.137) is obtained by using the nonoverlapping effective pair potential of microgels (the first regime of Equation (4.127), $r > 2a$) in Equation (4.136),

$$\pi_{\text{tail}} = -\frac{2\pi}{3} Z_{\text{eff}} \lambda_B n_m^2 \int_{r_c}^{\infty} r(1 + \kappa r) e^{-\kappa r} \mathrm{d}r, \tag{4.149}$$

which is equal to

$$\pi_{\text{tail}} = \frac{2\pi}{3} Z_{\text{eff}} \lambda_B n_m^2 \frac{r_c e^{-\kappa r_c} \left(3 + 3\kappa r_c + \kappa^2 r_c^2\right)}{\kappa^2}. \tag{4.150}$$

The process for calculating the total osmotic pressure Π begins by taking the effective forces [Equations (4.140) and (4.142)] and the volume energy [Equation (4.116)] of a suspension surface-charged microgels as input to the simulations. More details will be presented in the MC simulation section.

4.4.3. Effective Interactions of Mixtures of Ionic Microgels

By extending our coarse-graining approach formulated previously for monodisperse suspensions of spherical microgels (see section 4.4.1), effective electrostatic interactions of polydisperse suspensions of surface-charged microgels and the one-body volume energy are calculated. The system of interest was described in section (3.4).

For a mixture of ionic microgels, an explicit expression for the microgel Hamiltonian is

$$H_m = \sum_m \sum_{i<j}^{N_m} v_{mm}(r_{ij}) + \sum_{m<n} \sum_{i=1}^{N_m} \sum_{j=1}^{N_n} v_{mn}(r_{ij}), \tag{4.151}$$

where

$$v_{mn}(r_{ij}) = Z_m Z_n e^2 / \epsilon r_{ij} \tag{4.152}$$

is the Coulomb potential energy between a pair of microgels of species m and n. Similarly, the microion Hamiltonian is

$$H_c = \sum_c \sum_{i<j}^{N_c} v_{cc}\left(r_{ij}\right) + \sum_{c<\nu} \sum_{i=1}^{N_c} \sum_{j=1}^{N_\nu} v_{c\nu}\left(r_{ij}\right), \tag{4.153}$$

where the potential energy between a pair of microions of species c and ν is given by

$$v_{c\nu}\left(r_{ij}\right) = z_c z_\nu e^2/\epsilon r_{ij}. \tag{4.154}$$

Finally, the microgel-microion interaction Hamiltonian is given by

$$H_{mc} = \sum_{m,c} \sum_{i=1}^{N_m} \sum_{j=1}^{N_c} v_{mc}\left(r_{ij}\right). \tag{4.155}$$

The microgel-microion pair potential energy $v_{mc}\left(r_{ij}\right)$ of suspension having two microgels with different radii can be expressed as

$$v_{mc}^m(r) = \begin{cases} -\frac{Z_m z e^2}{\epsilon r} & r > a_m \\ \\ -\frac{Z_m z e^2}{\epsilon a_m} & r < a_m \end{cases} \tag{4.156}$$

Fourier transformation of Equation (4.156) yields

$$\hat{v}_{mc}^m(\mathbf{k}) = -\frac{4\pi Z_m z e^2}{\epsilon k^3 a_m} \sin(k a_m) \tag{4.157}$$

Next, substitution of Equation (4.157) into Equation (4.100) gives the Fourier transform of the microgel-induced pair potential

$$\beta \hat{v}_{\text{mm, ind}}\left(k\right) = -\frac{\beta^2 Z_m Z_n}{\left(1+\kappa^2/k^2\right)\epsilon^2 k} \frac{\sin\left(k a_m\right)}{a_m} \frac{\sin\left(k a_n\right)}{a_n}. \tag{4.158}$$

The counterion density profile of microgel species m, $\hat{\rho}_{m,c}(\mathbf{k})$, may be determined from Equations (4.157), (4.90), and (4.94). Substituting Equations (4.94) and (4.157) into Equation (4.90) gives

$$\hat{\rho}_{m,c}(\mathbf{k}) = \frac{\beta n_c}{(1+\kappa^2/k^2)} \frac{4\pi Z_m z e^2}{\epsilon k^3 a_m} \sin(k a_m), \quad k \neq 0. \tag{4.159}$$

Note that this density profile [Equations (4.159)] is around a single microgel. The inverse Fourier transform of this Equation (4.159) yields

$$\rho_{m,c}(\mathbf{r}) = \frac{Z_m z e^2 \beta n_c}{\epsilon \kappa a_m} \frac{e^{-r\kappa}}{r} \sinh(\kappa a_m), \tag{4.160}$$

which gives the real-space counterion density profile of species m, $\rho_{m,c}(\mathbf{r})$. To the reader, these expressions for the counterion density profile around a single microgel might appear similar to the Debye–Hückel expression for the density of electrolyte ions around a macroion [131]. However, our definition of the inverse Debye screening length differs from that what in the Debye–Hückel approximation. In our approach, the inverse Debye screening length κ depends on the average effective counterion density n_c whereas the Debye–Hückel κ depends on the bulk density of electrolyte ions.

The real-space induced electrostatic pair interaction of uniformly surface-charged ionic microgels (in units of $k_B T$) is obtained by substituting Equations (4.157) and (4.94) into (4.100), and then performing an inverse Fourier transform, yielding the expression

$$\beta v_{\mathrm{mn,ind}}(r) = Z_m Z_n \lambda_B \begin{cases} -\frac{1}{r} + Z_{\mathrm{eff},m}\, Z_{\mathrm{eff},n} \frac{\exp^{-\kappa r}}{r}, & r > a_m + a_n \\ \\ -\frac{1}{a_m} + \frac{e^{-\kappa\, a_m} \sinh(\kappa\, r) \sinh(\kappa\, a_n)}{\kappa^2 a_m a_n r}, & r < a_n - a_m \end{cases} \tag{4.161}$$

and in the intermediate range

$$\begin{aligned} \beta v_{\mathrm{mn,ind}}(r) = Z_m Z_n \lambda_B \Bigg(& \frac{2 + \kappa^2 \left(a_m^2 - a_n^2 - 2(a_m + a_n) r + r^2\right)}{4\kappa^2 a_m a_n r} \\ & - \frac{2e^{-\kappa a_m} \cosh(\kappa(a_n - r)) - 2e^{-\kappa(a_n + r)} \sinh(\kappa a_m)}{4\kappa^2 a_m a_n r} \Bigg), \quad a_m - a_n < r < a_m + a_n, \end{aligned} \tag{4.162}$$

where

$$Z_{\text{eff,m}} \equiv Z\frac{\sinh(\kappa a_m)}{\kappa a_m} \tag{4.163}$$

Note that if $a_m = a_n = a$, Equation (4.161) reduces to Equation (4.113) of the system contains only one microgel species. The effective pair potential between microgels of species m and n takes the form

$$v_{\text{eff}}(r) = \begin{cases} v_Y(r), & r > a_m + a_n \\ \\ v_{\text{ov}} + v_{\text{H}}(r), & r < a_m + a_n. \end{cases} \tag{4.164}$$

Substituting Equation (4.161) into Equation (4.99), the effective microgel-microgel pair potential (for $r \geq a_m + a_n$) is obtained as

$$\beta v_{\text{eff}}(r) = Z_{\text{eff,m}} Z_{\text{eff,n}} \lambda_B \frac{e^{-\kappa r}}{r}. \tag{4.165}$$

To derive the effective microgel-microgel pair potential when two microgel species are overlapping, the bare Coulomb potential $v_{mm}(r)$ between two overlapping surface-charged microgels with different size is calculated as follows:

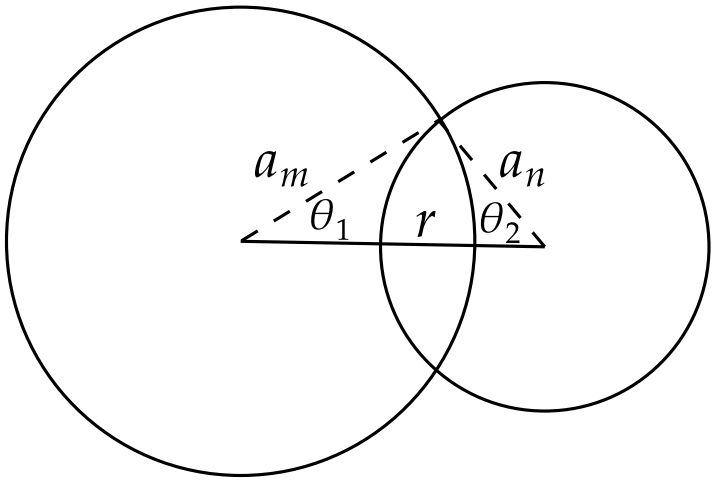

Figure 4.3. An illustration of two overlapping dissimilar spherical surface-charged microgels.

From the geometry of intersection spheres (Figure 4.3), the height of the spherical cap of the left sphere h_L is given by

$$h_L = a_m \times (1 - \cos\theta_1) \tag{4.166}$$

while the height of the spherical cap of the right sphere h_R is given by

$$h_R = a_n \times (1 - \cos\theta_2). \tag{4.167}$$

Using the law of cosines, the $\cos\theta_1$ and $\cos\theta_2$ can be expressed as

$$\cos\theta_1 = \frac{r^2 + a_m^2 - a_n^2}{2a_m r} \tag{4.168}$$

and

$$\cos(\theta_2) = \frac{r^2 + a_n^2 - a_m^2}{2a_n r}. \tag{4.169}$$

Now, the area of the left spherical cap, which is the portion of the surface of one microgel of radius a_m that intersects the second microgel of radius a_n, can be expressed as

$$A_l(r) = 2\pi a_n^2(1 - \cos\theta_2) = \pi a_n^2(1 - \frac{r^2 + a_n^2 - a_m^2}{ra_n}). \tag{4.170}$$

After multiplying by the Coulomb potential of the left microgel and the surface charge density of the right microgel, the interaction energy takes the form

$$v_{mm}(r) = \frac{Z_m Z_n e^2}{2\epsilon a_n^2 a_m} \times A_l(r), \quad r < a_m + a_n. \tag{4.171}$$

Substituting Equation (4.170) into Equation (4.171) yields

$$v_{mm}(r) = \frac{Z_m Z_n e^2}{2a_m \epsilon}\left(1 - \frac{r^2 + a_n^2 - a_m^2}{2ra_n}\right), \quad r < a_m + a_n. \tag{4.172}$$

Equation (4.172) is the electrostatic (Coulomb) energy of interaction between fixed charges on the surfaces of a pair of spherical homogeneously surface-charged microgels of different sizes. By setting $a_m = a_n = a$, the Coulomb interaction between a pair of spherical surface-charged microgels of equal sizes [Equation (4.121)] is recovered.

The contribution of the portion that lies outside the microgel of radius a_m to the bare Coulomb interaction energy between two microgels can be determined from the following approach. Consider two overlapping spheres of different size as, illustrated in Figure 4.4

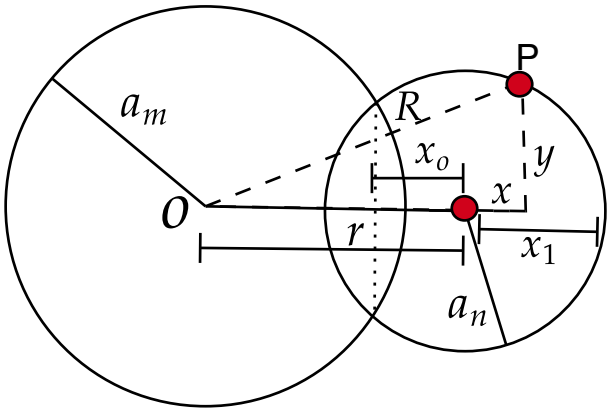

Figure 4.4. A geometric representation of two overlapping dissimilar spherical surface-charged microgels. Their radii are a_m and a_n, and the distance between their centers is r. y is the vertical distance between P and the line joining the centers of the two microgels, x is the horizontal distance between P and the ring of intersection of the two microgel surfaces, $x_0 = \left(\frac{a_n^2 - a_m^2 + r^2}{2r}\right)$, and $x_1 = a_n$.

From Figure 4.4, the area of the portion of the right sphere that lies outside the microgel of radius a_m can be discribed by the integral,

$$A_{out} = \int_{x0}^{x1} 2\pi y ds. \tag{4.173}$$

substituting the element of area ds

$$ds = \frac{a_2}{y} dx \tag{4.174}$$

yields

$$A_{out} = 2\pi a_2 \int_{x0}^{x1} dx. \tag{4.175}$$

The bare Coulomb potential at a point P on the surface of the right microgel of a distance R from the center of the left microgel can be expressed as

$$v_{mm}(r) = \frac{Z_m Z_n e^2}{2a_n \epsilon} \int_{x0}^{x1} \frac{1}{R} dx, \tag{4.176}$$

$$R = \sqrt{(r+x)^2 + y^2} \tag{4.177}$$

and $y = a_n^2 - x^2$. After some substitutions, the above integral can be expressed as

$$\begin{aligned} v_{mm}(r) &= \frac{Z_m Z_n e^2}{2a_n\epsilon} \int_{-\left(\frac{a_{2n}^2 - a_m^2 + r^2}{2r}\right)}^{a_n} \frac{dx}{\sqrt{(r+x)^2 + a^2 - x^2}} \\ &= \frac{Z_m Z_n e^2}{2a_n\epsilon} \frac{1}{r} \left(-a_m + a_n + r\right). \end{aligned} \tag{4.178}$$

Finally, the full bare Coulomb interaction between two spherical surface-charged microgels may be written in the form

$$\beta v_{mm}(r) = Z_m Z_n \lambda_B \begin{cases} \frac{1}{r}, & r > a_m + a_n \\ \frac{1}{2a_m}\left(1 - \frac{r^2 + a_n^2 - a_m^2}{2ra_n}\right) + \frac{1}{2a_n r}\left(-a_m + a_n + r\right), & a_m - a_n < r < a_m + a_n \\ \frac{1}{a_m}, & 0 < r < a_m - a_n. \end{cases} \tag{4.179}$$

Combining Equation (4.179) with Equation (4.161), the effective pair potential may be written in the form

$$\beta v_{\text{eff}}(r) = \begin{cases} \lambda_B\, Z_{\text{eff},m} Z_{\text{eff},n} \frac{e^{-\kappa r}}{r}, & r > a_m + a_n \\ \lambda_B Z_n Z_m \begin{cases} \frac{e^{-\kappa\, a_m} \sinh(\kappa\, r) \sinh(\kappa\, a_n)}{\kappa^2 a_m a_n r}, & r < a_m - a_n \\ \left(\frac{1 - e^{-\kappa r}\cosh(\kappa(a_m - a_n)) - e^{-\kappa(a_m + a_n)}\sinh(\kappa r)}{2a_m a_n \kappa^2 r}\right), & a_m - a_n < r < a_m + a_n. \end{cases} \end{cases} \tag{4.180}$$

The linear response theory also consistently yields an explicit result for the one-body volume energy of a microgel mixture which may be determined from substituting Equations (4.157), (4.158), and

(4.161) into

$$E_0 = F_{\text{OCP}} + \frac{1}{2}\sum_m N_m \lim_{r\to 0} v_{mm,\text{ ind}}\,(r) - \frac{1}{2}\sum_{m,n} N_m N_n \lim_{k\to 0} \hat{v}_{mn,\text{ ind}}\,(k) + \sum_m \sum_c n_m n_c \lim_{k\to 0} \hat{v}_{mc}(k) + \frac{1}{2\epsilon}\sum_m Z_m^2 n_m^2 \lim_{k\to 0} \hat{v}_{cc}(k), \tag{4.181}$$

yielding the expression

$$\beta E_0 = \beta F_{\text{OCP}} - \frac{\lambda_B}{2}\sum_m N_m Z_m^2 \frac{(e^{-2\kappa a_m} - 1 + 2\kappa a_m)}{2a_m^2\kappa} - \frac{1}{2}\frac{\left(\sum_m Z_m N_m\right)^2}{z_c^2 N_c}. \tag{4.182}$$

4.4.4. Osmotic Pressure of Polydisperse Suspensions of Charged Sphere Microgels

Similarly to osmotic pressure of monodisperse suspensions (see section 4.4.2), the osmotic pressure of polydisperse suspensions of surface-charged spherical microgels is obtained. The corresponding volume pressure [Equation (4.130)] is given by

$$\beta\Pi_0 = \lambda_B \left(\frac{-Z_m^2 n_m a_n^2 - Z_n^2 n_n a_m^2 + e^{-2\kappa a_m} a_n^2 n_m Z_m^2 (1 + 2\kappa a_m) + e^{-2\kappa a_n} a_m^2 n_n Z_m^2 (1 + 2\kappa a_n)}{8\kappa^2 a_m^2 a_n^2} \right). \tag{4.183}$$

Differentiating Equation (4.180) with respect to r to compute the effective force exerted on surface-charged microgel i by microgel j yields, for the nonoverlaping microgel pairs case,

$$\mathrm{f}_{\text{eff}}\,(r) = \frac{1 + \kappa r}{r} v_{\text{eff}}(r), \quad r > a_m + a_n \tag{4.184}$$

and for strongly overlapping ($r < a_m - a_n$)

$$\mathrm{f}_{\text{eff}}\,(r) = -\frac{1}{r} + \kappa \coth(\kappa r) v_{\text{eff}}(r), \quad r < a_m - a_n. \tag{4.185}$$

Finally for the intermediate range ($a_m - a_n < r < a_m + a_n$),

$$\beta \mathrm{f}_{\mathrm{eff}}(r) = \frac{Z_m Z_n \lambda_B}{2\kappa^2 a_m a_n} \left(\frac{e^{-\kappa r}\kappa \cosh\left[\kappa(a_m - a_n)\right] - e^{\kappa(-a_m - a_n)}\kappa \cosh(\kappa r)}{r} - \frac{1 - e^{-\kappa r}\cosh\left[\kappa(a_m - a_n)\right] - e^{\kappa(-a_m - a_n)}\sinh(\kappa r)}{r^2} \right), \quad a_m - a_n < r < a_m + a_n. \quad (4.186)$$

By using Equation (4.146), the density derivative of the effective electrostatic pair potential between dissimilar microgels of Equation (4.180) (for $r > a_m + a_n$) is given by

$$\beta n_m \left(\frac{\partial v_{\mathrm{eff}}(r)}{\partial n_m} \right) = \frac{1}{2}\left[-2 - \kappa r + \kappa a_m \coth(\kappa a_m) + \kappa a_n \coth(\kappa a_n) \right], \quad r > a_m + a_n \quad (4.187)$$

and for strongly overlaping ($r < a_m - a_n$),

$$\beta n_m \left(\frac{\partial v_{\mathrm{eff}}(r)}{\partial n_m} \right) = \frac{1}{2}\left[-2 - \kappa a_m + \kappa a_n \coth(\kappa a_n) + \kappa r \coth(\kappa r) \right], \quad r < a_m - a_n. \quad (4.188)$$

Finally for the intermediate range ($a_m - a_n < r < a_m + a_n$),

$$\begin{aligned} \beta n_m \left(\frac{\partial v_{\mathrm{eff}}(r)}{\partial n_m} \right) = \frac{Z_m Z_n \lambda_B}{4\kappa^2 a_m a_n r} \Big(& -2 + e^{-\kappa r}(2 + \kappa r)\cosh\left[\kappa(a_m - a_n)\right] \\ & + e^{-\kappa r}\Big(-\kappa(a_m + a_n)\sinh\left[\kappa(a_m - a_n)\right] \\ & + e^{-\kappa(a_m + a_n - r)}\big(-\kappa r \cosh(\kappa r) + (2 + \kappa(a_m + a_n))\sinh(\kappa r) \big) \Big) \Big). \end{aligned} \quad (4.189)$$

These expressions are taken as input to the MC simulations, from which the total osmotic pressure Π of a suspension of unequally sized, spherical, homogeneously, surface-charged microgels whose fixed charges is described in Equations (4.22) is computed.

5. COMPUTATIONAL METHODS

Computer simulations play a key role in bridging the gap between microscopic length and time scales and the macroscopic world of the laboratory. Computer simulations allow us to understand the properties of assemblies of molecules in terms of their structure and the microscopic interactions between them. Both molecular dynamics (MD) simulations and Monte Carlo (MC) techniques are used in our work and the basics of both simulation techniques with the methods that we developed are discussed in this section.

5.1. Molecular Dynamics Simulations

Molecular dynamics (MD) simulation is a numerical technique that follows the natural time evolution of the trajectories of the particles by integrating Newton's equations of motion in small time steps,

$$\mathbf{F}_i = m_i \frac{d^2\mathbf{r}_i}{dt^2} = -\nabla\, U(\mathbf{r}_{ij}), \tag{5.1}$$

where $i = 1, 2, 3, ...N$ and N is the total number of atoms, $\mathbf{F}_i, \mathbf{r}_i, t, m_i,\ a_i,\ \mathbf{r}_{ij}$, and $U(\mathbf{r}_{ij})$ are, respectively, the force on atom i, the position, time, mass, acceleration, the distance between atoms, and total energy of the system. Equation (5.1) takes into account interactions between particles, external forces acting on them, and the possible constraints imposed on the system. The trajectories of particles are calculated by the velocity Verlet algorithm [132].

In this technique, the configuration of particles is initialized with randomly chosen positions and velocities. Then, the system is evolved in small timesteps. The forces acting on the particles and their new positions and velocities are calculated at every step. The velocities of particles are scaled such that the system has the desired temperature. The average value of a measurable variable A_i, e.g. energy, temperature, and pressure, is now calculated as a time average,

$$\langle A_i \rangle = \frac{1}{M} \sum_{i=1}^{M} A_i, \tag{5.2}$$

where M is the total number of time steps. It has to be ensured that the code runs for a long enough time that the simulation goes through the desired states and reaches the equilibrium state.

LAMMPS [133], a molecular dynamics package, was used to run our simulations of a single ionic microgel (spherical, capsule, and cylindrical) in the cell model. This molecular dynamics package uses the Verlet algorithm to update the trajectories of the particles in each timestep. All simulations ran in the canonical ensemble (fixed N, V, T) in a cubic box, with fixed boundary conditions imposed in all directions only for ionic spherical and capsule microgels. For ionic cylindrical microgels, periodic boundary conditions (PBCs) are imposed in the x-, y-, z-directions. The simulations of spherical and microcapsule microgels were performed in the spherical cell, while those of the cylindrical ionic microgels was performed in a cylindrical cell. Figure 5.1 shows the initial state of the ionic spherical microgel simulation, and Figure 5.2 shows the initial state of the ionic cylindrical microgel simulation.

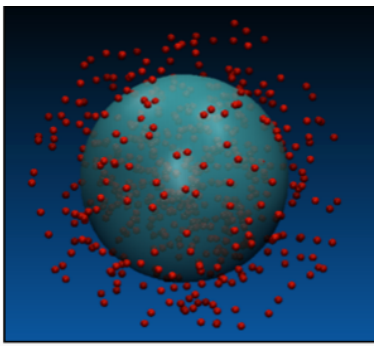

Figure 5.1. Snapshot of MD simulation of ionic spherical microgel and counterions.

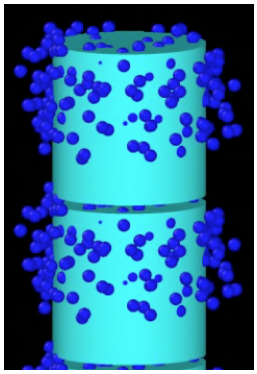

Figure 5.2. Snapshot of MD simulation of ionic cylindrical microgel and counterions.

Before the simulation started, the monovalent microions were initialized on the sites of an FCC lattice. All charged particles interact via bare Coulomb pair potentials, and the influence of the ionic microgel on the microions is modeled by imposing an external electric field. To constrain the particles inside the cell, all particles are repelled from the wall via a Lennard-Jones wall force in all directions for spherical and capsule microgels, whereas a repulsive Lennard-Jones wall force in (x, y) directions is applied for the cylindrical gel system. No Lennard-Jones potential was used between microions, since these were treated as point charges.

During the simulation, the microions are free to move throughout the whole spherical cell, but in the cylindrical cell, the microions can exit and enter the cell only in the z-direction. A direct sum of the Coulombic potential between all pairs of microions is calculated in the simulation of the fixed box. In contrast, in the periodic box, the cylindrical microgel is assumed to be infinitely long to neglect end-effects at the cylinder caps. This approximation can of course only be good if the actual finite cylinders are much longer than they are wide. Thus, a finite cylindrical microgel is replicated in all directions, which results in image charge effects. To calculate corresponding long-range Coulomb interactions, Ewald summation a function built into LAMMPS, is used.

Every 10^8 timesteps out of 10^6 total steps, the LAMMPS software wrote the coordinates of each atom to file. Typically 10^6 steps were used for equilibration. In order to maintain an average constant temperature, LAMMPS rescales the velocities of the particles using the Nosé-Hoover thermostat.

Visual Molecular Dynamics (VMD) and the Open Visualization Tool (OVITO) were used to generate videos and snapshots of the systems. By using OVITO, we made sure that the boundaries of the simulation box are set correctly, and that, in the case of cylindrical microgels, microions can exit and enter the cell only in the z-direction. Finally, after the system reached equilibrium, from the density profile of the counterions, the average number of counterions is computed, which in turn is used to compute the electrostatic component of the osmotic pressure π_e.

In all Poisson-Boltzmann calculations and MD simulations, the following variables were kept fixed:

System parameters: all $\phi_0, R, a_0, b_0, \lambda_B$, and Z, parameters were the same for all calculations and simulations.

Counterions : the total number of counterions was $N_+ = 1000$, each with a charge of $q = 1.0$.

Charge of Microgel : the total charge of the microgel was kept at $q_m = -1000$ to keep the system charge neutral.

Table 5.1 displays the fixed values used in our MD simulations.

Table 5.1. Input parameters for PB calculations and MD simulations.

System Parameter	Value
Particle dry radius a_0	10 nm
Number of microgels N_m	1
Charge valence Z	1000
Linear charge density λ	$100 - 500$
Number of monomers N_{mon}	2×10^5
Number of chains N_{ch}	100
Flory solvency parameter χ	0.5
Monomers radius r_m	1.5 Å
λ_B (water at $T = 293K$)	0.72 nm

5.2. Monte Carlo Simulations

Monte Carlo (MC) simulations [134] were used to compute the thermodynamic and structure properties, such as equilibrium swelling behavior, osmotic pressure, and pair correlation functions of bulk suspensions of ionic microgels. Below a basic description of the Monte Carlo method is discussed.

Consider a suspension whose macrostate is specified by fixed N, V, and T (canonical ensemble). At the microscopic level, there are many different configurations in which the macrostate (N, V, T) can be found. At equilibrium, the probability P_i of finding the system in microstate i at temperature T and energy E_i is proportional to the Boltzmann factor,

$$P_i \propto \exp(-\beta E_i). \tag{5.3}$$

The partition function is then given by

$$\mathcal{Z}(N,V,T) = \sum_i \exp(-\beta E_i). \tag{5.4}$$

An ensemble average of a physical quantity A, with value A_i in microstate i, can be determined by sampling the states,

$$\langle A_M \rangle = \frac{\sum_{i=1}^{M} A_i \exp(-\beta E_i)}{\mathcal{Z}}, \tag{5.5}$$

where M is the total number of microstates. To simulate a system of N particles, e.g., ionic microgels confined in a volume V at a fixed temperature T, only a finite number m of the total number of M microstates is required. Then, the average value of a physical quantity A can be written as

$$\langle A_m \rangle = \frac{\sum_{i=1}^{m} A_i \exp(-\beta E_i)}{\sum_{i=1}^{m} \exp(-\beta E_i)}. \tag{5.6}$$

This sampling procedure is known as the Metropolis sampling method [134]. Note that a sufficiently long sequence of random configurations is necessary to obtain reliable results.

The Monte Carlo algorithm consists of trial moves that are rejected or accepted based on probability distribution associated with the ensemble. For example, the types of trial moves in our work are trial moves of both displacements and changes in size of microgel particles. The acceptance probability for a trial displacement or change in size of the microgel particle is

$$p_{acc} = \min\{e^{-\beta(\Delta E)}, 1\}, \tag{5.7}$$

where ΔE is the total change in energy. The general steps of a basic Monte Carlo algorithm are [134]

1. Make a trial move;
2. Using a probability distribution function, accept or reject the trial move;
3. Update the state of the system;
4. Repeat.

Our Metropolis Monte Carlo simulations which are suited to the coarse-grained one-component model described in section 3.4, were developed within the Open Source Physics Library in Java [135]. The Open Source Physics Library is a free, open source library that contains many different simulations of numerical methods and physical systems written in the Java programming language. The simulation is performed within a cubic cell with periodic boundary conditions (PBCs) so that if a particle passes through one face of the simulation box it re-enters through the opposite face of the box. This means that the particles are able to interact with each other from opposite sides of the simulation box.

The simulation of pseudo-microgels is performed in the constant-NVT (canonical) ensemble at fixed system parameters: λ_B, Z, a_0, N_{mon}, N_{ch}, ν, N_m χ, and B. Table 5.2 displays the fixed values used in our MC simulations.

Table 5.2. Input parameters for ionic microgel suspensions.

System Parameter	Value
Particle dry radius a_0	10 nm
Number of microgels N_m	500
Charge valence Z	1000
Number of monomers N_{mon}	2×10^5
Number of chains N_{ch}	100
Flory solvency parameter χ	0.5
Hertz amplitude B	15000
Poisson's ratio ν	0.5
λ_B (water at $T = 293K$)	0.72 nm

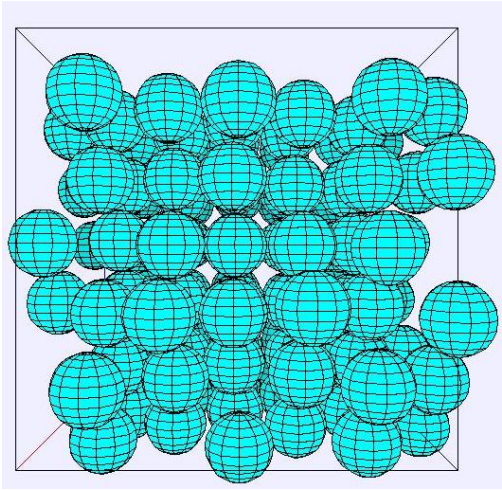

Figure 5.3. Typical snapshot from a MC simulation of a suspension of compressible, ionic, spherical microgels of fluctuating size in a cubic box with periodic boundary conditions in the coarse-grained model.

Figure 5.3 shows a typical snapshot of the system. For each step in a simulation, a trial move consisting of both a displacement and size change (swelling/deswelling) was attempted for one microgel. This was done by a trial changes in the coordinates (x, y, z) and swelling ratio α of each particle with tolerances $\Delta x = \Delta y = \Delta z = 0.1a_0$ and $\Delta a = 0.05$ and then calculating the difference of the total energy ΔE after trial moves and before the trial moves were attempted. The trial moves were rejected if the Boltzmann factor $\left(e^{-\beta \Delta E}\right)$ is less than a random number between $(0, 1)$. If the trial moves were accepted, then the energy of the system was updated and another microgel particle underwent trial moves. The equilibrium state of minimum total free energy is obtained through repeated trial moves. After equilibration stage, the equilibrium structural and thermal properties were collected by averaging over configurations.

5.2.1. Structural Properties

5.2.1.1. Radial Distribution Function

The radial distribution function $g(r)$ was used to determine the equilibrium structure of the surface-charged spherical microgel suspensions. The radial distribution function allowed us to determine the probability distribution of finding a particle in a given position at a radial distance r from the center of a reference sphere. In other words, it describes how the density of surrounding particle varies as a function of the distance from a point. The radial distribution function for each

frame is computed and then averaged:

$$g(r) = \frac{N(r)}{4\pi r^2 \rho \delta r}, \tag{5.8}$$

where $N(r)$ is the number of particles in a spherical shell of thickness δr with center-to-center distance r from a microgel particle at the origin and ρ is the number of particles per unit volume. To calculate $g(r)$, we histogrammed the number of pairs of microgels at the center-to-center distance r within a cut-off radius r_c, which is taken equal to half of the simulation box length.

5.2.1.2. Static Structure Factor

Computing the static structure factor $S(q)$ allowed us to characterize the average order of an ionic microgel suspension. It is well-known that the Fourier transform of the radial distribution function $g(r)$ gives the static structure factor [136, 137]. However, $S(q)$ can be directly computed from the particle coordinates in our MC simulations:

$$S(q) = 1 + \frac{2}{N_{\mathrm{m}}} \sum_{i<j=1}^{N_{\mathrm{m}}} \left\langle \frac{\sin(qr_{ij})}{qr_{ij}} \right\rangle, \tag{5.9}$$

where q is the scattered wave vector magnitude, r_{ij} is the center-to- center distance between particles i and j, and the angular brackets denote an average over configurations.

6. RESULTS AND DISCUSSION

The results that are obtained using the theoretical approaches and both MC and MD methods are presented in this chapter. This chapter contains two major sections. In the first section, swelling behavior and osmotic pressure of single ionic microgels are presented and discussed. Three systems are presented here, namely, microcapsule, cylindrical, and spherical ionic microgels. In the second section, effective pair potentials, swelling behavior, and bulk osmotic pressure of suspensions of ionic microgels are presented and discussed.

6.1. Cell Model Results

In this section, the results obtained using Poisson-Boltzmann theory and molecular dynamics simulation methods in the cell model are presented. After validating our PB theory, by comparing our results with results obtained from MD simulation, we set the stage for analysis of the density profiles, osmotic pressure, and the equilibrium swelling of ionic, microcapsule, cylindrical, and spherical microgels.

6.1.1. Ionic Microcapsules

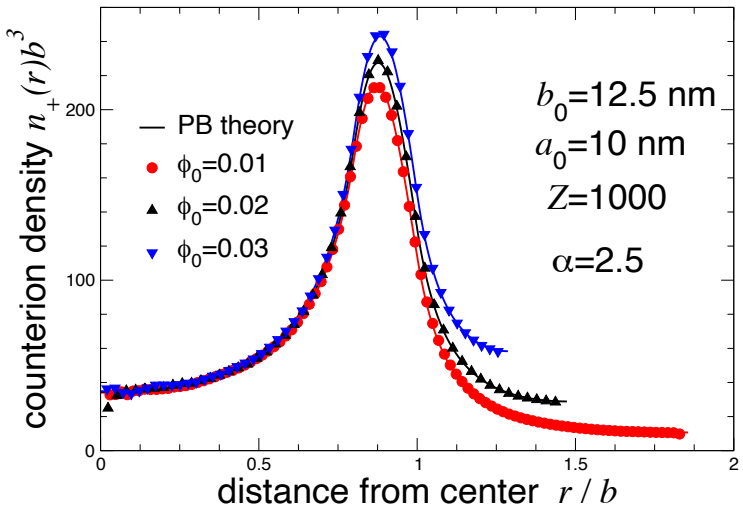

Figure 6.1. Counterion number density profiles around an ionic microcapsule of inner and outer dry radii $a_0 = 10$ nm and $b_0 = 12.5$ nm, respectively, with swollen radii $a = 25$ nm and b= 31.25 nm, and valence number $Z = 1000$ in aqueous solvent from MD simulations (symbols) and PB theory (solid curves) in the cell model at dry volume fractions $\phi_0 = 0.01$, 0.02, 0.03.

Figure 6.1 shows a plot of the counterion radial density profile $n_+(r)$ at different values of the dry volume fraction ϕ_0. The close agreement between simulation and theoretical predictions validates our methods. It can be seen that the heights of the counterion density profiles increase with increasing dry volume fraction. This means that as the dry volume fraction increases, more counterions are attracted to the shell. Because of the charge balance across the microcapsule shell, the distributions of counterions are relatively flat at the cell edge, where the electric field vanishes, while they peak inside the shell region. The slight discrepancy between the MD data and PB predictions at $r/b = 0$ can be attributed to relatively poor statistics at the microcapsule center. Integrating the radial profile over the microcapsule volume gave nearly identical results to the average fraction of interior mobile counterions extracted from the simulations.

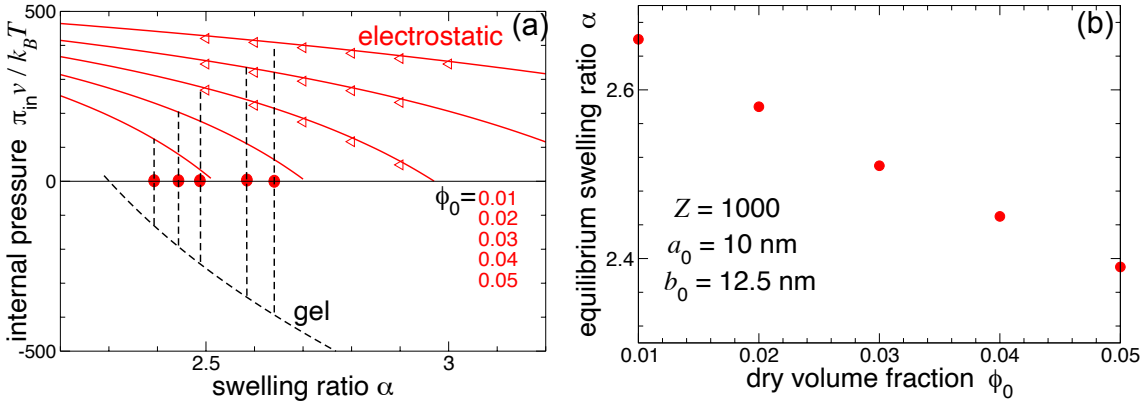

Figure 6.2. Panel (a) shows contributions to the osmotic pressure (electrostatic and gel) inside the ionic microcapsule versus microcapsule swelling ratio for dry microcapsule volume fractions $\phi_0 =$ 0.01-0.05. Electrostatic pressure π_e (Equation 4.18) from Poisson-Boltzmann theory (solid red curves) and from simulations (open red symbols), both in the cell model. Elastic gel pressure π_g (dashed curve) from Flory-Rehner theory. At equilibrium swelling, the total microgel osmotic pressure vanishes: $\pi_e + \pi_g = 0$ (filled symbols). Panel (b) shows equilibrium swelling ratio α vs. dry volume fraction ϕ_0 for same system parameters as in Figure 6.2 (a).

Figure 6.2 (a) shows both the electrostatic component and the gel component of the total microgel osmotic pressure as a function of swelling ratio α, as calculated from both PB theory and MD simulation. By numerically solving the PB equation along with the boundary conditions, as given in section 4.3 in the three radial regions (inside the cavity, in the shell, and outside the capsule), the entire radial density profile $n_\pm(r)$ is computed. After obtained the radial density

profile $n_{\pm}(r)$, the mean numbers of counterions in the shell and second moments of the microion density profiles [Equations (4.20) and (4.21)] are calculated and then used as an input Equation (4.18), from which the electrostatic component of the osmotic pressure π_e is computed. To check our PB numerical calculations, the electrostatic pressure is also computed from MD simulations, which include correlations between microions, using the counterion density profile extracted as histograms. The MD simulation results are nearly identical to those from PB theory, indicating again an agreement between the theoretical prediction and MD simulation. The gel component of the osmotic pressure π_g, as displayed by the black dashed curve in Figure 6.2 (a), is computed from Equation (4.59).

As seen in Figure 6.2 (a), the electrostatic contribution to the osmotic pressure π_e monotonically decreases as the swelling ratio α increases. This may be attributed either to a declining charge density with increasing particle volume, or to a decrease of the self-energy contribution to the pressure [Equation (4.18)] as the size of the microcapsule becomes larger. It can be seen that at low volume fraction, the electrostatic osmotic pressure is higher, as most of the counterions are outside the shell. Starting at $\phi_0 = 0.01$, increasing ϕ_0 leads to a decrease in the electrostatic osmotic pressure. Thus, at sufficiently high concentrations of microcapsules, electrostatic interactions between particles will eventually affect the size distribution. The gel contribution to the osmotic pressure (black dashed curve π_g in Figure 6.2 (a)) monotonically decreases as the swelling ratio α increases. The red dots in Figure 6.2 (a) indicate where the total osmotic pressure vanishes, $\pi_e(\alpha) + \pi_g(\alpha) = 0$. At this point, the system is in an equilibrium state.

Figure 6.2 (b) shows numerical results of the equilibrium swelling ratio α, computed as the root of the equation, $\pi_e(\alpha) + \pi_g(\alpha) = 0$, where $\pi_e(\alpha)$ and $\pi_g(\alpha)$ are obtained from Equations (4.18) and (4.59), respectively. It can be seen that the equilibrium swelling ratio decreases as the dry microcapsule volume fraction increases. This can be explained by the fact that the number of counterions inside the microcapsule decreases as the dry volume fraction increases. As a result, the net charge decreases and causes the microcapsules to deswell.

To perform a more in-depth analysis of the interplay between the equilibrium swelling ratio and the shell thickness, the equilibrium swelling ratio as a function of inner and outer radii of the microcapsule particle is investigated. Figure 6.3 shows the dependence of the equilibrium swelling ratio on microcapsule inner radius a and outer radius b at dry volume fraction $\phi_0 = 0.02$. As the

inner and outer radii grow, the equilibrium swelling ratio of the microcapsule decreases due to there being a decrease in electrostatic pressure, which drives a corresponding reduction in equilibrium particle size.

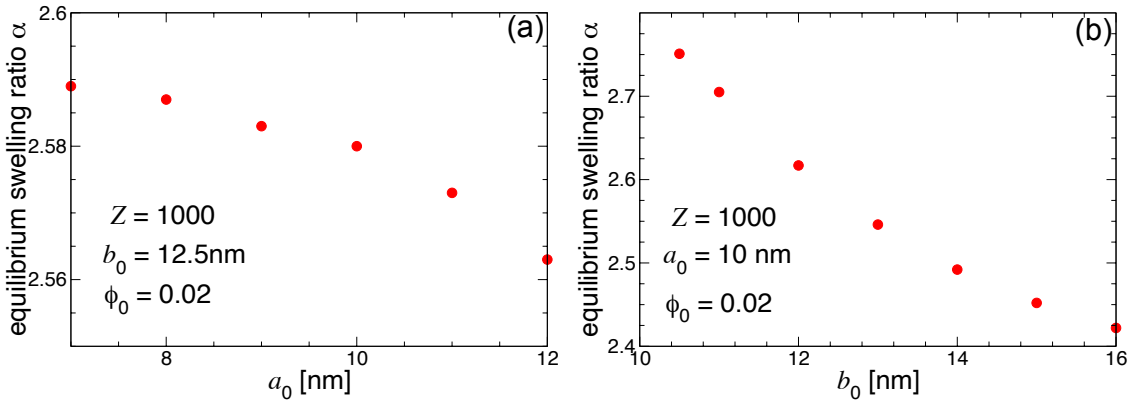

Figure 6.3. Panel (a) displays dependence of equilibrium swelling ratio α on the microcapsule dry inner radius with valence $Z = 1000$ and dry volume fraction $\phi_0 = 0.02$, while panel (b) displays dependence of α on the microcapsule outer dry radius with same parameters as in panel (a).

Figure 6.4 (a) displays the equilibrium swelling ratio as a function of net valence Z_{net} with fixed inner and outer radii. The net valence is defined as the difference in the numbers of counterions inside the shell and outside ($Z_{\text{net}} = N_{\text{in}} - N_{\text{out}}$). As expected, the equilibrium swelling ratio of the microcapsule also increases as the net valence increases. A reason why this equilibrium swelling ratio increases is that the electrostatic component of the osmotic pressure π_e as given in Equation (4.18) increases with the number of counterions Z. Figure 6.4 (b) shows that as the microcapsule dry volume fraction ϕ_0 increases, the net valence decreases. In conclusion, the results shown in Figure 6.4 show that a redistribution of counterions is important in determining the equilibrium swelling/deswelling of ionic microcapsules.

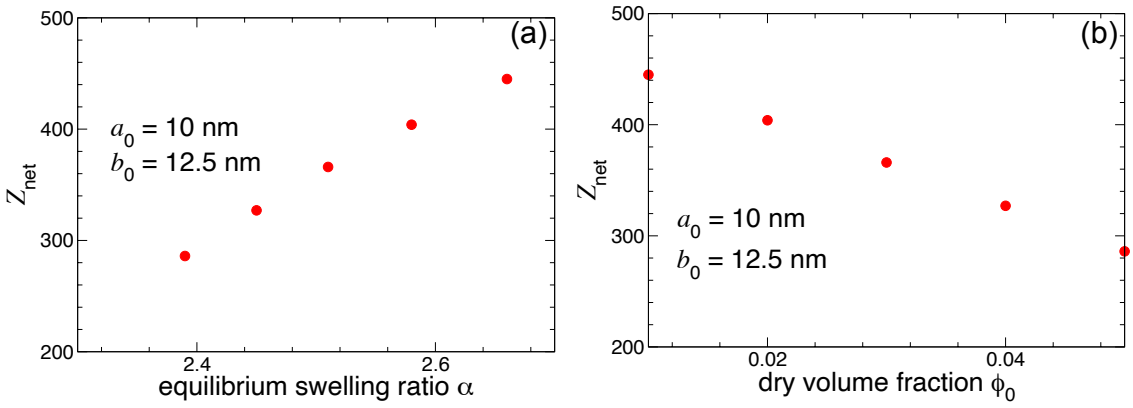

Figure 6.4. Panel (a) displays net valence Z_{net} as a function of equilibrium swelling ratio α with fixed inner and outer dry radii, while panel (b) displays net valence as a function of dry volume fraction with same parameters as in panel (a).

6.1.2. Surface-Charged Microgel

Counterion number density profiles near the fixed charge distributed uniformly over the surface of microgel particle are shown in Figure 6.5, as the results were obtained from PB theory and MD simulations. The data show relatively good agreement between theory and simulation over a range of dry volume fractions. It can be seen that the counterion density has its maximum at $r = a$, where the magnitude of the electrostatic energy of a counterion ψ(r) is maximum, and relatively flat near the microgel center and the cell edge, where the electric field vanishes. Also, the counterion density inside the particle is largely independent of the volume fraction. This is expected, as the environment of the counterions inside the particle remains almost unaffected by a change in the available space outside the particle as the volume fraction changes. At low volume fraction (dilute conditions), the density of counterions inside the microgel is larger than that at the edge of the cell. However, the situation is reversed at high concentrations.

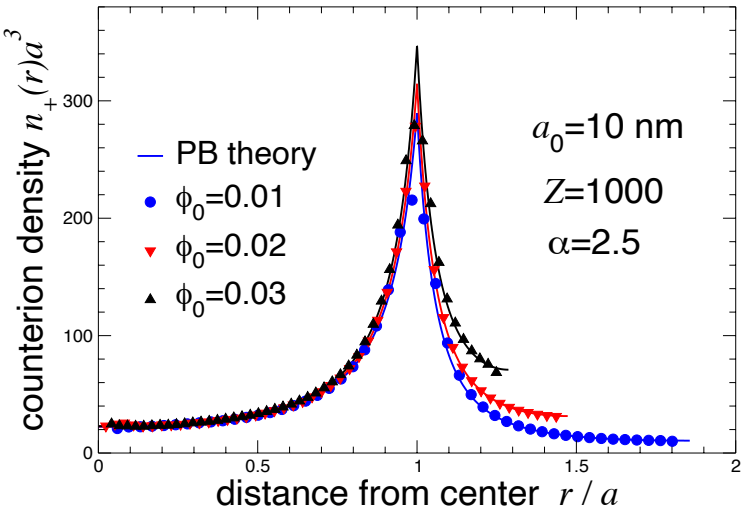

Figure 6.5. Counterion number density profiles around a surface-charged microgel of dry radius a_0 = 10 nm, swollen radius a = 25 nm, and valence Z = 1000 in an aqueous solvent, from MD simulations (symbols) and PB theory (curves) in the cell model at dry volume fractions ϕ_0 = 0.01, 0.02, 0.03.

Following the same procedure as for microcapsule particles (Figure 6.2), both electrostatic (π_e) and gel (π_g) contributions to the osmotic pressure π are shown in Figure 6.6 (a). It is evident from the plot in Figure 6.6 (a) that the theoretical predictions of PB theory and MD simulations agree well. The electrostatic osmotic pressure of the ionic microgel is governed by the self energy of the micorgel and by the number of counterions that are inside the particles. At low swelling ratio, most of the counterions are bound by the charged ions fixed on the particle surface. As a result, the electrostatic osmotic pressure of the microgel is high. However, at higher swelling ratios, more of the counterions are able to escape the attraction and explore the whole volume of the cell, causing the counterion number outside the particle to increase, and resulting in a monotonically decreasing electrostatic contribution to the osmotic pressure. Finally, note that the magnitude of the electrostatic osmotic pressure is greater than in Figure 6.2 (a) for microcapsules.

Similarly to microcapsules, the gel contribution to the osmotic pressure (black dashed curve) π_g monotonically decreases as the swelling ratio increases. The red dots in Figure 6.6 (a) indicate where the equilibrium size of the surface-charged microgel occurs.

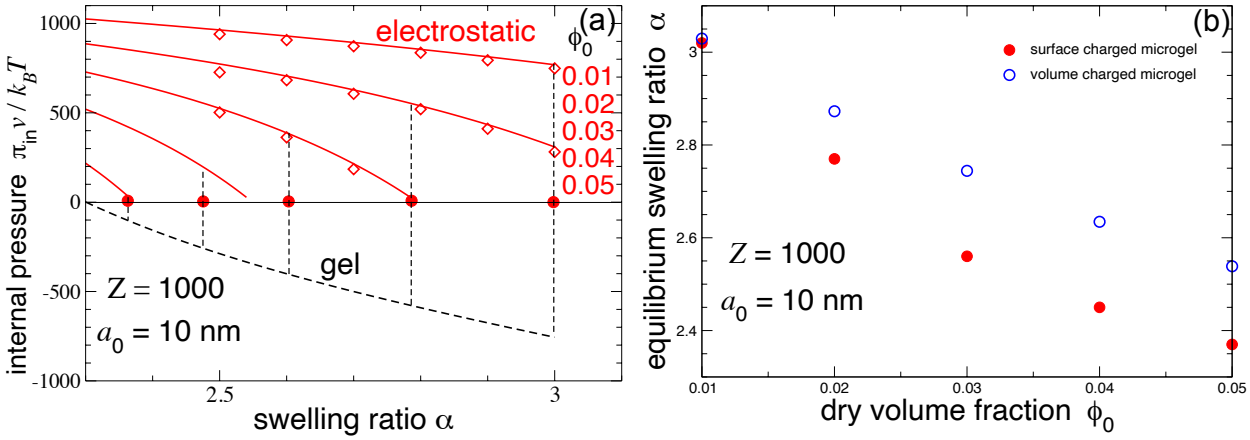

Figure 6.6. Panel (a) shows contributions to osmotic pressure (electrostatic and gel) for a surface-charged microgel versus swelling ratio α for dry charged volume fractions $\phi_0 = 0.01$-0.05. Electrostatic osmotic pressure π_e from Poisson-Boltzmann theory (red curves) and from MD simulations (open red symbols), both in the cell model. Gel pressure π_g (dashed curve) from Flory-Rehner theory. At equilibrium swelling, the total internal osmotic pressure vanishes: $\pi_e + \pi_g = 0$ (filled symbols). Panel (b) displays equilibrium swelling ratio α vs. dry volume fraction ϕ_0 for volume-charged (blue circle) and surface-charged (red circle) microgels.

A comparison between equilibrium the swelling ratio of a volume-charged microgel and a surface-charged microgel is shown in Figure 6.6 (b). It can be seen that the difference in α between volume-charged microgel and surface-charged microgel is significant. This was expected, because the fixed charged distribution of the two systems is different. It is also evident that the surface-charged microgel deswells faster than the volume-charged microgel with increasing concentration. This difference may be attributed to the change in self-energy and to the change in mobile counterion distribution. In conclusion, the comparison shown in Figure 6.6 (b) shows that the fixed charge distribution influences counterion distributions and equilibrium sizes of microgels.

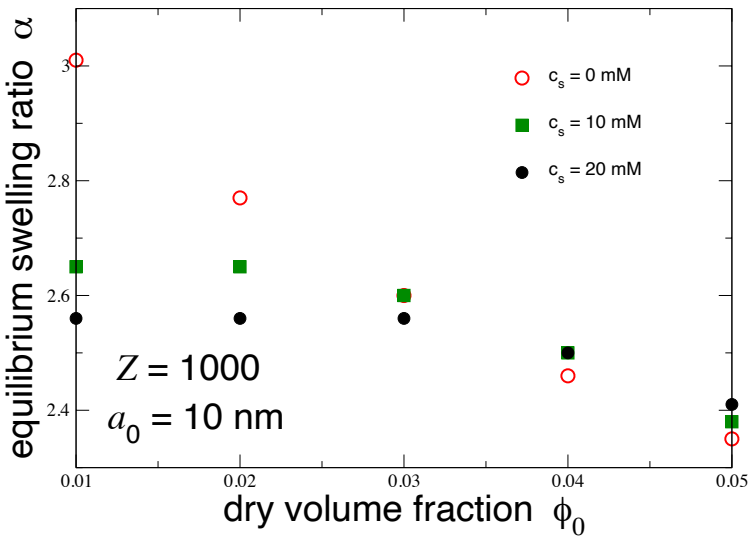

Figure 6.7. Equilibrium swelling ratio α vs. dry volume fraction ϕ_0 for uniform surface-charged microgels of valence $Z = 1000$ and collapsed radius $a_0 = 10$ nm in aqueous solutions with system salt concentrations $c_s = 0$ (red open circles), 10 mM (green squares), and 20 mM (black solid circles).

Figure 6.7 shows the dependence of the equilibrium swelling ratio on both particle and salt concentrations for surface-charged microgels with valence number $Z = 1000$ and dry radius $a_0 = 10$ nm. It can be seen that at zero salt concentration, the microgels swell as the dry volume fraction decreases. With increasing salt concentration, however, the microgels deswell less. This could signify that at higher salt concentrations, there is a reduction in Coulomb electrostatic interaction strength, implying that the gel pressure dominates and deswelling is suppressed.

6.1.3. Cylindrical Ionic Microgels

As mentioned in section 3.3, cylindrical microgels can swell in both axial and radial directions. Therefore, three cases of the swelling of cylindrical gels are considered in this work. The first case is a cylindrical microgel with two ends constrained that swells only in the radial direction. The second case is a cylindrical microgel with a fixed width that swells only in the axial direction. The third case is a free swelling microgel, where no constraint is applied over the cylinder's width and length; the microgel has the freedom to swell in both the axial and radial directions. It is important to keep in mind that the osmotic pressure tensor is anisotropic. The corresponding radial osmotic pressure (electrostatic and gel) can be studied by fixing the axial swelling ratio α_a, and varying only the radial swelling ratio α_r. Conversely, the corresponding axial osmotic pressure can be studied

by fixing the radial swelling ratio α_r, and varying only the axial swelling ratio α_a. However, we infer from the present study that in order to reach our equilibrium conditions, $\pi_{e,r} + \pi_{g,r} = 0$ or $\pi_{e,a} + \pi_{g,a} = 0$ realistic, values of α_a and α_a must be chosen. The radial/axial electrostatic osmotic pressures due to the fixed charges on the microgel and the counterion distribution are obtained from the partial derivative of the free energy with respect to the volume of the microgel (see section 4.1.3), while the radial/axial gel pressures are computed via the Flory-Rehner theory (see section 4.2). It is important to emphasize that our theoretical calculations are well below the threshold for counterion condensation onto polyelectrolyte chains $\lambda_B/l < 1$ (see section 4.3). Finally, to our knowledge, no one has studied the anisotropic swelling of ionic cylindrical microgels. Indeed, systematic studies on control over the osmotic pressure and thermodynamic swelling of ionic cylindrical microgels have not been reported.

Below, the results of each swelling case of surface-charged cylindrical microgels and volume-charged cylindrical microgels are presented.

6.1.3.1. Constrained Swelling

Figure 6.8 shows the theoretical and simulation results for the counterion number density profile $n_+(r)$ for a surface-charged cylindrical microgel at volume fraction $\phi = 0.156$. Similar to a surface-charged spherical microgel, both the theoretical and simulation counterion distributions are relatively flat near the microgel center and cell edge, whereas the distributions peak at the surface of the cylinder. As seen in Figure 6.8, there is excellent agreement between the PB numerical calculations and simulations. This was initially surprising since image charges may affect ion distributions. However, it appears that this effect is less significant in our MD simulations, and PB theory is a fairly good description of weakly correlated cylindrical microgel systems.

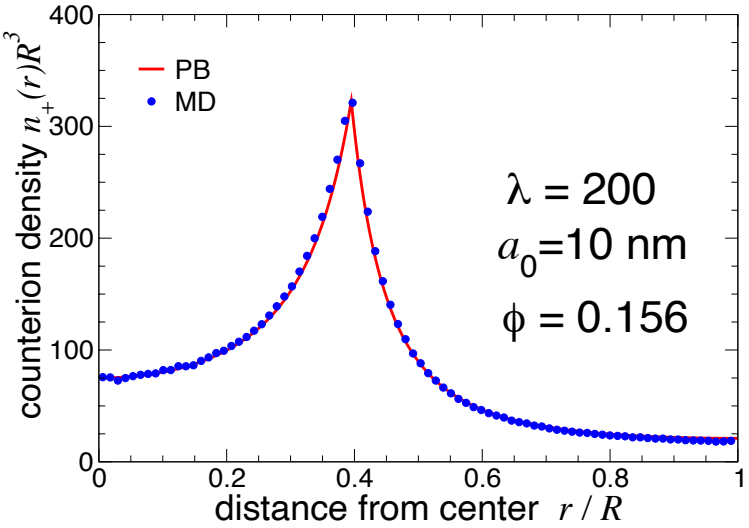

Figure 6.8. Counterion density $n_+(r)$ vs radial distance r from the center of a cylindrical cell (in units of cell radius R) for surface-charged cylindrical microgel.

Figure 6.9 shows computed results for the radial electrostatic osmotic pressure $\pi_{e,r}$ and radial gel osmotic pressure $\pi_{g,r}$ for salt concentrations $c_s = 0.0 - 2$ [mM] and linear charge density $\lambda = 100 - 500$ for surface-charged cylindrical microgels. These results were obtained from our theoretical approach after being validated by MD simulations. As mentioned previously, an optimal value for the axial swelling ratio is required to obtain the equilibrium swelling of the particle; therefore, α_a is fixed at the value of $\alpha_a = 2$. As the counterions are much more mobile than the cylindrical microgel particles, the counterions reach their equilibrium distribution before the microgels. Therefore, the actual charged ions on the microgel surface are assumed to be fixed, and only the reduced linear charge density $\lambda = \frac{Z}{h_0} a_0$ is varied in our PB calculations.

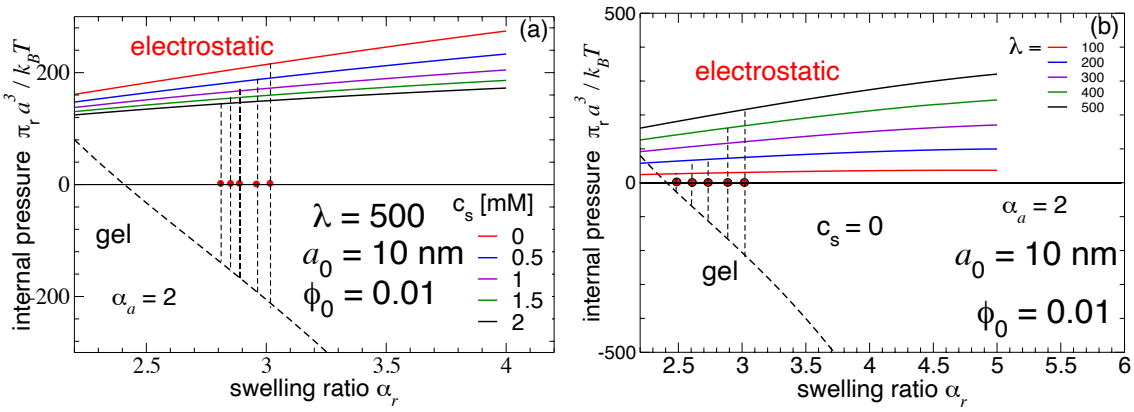

Figure 6.9. (a) Contributions to internal osmotic pressure inside a cylindrical surface-charged microgel vs. radial swelling ratio for salt concentration $c_s = 0.0 - 2$ mM (top to bottom) and linear charge density $\lambda = 500$. (b) Contributions to internal osmotic pressure inside a cylindrical surface-charged microgel vs. radial swelling ratio for linear charge density $\lambda = 100 - 500$ (top to bottom) and $c_s = 0$. Electrostatic pressure $\pi_{e,r}$ from PB theory (solid curves). Radial gel pressure $\pi_{g,r}$ (dashed curve) from the Flory-Rehner theory. At equilibrium swelling, the total internal osmotic pressure vanishes: $\pi_{e,r} + \pi_{g,r} = 0$ (filled symbols).

As seen in both Figures 6.9 (a) and 6.9 (b), the radial osmotic pressure increases gradually as a function of swelling ratio α_r. This is an unusual observation, as in the spherical and microcapsule ionic microgels, the electrostatic osmotic pressure decreases as the swelling ratio α increases (see Figures 6.2 (a) and 6.6 (a)). It was an unexpected result, because the number of counterions inside a spherical or capsule microgel particle increases linearly when the volume fraction of the microgel increases. Therefore, the electrostatic osmotic pressure π_e, which is set by the fraction of counterions that are inside the particle and also by those that are able to escape the attraction, should decrease. The behavior observed in Figures 6.9 can be rationalized as follows. Counterions are more spread out in the case of a cylindrical microgel, therefore, enhancing the self-energy contribution to the radial electrostatic osmotic pressure. As a result, $\pi_{e,a}$ increases.

It is interesting to note that the radial electrostatic pressure curve does ultimately turn down at a very high swelling ratio α_r, where the self-energy term becomes sufficiently weak. Since the present study focused on equilibrium swelling, the present data are only displayed where the equilibrium swelling ($\pi_{e,r} + \pi_{g,r} = 0$) occurs, as represented by the red filled circles in Figures 6.9 (a) and 6.9 (b).

It can be seen that the magnitude of $\pi_{e,r}$ is relatively small at lower α_r, but increases as α_r increases, indicating that salt concentration and charge per unit length λ have less effect at lower swelling ratios than at higher swelling ratios. The salt concentration was included via the Debye screening constant and also in the electrostatic contribution to the radial osmotic pressure [Equation (4.35)]. Since the cylindrical microgels are permeable to microions, salt ions are free to explore the outside and inside region of the microgel. Thus, the presence of salt at a concentration higher than the mean concentration of counterions is expected to reduce the magnitude of electrostatic osmotic pressure. In contrast, the magnitude of $\pi_{e,r}$ increases as the charge of the cylinder increases, as displayed in Figure 6.9 (b). This is likely because there is a significant enhancement in the self-energy with an increase in λ. As a result, the cylindrical gel radius increases.

Adapting the Flory-Rehner theory [Equation (4.59)] (see section 4.2) enables us to compute the radial gel pressure $\pi_{g,r}$. Theoretically, if $\pi_{e,r}$ of our system rapidly increases, then $\pi_{g,r}$ should rapidly decreases since the gel tends to restrain the swelling of the particle. This is shown graphically in Figures 6.9 (a) and (b) by the dashed black lines. If the microgel is not charged, the microgel approaches its equilibrium state when the driving force for the mixing between polymer and solvent molecules is balanced by the elastic restoring force of the chains in the network due to the elasticity of the polymer network. In Figures 6.9 (a) and (b), the equilibrium radial swelling ratio for non-ionic cylindrical microgels would be at $\alpha_r = 2.4$, where the gel pressure is zero.

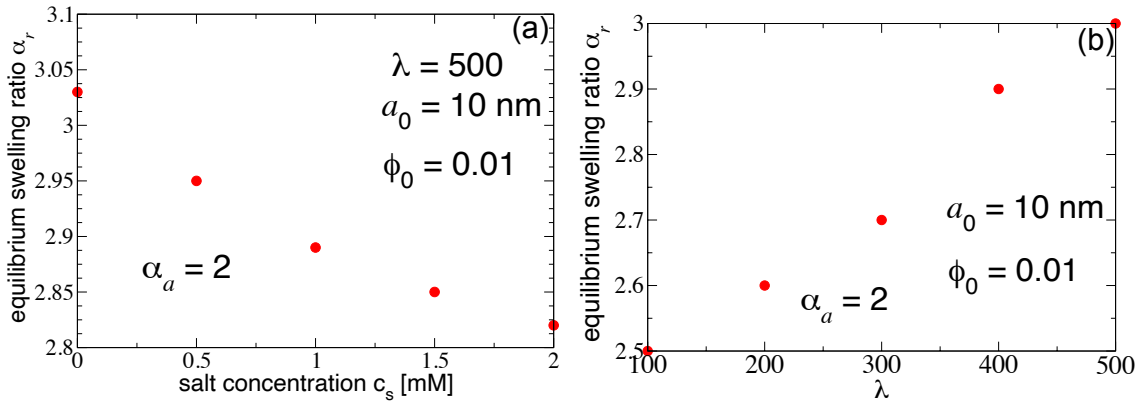

Figure 6.10. (a) Equilibrium radial swelling ratio α_r vs. salt concentration for surface-charged cylindrical microgel computed via nonlinear PB theory. (b) Equilibrium radial swelling ratio α_r vs. linear charge density for surface-charged cylindrical microgel for $c_s = 0$.

The importance of the counterions in our model for equilibrium swelling suggests that the addition of salt ions could have a strong influence. As noted above, the swelling of a microgel is given by the balance of the pressures inside and outside the particle. The equilibrium radial swelling ratio α_r was computed by finding the root of the equation $\pi_{e,r} + \pi_{g,r} = 0$ over ranges of salt concentration and linear charge density as shown in Figure 6.10. As shown in Figure 6.10 (a), the cylinder radius decreases as the salt concentration increases. Our data imply that high salt concentrations might reduce counterion-induced effects. Figure 6.10 (b) shows the dependence of α_r on λ, whose trend can be explained by the self-energy contribution to the electrostatic osmotic pressure and the counterion density.

Figure 6.11 shows the electrostatic and gel contributions to the axial osmotic pressure, $\pi_{e,a}$ and $\pi_{g,a}$, when the radius of the cylinder is fixed, and only the length of the cylindrical microgel varies. It can be seen that over this range of salt concentration ($c_s = 0.0 - 2$ mM) and linear charge density ($\lambda = 100 - 500$), the axial electrostatic osmotic pressure decreases monotonically and roughly linearly. Furthermore, it is shown that the variations of the magnitude of $\pi_{e,a}$ as a function of salt concentration are weaker compared to those for radial swelling [Figure 6.9 (a)]. However, as λ increases, as in Figure 6.11 (b), the magnitude of $\pi_{e,a}$ is very large compared to the corresponding value for radial swelling [Figure 6.9 (b)]. For axial swelling, the axial gel contribution to the total osmotic pressure decreases more gradually than for radial swelling, indicating that the cylindrical microgel tends to deswell less in the axial direction.

The equilibrium axial swelling ratio α_a is shown in Figure 6.12 over a range of salt concentration and charge density. As the salt concentration is increased, the change in α_a is more significant than that in the radial direction. Figure 6.12 (b) shows α_a as a function of linear charge density λ. For similar reasons to those given for Figure 6.10 (a), it was expected that α_a would increase when λ of the cylidrical microgel increases. Finally, Figures 6.10 (b) and 6.12 (b) indicate that the surface-charged cylindrical microgel swells more in the axial direction.

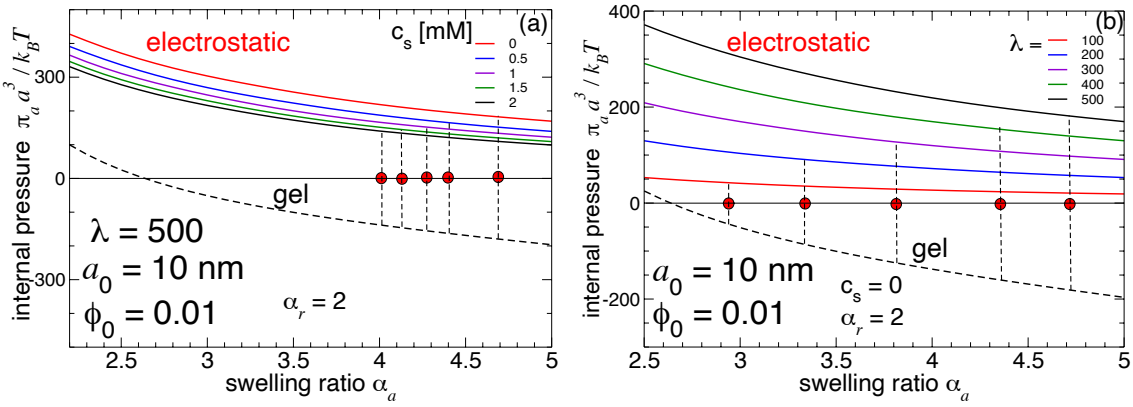

Figure 6.11. Contributions to internal osmotic pressure inside a cylindrical surface-charged microgel vs. axial swelling ratio for (a) linear charge density $\lambda = 500$ and salt concentration $c_s = 0.0 - 2$ mM (top to bottom), and (b) $\lambda = 100 - 500$ (bottom to top) and $c_s = 0$. Electrostatic axial pressure $\pi_{e,a}$ from PB theory (solid curves) and axial gel pressure $\pi_{g,a}$ (dashed curve) from the Flory-Rehner theory. At equilibrium swelling, the total internal osmotic pressure vanishes: $\pi_{e,a} + \pi_{g,a} = 0$ (filled symbols).

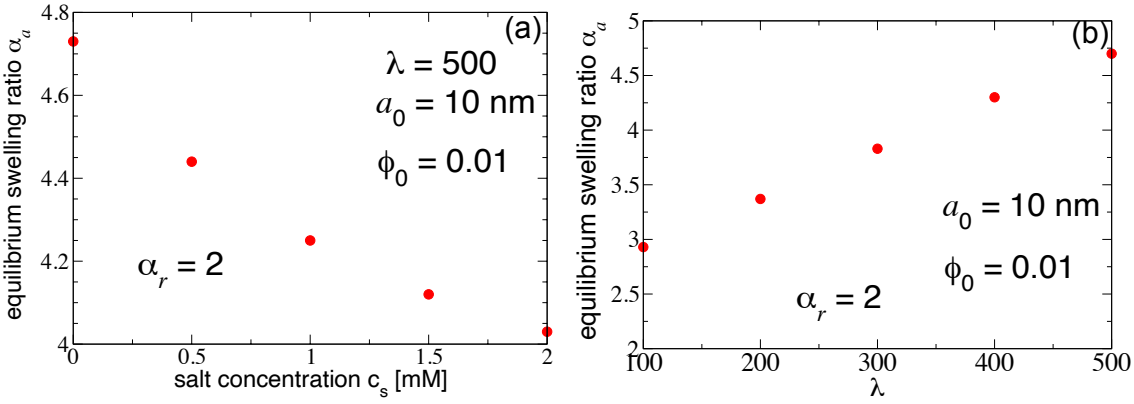

Figure 6.12. Equilibrium axial swelling ratio α_a vs. (a) salt concentration and (b) linear charge density ($c_s = 0$) for a surface-charged cylindrical microgel, computed via nonlinear PB theory.

A typical numerical and simulation result for the radial density distribution of counterions $n_+(r)$ for a volume-charged cylindrical microgel is shown in Figure 6.13. It can be seen that the PB theory has a remarkable agreement to the molecular dynamics simulation data. This close agreement between MD simulation and theory validates the PB approximation. The counterion density profiles are relatively flat near the cylinder center, where the electric field is weak, and fall off toward the edge over a distance comparable to the screening length (see section (4)). The slight deviations near the center of the microgel are likely due to poor statistics. Note that the

counterion density has its maximum at $r = 0$, where the electrostatic force on a counterion is minimal. By integrating the radial density profile, the average number of counterions inside the cylindrical microgel is computed, from which the electrostatic osmotic pressure is calculated.

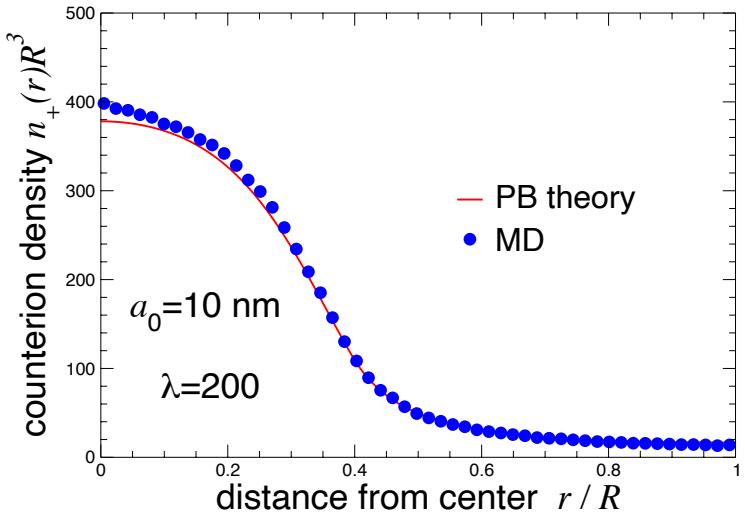

Figure 6.13. Counterion density $n_+(r)$ vs radial distance r from the center of a cylindrical cell for a volume-charged cylindrical microgel of dry radius $a_0 = 10$ nm, reduced valence per unit length $\lambda = 200$, dry volume fraction $\phi_0 = 0.01$, and actual volume fraction $\phi = 0.156$.

Figure 6.14 displays results for the electrostatic and gel contributions to the internal osmotic pressure for volume-charged cylindrical microgels confined in a cylindrical cell over a range of reduced valence per unit length $\lambda = 100 - 500$. Figure 6.14 (a) shows the theoretical results for radial osmotic pressure computed from PB theory. Similar to a surface-charged cylindrical microgel (Figure 6.9 (b)), the electrostatic pressure increases with increasing α_r. The dependence on λ of the magnitude of the electrostatic pressure is relatively small compared to that seen in Figure 6.9 (b). Once again, this difference may be attributed to the modified counterion distribution. Figure 6.14 (b) shows that the axial electrostatic osmotic pressure $\pi_{e,a}$ for volume-charged cylindrical microgels decreases as the axial swelling ratio α_a increases. This decrease in outward (electrostatic) pressure again arises from a redistribution of counterions. The increase in the electrostatic osmotic pressure from $\alpha_a = 1.2$ to 1.6 for $\lambda = 400$ and from $\alpha_a = 1.2$ to 2.1 for $\lambda = 500$ is not surprising since, in general, the electrostatic pressure in principle become negative at sufficiently low swelling ratio. This means that the gel contribution is much larger than the electrostatic contribution for these

chosen system parameters. However, with increasing particle size, the self-energy contribution decreases, and eventually, the electrostatic osmotic pressure drops.

Figure 6.14 shows the gel contribution for the volume-charged cylindrical microgels, which was computed from the Flory-Rehner theory [Equation (4.60)]. In both the radial and the axial direction, the gel pressure becomes negative and monotonically increases in magnitude as the particle swells. This behavior is expected, as the elastic force of the gel tends to restrain the swelling of the particle. The change in gel pressure is lower for radial swelling than for axial swelling, which is clear by comparing the scales of the gel pressures. In terms of our model, suitable values of α_r and α_a should be chosen to fulfill the equilibrium swelling condition, $\pi_e + \pi_g = 0$. Therefore, in the case of radial swelling, the axial swelling ratio is fixed at $\alpha_a = 4$, while in the case of axial swelling, the radial swelling ratio is fixed at $\alpha_r = 4$. Finally, the small red spheres indicate where the sum of electrostatic and gel contributions to the internal osmotic pressure is zero.

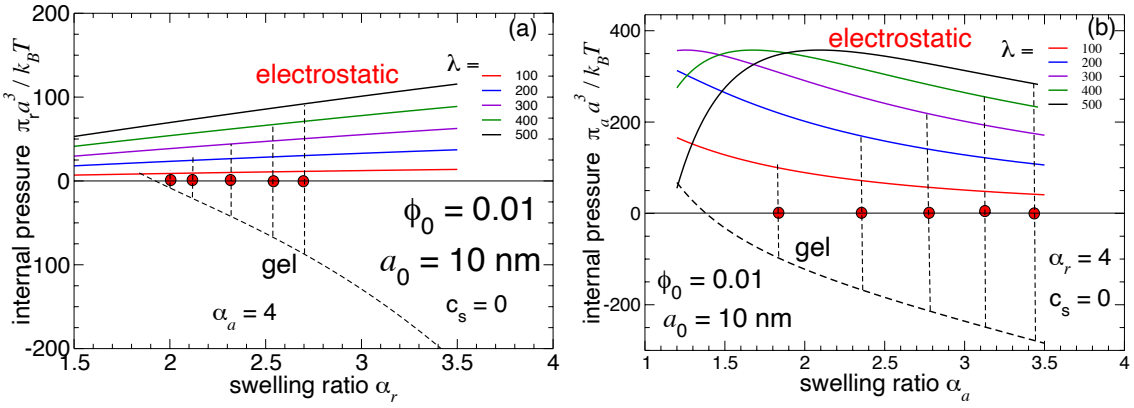

Figure 6.14. Contributions to pressure inside ionic cylindrical microgels vs. the particle swelling ratio for reduced valence per unit length $\lambda = 100 - 500$ (bottom to top). (a) Radial electrostatic pressure $\pi_{e,r}$ from PB theory (solid curves) in the cell model, and radial gel pressure $\pi_{g,r}$ from Flory-Rehner theory (dashed curve). (b) Axial electrostatic pressure $\pi_{e,a}$ from PB theory (solid curves) in the cell model and axial gel pressure $\pi_{g,a}$ from Flory-Rehner theory (dashed curve). At equilibrium swelling, the total radial internal osmotic pressure vanishes, $\pi_{e,r} + \pi_{g,r} = 0$ (filled symbols) and the total axial internal osmotic pressure vanishes, $\pi_{e,a} + \pi_{g,a} = 0$.

The equilibrium radial/axial swelling ratios vs. linear charge density $\lambda = 100 - 500$ for a volume-charged cylindrical microgel are displayed in Figure 6.15. For similar reasons to those given for Figure 6.10 (a), it was expected that equilibrium radial/axial swelling would increase when the valence of the cylidrical microgel increases. For these parameters, the axial equilibrium swelling

ratio α_a rises by more than 10% from $\lambda = 100 - 500$ compared to α_r. This indicates that the cylindrical microgel swells more in the axial direction.

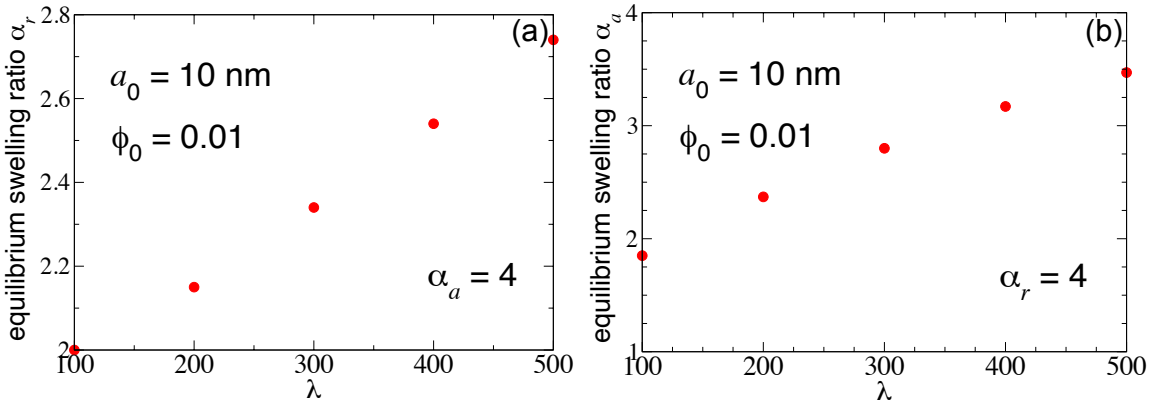

Figure 6.15. Equilibrium radial swelling ratio α_r (a) and equilibrium axial swelling ratio α_a (b) vs. reduced linear charge density for a volume-charged cylindrical microgel computed via nonlinear PB theory.

One possible explanation for why the cylindrical microgel swelling behavior results for the radial swelling differ from the axial swelling is that the volume outside of the microgel for radial swelling decreases as the particle size increases while it remains unchanged in the case of axial swelling, leaving the counterions with less free space between the microgel and the cell's edge in the case radial swelling than in the case of axial swelling, which would affect the distribution of counterions. Although, these free counterions influence the equilibrium swelling of the ionic cylindrical microgel, most counterions are bound to the microgel due to the electrostatic attraction with its fixed charges. However, the equilibrium swelling properties of the cylindrical ionic microgels are less well understood than those of spherical ionic microgels.

6.1.3.2. Free Swelling

Let us now consider the case of free swelling. In this case, the radial osmotic pressure,

$$\pi_r(\alpha_r, \alpha_a) = \pi_{e,r}(\alpha_r, \alpha_a) + \pi_{g,r}(\alpha_r, \alpha_a), \tag{6.1}$$

which is the sum of the radial electrostatic osmotic pressure [Equation (4.35)] and radial gel osmotic pressure [Equation (4.60)], was computed via PB theory and Flory-Rehner theory. Similarly, the

axial osmotic pressure,

$$\pi_a(\alpha_r, \alpha_a) = \pi_{e,a}(\alpha_r, \alpha_a) + \pi_{g,a}(\alpha_r, \alpha_a), \tag{6.2}$$

which is the sum of axial electrostatic osmotic pressure [Equation (4.37)] and axial gel osmotic pressure [Equation (4.61)], was computed via PB and Flory-Rehner theories as well. Note that Equations (6.1) and (6.2) involve functions of both α_r and α_a. In contrast to the constrained swelling, here, both α_r and α_a vary during the PB calculations. These equations generate two curves, one for the radial pressure and another for the axial pressure, as shown in Figure 6.16, which represents the equilibrium free swelling ratios α_r and α_a for a nonionic cylindrical microgel and a surface-charged cylidrical microgel. These results were obtained by computing the roots of $\pi_r(\alpha_r, \alpha_a) + \pi_a(\alpha_r, \alpha_a) = 0$ via the ContourPlot and FindRoot methods, which are built-in functions in Mathematica. The dashed curves represent the root of the axial osmotic pressure $\pi_a(\alpha_r, \alpha_a)$ and the solid green curves represent the root of the radial osmotic pressure $\pi_r(\alpha_r, \alpha_a)$. It is important to note that $\pi_a(\alpha_r, \alpha_a)$ and $\pi_r(\alpha_r, \alpha_a)$ are equal to zero along their respective curves. The intersection of the curves is a unique point where the total osmotic pressure of the system is equal to zero, indicating that the cylindrical microgel is at equilibrium with the surrounding solvent.

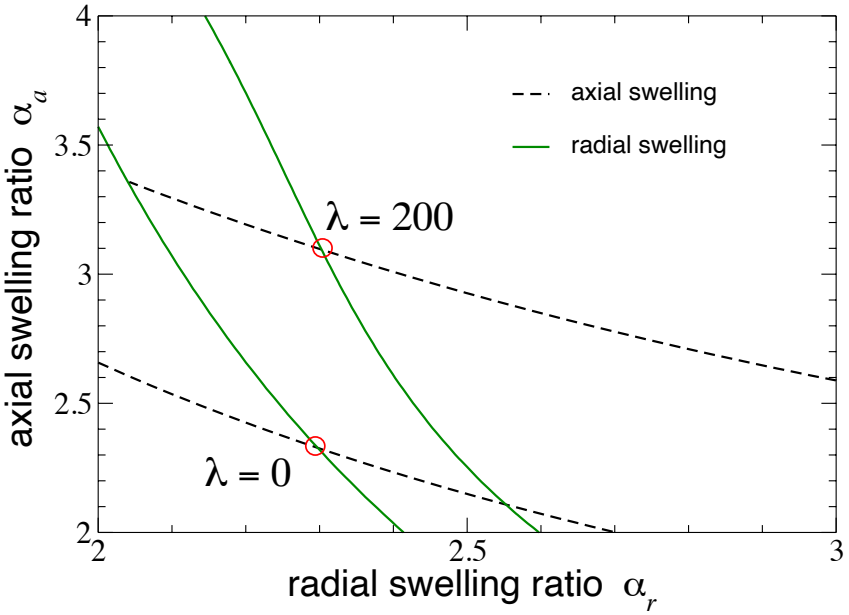

Figure 6.16. Free equilibrium radial swelling ratio α_r vs. axial swelling ratio α_a for cylindrical non-ionic ($\lambda = 0$) and surface-charged ($\lambda = 200$) microgels.

To analyze the swelling properties in the case of free swelling for cylindrical microgels with fixed charges uniformly spread over the particle surface, Figure 6.17 shows the free equilibrium axial swelling ratio α_a vs. the radial swelling ratio α_r over a range of reduced linear charge density $\lambda = 0 - 300$. Upon increasing λ, the equilibrium radial swelling ratio does not increase as much as the equilibrium axial swelling ratio does for all salt concentration c_s. In addition, there is a very slight decrease of α_r as λ increases from 0 to 100. However, it seems that the cylinder tends to swell more in the axial direction than in the radial direction. One possible explanation for this finding is that the axial osmotic pressure $\pi_{e,a}(\alpha_r, \alpha_a)$ is higher than the radial osmotic pressure $\pi_{e,r}(\alpha_r, \alpha_a)$, as shown in Figure 6.17 (b), which is due to the self-energy contribution being higher for axial pressure than radial pressure. Therefore, the cylindrical ionic microgel swells more in the axial direction.

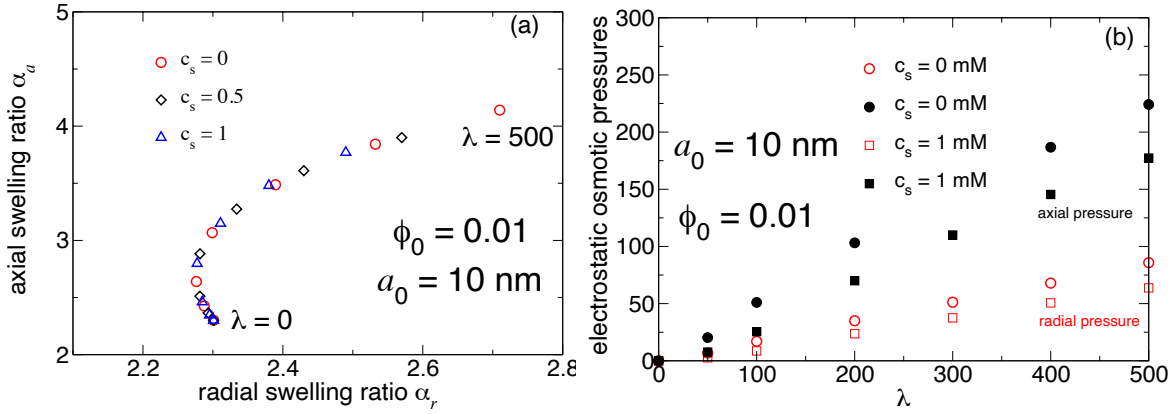

Figure 6.17. (a) Free equilibrium swelling ratios for surface-charged cylindrical microgels over ranges of reduced linear charge density and salt concentration. (b) Radial osmotic pressure $\pi_{e,r}(\alpha_r, \alpha_a)$ and axial osmotic pressure $\pi_{e,a}(\alpha_r, \alpha_a)$ vs. λ for two salt concentrations.

For a volume-charged cylindrical microgel, the data in Figure 6.18 (a) show that with increasing λ, the equilibrium radial swelling ratio increases very slowly compared to the equilibrium axial swelling ratio. As the reduced linear charge density increases beyond $\lambda = 200$, however, α_r increases much more than α_a. To understand this behavior, let's look at the electrostatic pressure as a function of charge density, which is shown in Figure 6.18 (b). Initially, $\pi_{e,a}(\alpha_r, \alpha_a)$ increases up to $\lambda = 200$ and then decreases, while $\pi_{e,r}(\alpha_r, \alpha_a)$ increases monotonically as λ increases. We tried to explore the free swelling behavior for a higher value of λ, but did not succeed, because the

nonlinear Poisson-Boltzmann equation becomes so numerically stiff that our computational method fails to converge to a solution. However, the results of Figure 6.18 suggest that the cylindrical gel tends to swell more in the axial direction than in the radial direction.

Figure 6.19 displays the volume swelling ratio V/V_0 as a function of λ for cylindrical surface-charged and volume-charged microgels. In the surface-charged case, the microgel volume swelling ratio increases as the charge density increases, while in the volume-charged case, V/V_0 increases up to $\lambda = 250$, then decreases. Once again, this difference can be attributed to the differing distributions of counterions inside and outside the particle for the different fixed charge distributions, which would affect the electrostatic osmotic pressures. Finally, due to the PB equation's failing to converge to a solution, we cannot explore the influence of salt on the swelling of volume-charged cylindrical microgels.

In summary, the results from the PB computational method seem to suggest that the distribution of counterions has a significant influence on the swelling/deswelling of ionic cylindrical microgels. In this dissertation, our purpose is to test the accuracy of the theory against MD simulations, and to demonstrate the ability of our theory to explain and interpret observations of particle swelling. Moreover, we showed the sensitivity of swelling to variations in salt concentration. Overall, however, there are still many simulations, numerical calculations, and analyses that need to be completed in order to fully understand the swelling of cylindrical ionic microgels.

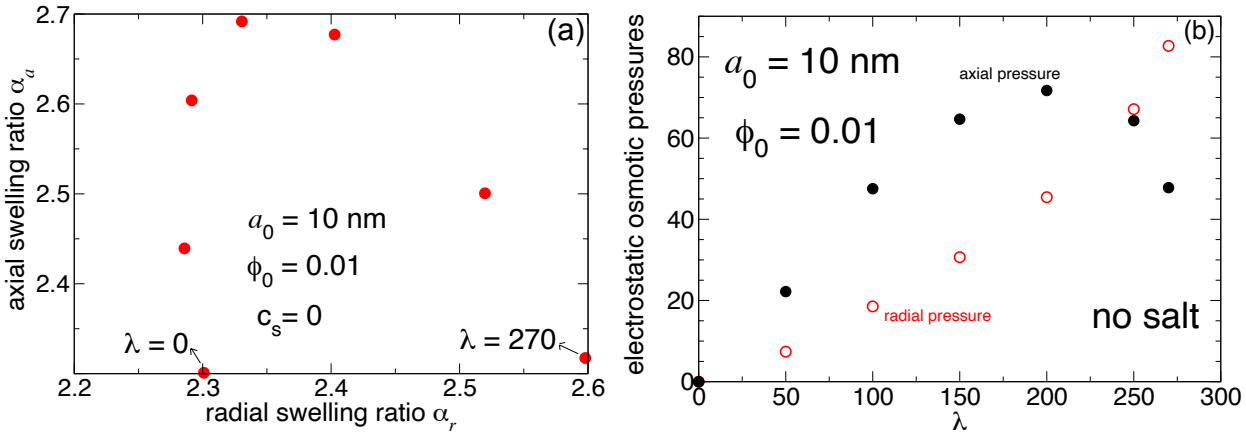

Figure 6.18. (a) Equilibrium radial swelling ratio α_r vs equilibrium axial swelling ratio α_a and (b) equilibrium swelling ratios, α_r and α_a, as functions of λ for volume-charged cylindrical microgels with dry volume fraction $\phi_0 = 0.01$ and dry radius $a_0 = 10$ nm.

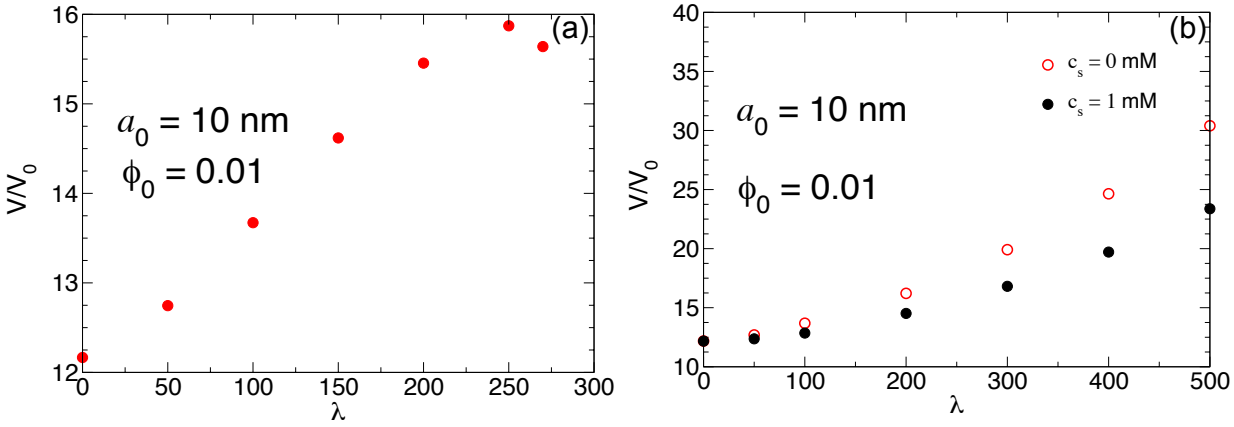

Figure 6.19. Volume swelling ratio V/V_0 as a function of λ for (a) volume-charged and (b) surface-charged cylindrical microgels for dry volume fraction $\phi_0 = 0.01$ and dry radius $a_0 = 10$ nm.

6.2. One-Component Model Results

6.2.1. Monodisperse Suspension of Ionic Microgels

Figure 6.20 shows results for the bulk osmotic pressure of suspensions of spherical surface-charged microgels of the same dry size. The data represented by red circles were computed from MC simulation within the one-component model framework (see section 4.4.2), and the data represented by black squares were computed from PB theory within the cell model framework (see Equation (3.8)). At low concentrations, we find excellent agreement between the MC data and the PB predictions as expected, since the PB theory is known to give a fairly good description of dilute suspensions of weakly charged particles. As the particle concentration increases, however, ion correlations, which are neglected within the PB theory, start to manifest and deviations between MC and PBMC emerge.

Around $\phi_0 = 0.08$, a dip in the MC data is seen due to deformations of the particle. With increasing the particle density (volume fraction ϕ) of a suspension of microgels, the distance between particles decreases and, eventually, above the close packing of hard spheres ($\phi \cong 0.74$), the microgels deform or interpenetrate to accommodate the increase in volume fraction. Microgels can deform by forming facets at the contact area (see Figure 6.21) or can deswell by expelling solvent. As a result, the microgels uniformly deswell, and the available volume decreases.

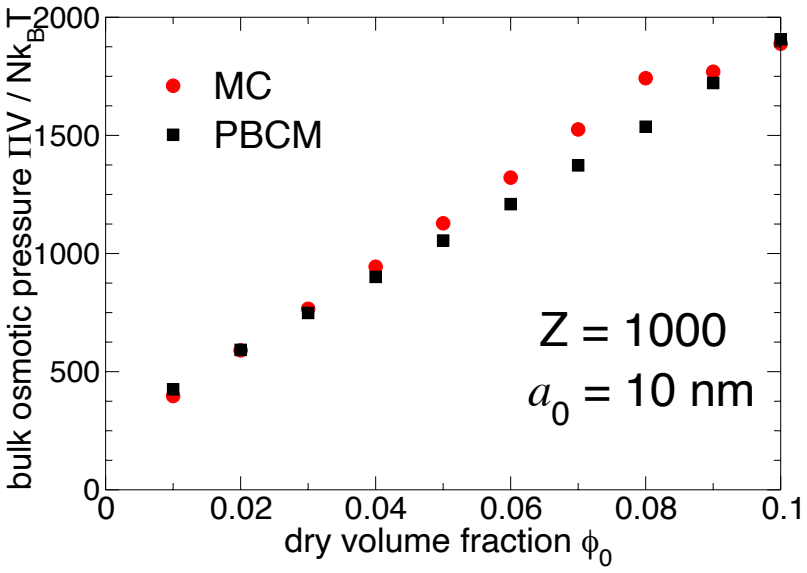

Figure 6.20. Bulk osmotic pressure vs. dry volume fraction ϕ_0 of deionized suspensions of spherical surface-charged microgels. MC simulation data (red circles) are compared with predictions of Poisson–Boltzmann cell model calculations (black squares).

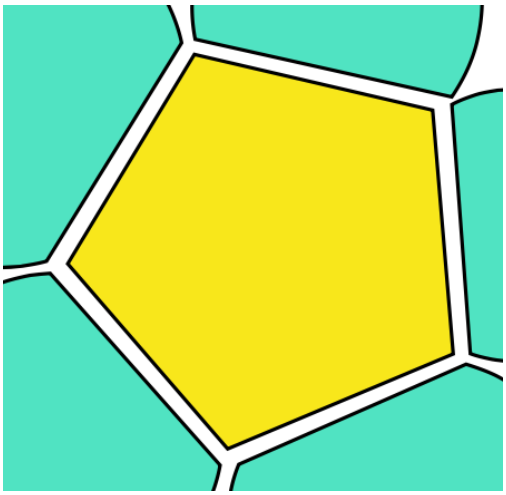

Figure 6.21. Particle deformation in the form of contact facets.

Figure 6.22 (a) displays the variation of actual volume fraction with dry volume fraction obtained from our MC simulations. As the dry volume fraction increases, the actual volume fraction increases until microgels start to deform and shrink to fit into the available space, which occurs at

about $\phi_0 = 0.08$. At this contact point, the effect of elastic (Hertz) interactions become significant, and may imply a shift in microgel response from deswelling to faceting as the microgels get squeezed together, as illustrated in Figure 6.21. This sensitive dependence of microgel size and shape on particle concentration results from a complex interplay between single-particle free energy and effective electrostatic and elastic interactions.

Figure 6.22 (b) shows the cell model result for the swelling ratio of ionic microgels compared with the Monto Carlo simulation result over a range of particle concentrations. The average equilibrium a increases with decreasing ϕ_0. The good agreement between our simulation and the nonlinear PB theory implementation of the cell model provides an important validation of the osmotic pressure theorem, described in section 4. The small deviations at the lowest and highest density can be attributed to differences between the cell model and the one-component model and weak nonlinear screening effects.

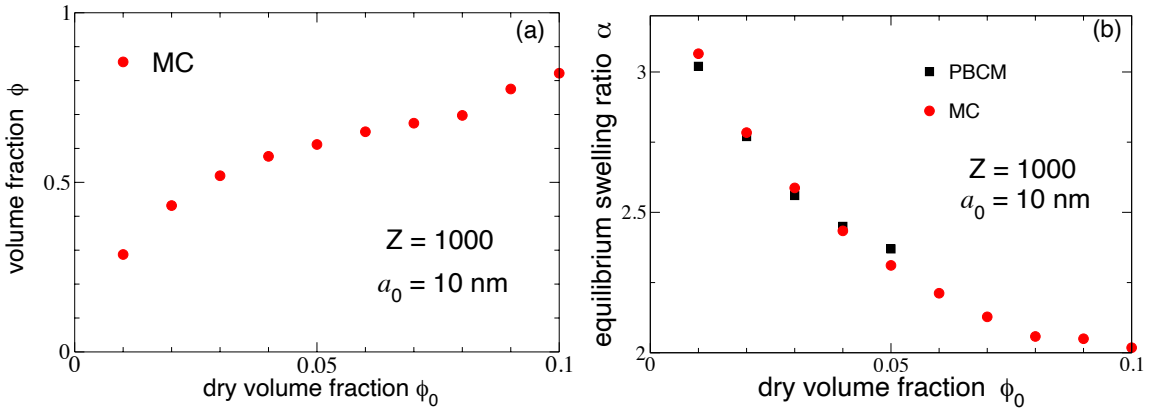

Figure 6.22. MC simulation data for (a) equilibrium volume fraction ϕ and (b) equilibrium swelling ratio α vs. dry volume fraction ϕ_0 in deionized suspensions of spherical surface-charged microgels.

Figure 6.23 (a) shows four radial distribution functions that we obtained from our MC simulations when the valence was fixed at $Z = 1000$ and the number of microgels was $N_m = 108$ for a series of dry volume fractions ($\phi_0 = 0.002, 0.004, 0.01, \text{and } 0.02$). Figure 6.23 (b) shows the corresponding static structure factors. At lower particle concentrations, the structure is still in an FCC crystal phase, as reflected by relatively strong oscillations in $g(r)$ and $S(q)$. In this case, the spherical microgels are not significantly compressed. At higher particle concentrations, the

strucure is also in a solid phase with crystalline order, as signaled by distinct peaks in $g(r)$ and $S(q)$, indicating that the system its retained FCC structure. In this state, microgels are tightly confined and compressed by their microgel neighbors. As seen in Figure 6.23 (b), the main peak grows steadily in height and becomes more distinct with increasing concentration, reflecting strengthening correlations between microgels.

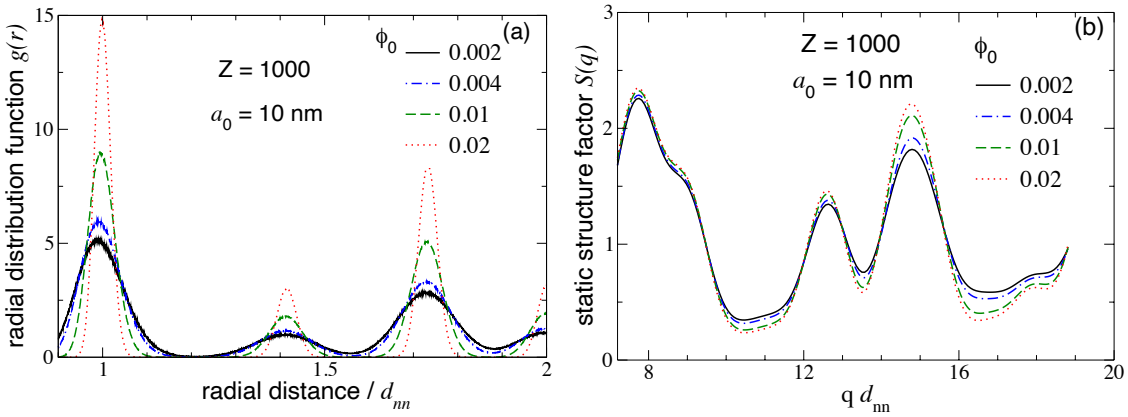

Figure 6.23. (a) Radial distribution function $g(r)$ vs. radial distance r, in units of nearest-neighbor distance d_{nn} in FCC lattice, in suspensions of ionic, compressible microgels. Results are shown for dry volume fraction $\phi_0 = 0.002$-0.02. These systems are all in an FCC crystal phase, as revealed by the positions of the peaks. (b) Static structure factor $S(q)$ vs. scattered wave vector magnitude q, in units of inverse nearest-neighbor distance in FCC lattice. Results are shown for dry volume fractions corresponding to radial distribution functions in Figure 6.23 (a). These suspensions are all in an FCC crystal phase, as reflected by the height of the main peak of $S(q)$

Observing a crystal phase for such low concentations might be due to finite size effects, since our system contains only $N_m = 108$ particles. Therefore, we increased the number of particles to $N_m = 500$ to ensure that $\kappa r_c \gg 1$, such that finite-size effects are negligible. Here r_c is equal to half the box length. Interestingly, our results suggest that the suspensions of surface-charged microgels with dry volume fractions $\phi_0 = 0.002$, 0.003 are in a stable ordered crystal phase as revealed by the positions of the peaks in Figures 6.24, indicating that the electrostatic repulsive interactions are strong even at such low volume fractions. Note that our simulation method cannot distinguish between stable and metastable solid states. As seen in Figure 6.25, the systems with dry volume fractions $\phi_0 = 0.01$, 0.02, and 0.03 are all in a solid phase with crystalline order, and as ϕ_0 increases, the peaks of $g(r)$ and $S(q)$ grow taller and more distinct, reflecting strengthening

correlations between surface-charged microgels. Finally, our results confirm that the finite-size effects are very small.

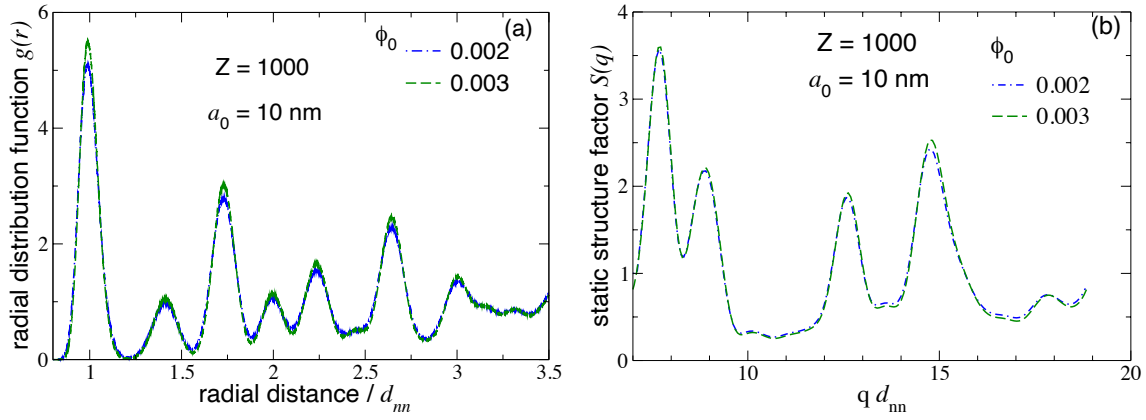

Figure 6.24. (a) Radial distribution function $g(r)$ in units of nearest-neighbor distance d_{nn} for suspensions of surface-charged microgels for dry volume fractions $\phi_0 = 0.002$ (dashed blue curve) and 0.003 (dashed green curve) with system parameters $Z = 1000$, $a_0 = 10$ nm, and $N_m = 500$. (b) Static structure factor $S(q)$ vs. scattered wave vector magnitude q, in units of inverse nearest-neighbor distance d_{nn} in FCC lattice, corresponding to radial distribution functions in Figure 6.24 (a).

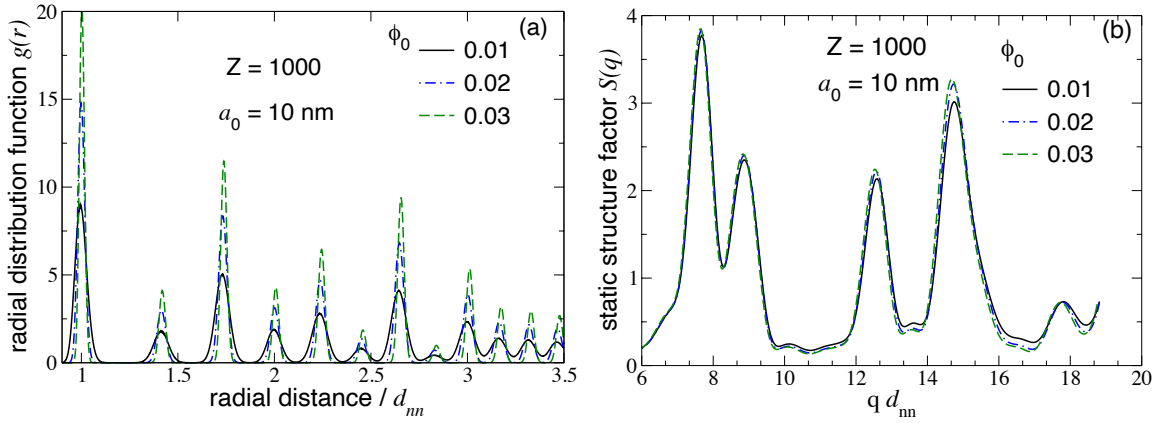

Figure 6.25. Same as Figure 6.24, but for dry volume fractions $\phi_0 = 0.01$ (solid black curve), 0.02 (dashed blue curve), and 0.03 (dashed green curve).

7. SUMMARY AND OUTLOOK

7.1. Summary

Microgels are cross-linked microgel particles in the nanometer to micrometer size range with a capacity to drastically change their size in response to changes in the external environment. Microgels have an ability to store substances such as molecular drugs, and release them upon stimulation, making them potential candidates as drug delivery carries and functional biomaterials.

Using the Poisson-Boltzmann theory of ionic solutions, the Flory-Rehner theory of cross-linked polymer gels, and molecular dynamic simulation techniques, we investigated the swelling behavior of a *single* charged microgel and the connection between counterion distribution and internal osmotic pressure for ionic microgels of various shapes and charge distributions. The Poisson-Boltzmann theory was implemented within a cell model to facilitate numerical solution, allowing us to isolate the electrostatic features of a single ionic microgel. The Poisson-Boltzmann approach was validated by performing MD simulations via LAMMPS. The Flory-Rehner theory was used to compute the gel contribution to the osmotic pressure.

Next, we developed a Monte Carlo simulation algorithm for a coarse-grained model of ionic microgel *suspensions*. Starting from the one-component model and linear response approximation, we derived explicit expressions for (1) an effective electrostatic pair interaction potential between pseudo-microgels and (2) an associated one-body volume energy that contributes to the total free energy. By inputting the effective interactions into MC simulations of the one-component model, we computed thermodynamic and structural properties, including the equilibrium swelling ratio, bulk osmotic pressure, the radial distribution function, and the static structure factor of ionic microgel suspensions.

7.2. Conclusions

In general, ionic microgels swell increasingly in size as the fixed charge on the microgels increases. This behavior can be understood based on the counterion distribution and the electrostatic osmotic pressure. As the valence increases, the self-energy contribution to the electrostatic pressure is strongly enhanced. In contrast, microgels deswell with increasing concentration of salt ions. Increasing the ionic strength of the solvent, induces screening of the microgel charge. Inter-

estingly, the microgel's shape affects the equilibrium swelling ratio; for example, spherical microgel particles were found to swell less than microcapsule particles. In cylindrical geometry, the internal osmotic pressure in the free swelling case showed that charged cylindrical microgels swell more in the axial direction than in the radial direction.

Results from molecular dynamics simulations were compared with PB theoretical predictions and found to be in quantitative agreement. The agreement between simulation and theory confirms that the PB theory is able to describe the equilibrium swelling of ionic microgels in the range of investigated volume fractions. Results also indicate that ionic microgels deswell with increasing volume fraction. As expected, the fixed charge distribution affects the electrostatic osmotic pressure and equilibrium swelling of ionic microgels. When considering a microgel with a charged surface, the electrostatic osmotic pressure is lower and the microgel deswells more compared to a microgel with a volume charge. As shown, the general swelling behavior of ionic microgels can be understood based on the distribution of counterions and osmotic pressure influences.

In the case of a suspension of surface-charged ionic microgels, the results for the equlibrium swelling ratio and bulk osmotic pressure computed from our Monto Carlo simulations of the linearized one-component model quantitively matched theoretical predictions of the nonlinear PB cell model over a considerable range of particle concentrations. With increasing concentration, the surface-charged microgels uniformly deswell, while the actual volume fraction increase monotonically until neighboring microgels start to touch each other.

7.3. Future Work

Although the theoretical models and simulation methods developed here give a better understanding of the swelling behavior of ionic microgels, there is significant room for improvement. A first step toward further developing the model would be to account for the counterion correlations and the effect of multivalent counterions and solvent. Also, one of the major assumptions made in the theoretical model developed here is that all monomers making up a microgel are implicit. This assumption could be avoided by running MD simulations using a more explicit bead-spring polymer model. MD simulations could also be used to probe the dynamical properties of ionic microgels under similar conditions, something the methods used in this study cannot do. The models used in this study can be modified in order to explore the swelling behavior of ionic microgels as a function of pH. The models could also be used to investigate the swelling, ion distributions, and osmotic

pressure of ionic hollow cylindrical microgels or microcapsules with a loaded nano-drug. So far, no experimental study has been reported for investigating the swelling and osmotic pressure of ionic cylindrical microgels. Therefore, one of the major areas of future research would be synthesizing and characterizing swelling and osmotic pressure of ionic cylindrical microgels.

REFERENCES

[1] R H Pelton and P Chibante. Preparation of aqueous latices with n-isopropylacrylamide. *Colloids and Surfaces*, 20(3):247–256, 1986.

[2] Alberto Fernandez-Nieves, Hans Wyss, Johan Mattsson, and David A Weitz. *Microgel Suspensions: Fundamentals and Applications*. John Wiley & Sons, 2011.

[3] W O Baker. Microgel, A New Macromolecule. *Industrial & Engineering Chemistry*, 41(3):511–520, 1949.

[4] A Fernández-Nieves, A Fernández-Barbero, B Vincent, and FJ De Las Nieves. Charge controlled swelling of microgel particles. *Macromolecules*, 33(6):2114–2118, 2000.

[5] Xiaohu Xia and Zhibing Hu. Synthesis and light scattering study of microgels with interpenetrating polymer networks. *Langmuir*, 20(6):2094–2098, 2004.

[6] Shufan Chen, Long Jiang, and Yi Dan. Preparation and thermal response behavior of poly (n-isopropylacrylamide-co-a crylic acid) microgels via soap-free emulsion polymerization based on aibn initiator. *Journal of Applied Polymer Science*, 121(6):3322–3331, 2011.

[7] Nurettin Sahiner, WT Godbey, Gary L McPherson, and Vijay T John. Microgel, nanogel and hydrogel–hydrogel semi-ipn composites for biomedical applications: Synthesis and characterization. *Colloid and Polymer Science*, 284(10):1121–1129, 2006.

[8] Janine Dubbert, Katja Nothdurft, Matthias Karg, and Walter Richtering. Core–shell–shell and hollow double-shell microgels with advanced temperature responsiveness. *Macromolecular Rapid Communications*, 36(2):159–164, 2015.

[9] Ingo Berndt, Jan Skov Pedersen, and Walter Richtering. Temperature-sensitive core–shell microgel particles with dense shell. *Angewandte Chemie*, 118(11):1769–1773, 2006.

[10] Matthias Ballauff. Nanoscopic polymer particles with a well-defined surface: Synthesis, characterization, and properties. *Macromolecular Chemistry and Physics*, 204(2):220–234, 2003.

[11] Janine Dubbert, Tobias Honold, Jan Skov Pedersen, Aurel Radulescu, Markus Drechsler, Matthias Karg, and Walter Richtering. How hollow are thermoresponsive hollow nanogels? *Macromolecules*, 47(24):8700–8708, 2014.

[12] Sarah K Wypysek, Andrea Scotti, Mohammed O Alziyadi, Igor I Potemkin, Alan R Denton, and Walter Richtering. Tailoring the cavity of hollow polyelectrolyte microgels. *Macromolecular Rapid Communications*, 41(1):1900422, 2020.

[13] Andrij Pich, Arpita Karak, Yan Lu, Arnup K Ghosh, and Hans-Juergen P Adler. Preparation of hybrid microgels functionalized by silver nanoparticles. *Macromolecular Rapid Communications*, 27(5):344–350, 2006.

[14] Yue Cui, Cheng Tao, Suping Zheng, Qiang He, Sufen Ai, and Junbai Li. Synthesis of thermosensitive pnipam-co-mbaa nanotubes by atom transfer radical polymerization within a porous membrane. *Macromolecular Rapid Communications*, 26(19):1552–1556, 2005.

[15] Srinivasa Raghavan, Neville Fernandes, and Bani Cipriano. Shape-changing tubular hydrogels. *Gels*, 4:18, 02 2018.

[16] Karg, Isabel Pastoriza-Santos, Benito Rodriguez-Gonzalez, Regine von Klitzing, Stefan Wellert, and Thomas Hellweg. Temperature, pH, and ionic strength induced changes of the swelling behavior of PNIPAM-poly (allylacetic acid) copolymer microgels. *Langmuir*, 24(12):6300–6306, 2008.

[17] Clinton D Jones and L Andrew Lyon. Synthesis and characterization of multiresponsive core-shell microgels. *Macromolecules*, 33(22):8301–8306, 2000.

[18] Qiang Zhang, Juan Colazo, Darren Berg, Samuel M Mugo, and Michael J Serpe. Multiresponsive nanogels for targeted anticancer drug delivery. *Molecular Pharmaceutics*, 14(8):2624–2628, 2017.

[19] Murali Mohan Yallapu, Meena Jaggi, and Subhash C Chauhan. Design and engineering of nanogels for cancer treatment. *Drug Discovery Today*, 16(9-10):457–463, 2011.

[20] Garima Agrawal and Rahul Agrawal. Functional microgels: Recent advances in their biomedical applications. *Small*, 14(39):1801724, 2018.

[21] Claudia Obeso-Vera, Jose M Cornejo-Bravo, Aracely Serrano-Medina, and Angel Licea-Claverie. Effect of crosslinkers on size and temperature sensitivity of poly (n-isopropylacrylamide) microgels. *Polymer Bulletin*, 70(2):653–664, 2013.

[22] Michael Heskins and James E Guillet. Solution properties of poly (n-isopropylacrylamide). *Journal of Macromolecular Science—Chemistry*, 2(8):1441–1455, 1968.

[23] Ying Guan and Yongjun Zhang. PNIPAM microgels for biomedical applications: From dispersed particles to 3d assemblies. *Soft Matter*, 7(14):6375–6384, 2011.

[24] Jacobus Henricus Van't Hoff. The role of osmotic pressure in the analogy between solutions and gases. *Journal of Membrane Science*, 100(1):39–44, 1995.

[25] Rob Phillips, Jane Kondev, Julie Theriot, and Hernan Garcia. *Physical Biology of the Cell*. Garland Science, 2012.

[26] S Hirotsu. Static and time-dependent properties of polymer gels around the volume phase transition. *Phase Transitions: A Multinational Journal*, 47(3-4):183–240, 1994.

[27] Todd Hoare and Robert Pelton. Titrametric characterization of pH-induced phase transitions in functionalized microgels. *Langmuir*, 22(17):7342–7350, 2006.

[28] A Fernández-Nieves, A Fernández-Barbero, B Vincent, and FJ De las Nieves. Osmotic deswelling of ionic microgel particles. *The Journal of Chemical Physics*, 119(19):10383–10388, 2003.

[29] Michal Ilavsky. Phase transition in swollen gels. 2. Effect of charge concentration on the collapse and mechanical behavior of polyacrylamide networks. *Macromolecules*, 15(3):782–788, 1982.

[30] Qiyun Tang and Alan R. Denton. Ion density deviations in semipermeable ionic microcapsules. *Physical Chemistry Chemical Physics*, 17(16):11070–11076, 2015.

[31] M J Murray and M J Snowden. The preparation, characterisation and applications of colloidal microgels. *Advances in Colloid and Interface Science*, 54:73–91, 1995.

[32] Kokkarachedu Varaprasad, Rotimi Sadiku, Koduri Ramam, Jaragula Jayaramudu, and Siva Mohan Reddy. *Chapter 8 - Significances of Nanostructured Hydrogels for Valuable Applications*, pages 273 – 298. 12 2014.

[33] Michael C Wilkinson, John Hearn, and Paul A Steward. The cleaning of polymer colloids. *Advances in Colloid and Interface Science*, 81(2):77–165, 1999.

[34] Toyoichi Tanaka. Collapse of gels and the critical endpoint. *Physical Review Letters*, 40(12):820, 1978.

[35] K Dušek and Donald Patterson. Transition in swollen polymer networks induced by intramolecular condensation. *Journal of Polymer Science Part A-2: Polymer Physics*, 6(7):1209–1216, 1968.

[36] Andrea Scotti, Alan R Denton, Monia Brugnoni, Judith E Houston, Ralf Schweins, Igor I Potemkin, and Walter Richtering. Deswelling of microgels in crowded suspensions depends on cross-link density and architecture. *Macromolecules*, 52(11):3995–4007, 2019.

[37] Andrij Pich and Walter Richtering. Microgels by precipitation polymerization: Synthesis, characterization, and functionalization. In *Chemical Design of Responsive Microgels*, pages 1–37. Springer, 2010.

[38] Sofi Nöjd, Peter Holmqvist, Niels Boon, Marc Obiols-Rabasa, Priti S Mohanty, Ralf Schweins, and Peter Schurtenberger. Deswelling behaviour of ionic microgel particles from low to ultra-high densities. *Soft Matter*, 14(20):4150–4159, 2018.

[39] Alan R Denton and Qiyun Tang. Counterion-induced swelling of ionic microgels. *The Journal of Chemical Physics*, 145(16):164901, 2016.

[40] Gil C Claudio, Kurt Kremer, and Christian Holm. Comparison of a hydrogel model to the Poisson–Boltzmann cell model. *The Journal of Chemical Physics*, 131(9):094903, 2009.

[41] Alan R Denton. Effective interactions and volume energies in charged colloids: Linear response theory. *Physical Review E*, 62(3):3855, 2000.

[42] Alan R Denton. Counterion penetration and effective electrostatic interactions in solutions of polyelectrolyte stars and microgels. *Physical Review E*, 67(1):011804, 2003.

[43] Paul J Flory. *Principles of Polymer Chemistry*. Cornell University Press, 1953.

[44] Manuel Quesada-Pérez, José Alberto Maroto-Centeno, Jacqueline Forcada, and Roque Hidalgo-Alvarez. Gel swelling theories: the classical formalism and recent approaches. *Soft Matter*, 7(22):10536–10547, 2011.

[45] Xianyu Song, Bo Bao, Jiabo Tao, Shuangliang Zhao, Xia Han, and Honglai Liu. Deswelling dynamics of thermoresponsive microgel capsules and their ultrasensitive sensing applications: a mesoscopic simulation study. *The Journal of Physical Chemistry C*, 123(3):1828–1838, 2018.

[46] A Moncho-Jordá. Effective charge of ionic microgel particles in the swollen and collapsed states: The role of the steric microgel-ion repulsion. *The Journal of Chemical Physics*, 139(6):064906, 2013.

[47] Silvia Corezzi, Lucia Comez, and Marco Zanatta. A simple analysis of Brillouin spectra from opaque liquids and its application to aqueous suspensions of poly-n-isopropylacrylamide microgel particles. *Journal of Molecular Liquids*, 266:460–466, 2018.

[48] Karl Kratz, Thomas Hellweg, and Wolfgang Eimer. Influence of charge density on the swelling of colloidal poly (n-isopropylacrylamide-co-acrylic acid) microgels. *Colloids and Surfaces A: Physicochemical and Engineering Aspects*, 170(2-3):137–149, 2000.

[49] Charlotte Pellet and Michel Cloitre. The glass and jamming transitions of soft polyelectrolyte microgel suspensions. *Soft Matter*, 12(16):3710–3720, 2016.

[50] R Borrega, M Cloitre, I Betremieux, B Ernst, and L Leibler. Concentration dependence of the low-shear viscosity of polyelectrolyte micro-networks: From hard spheres to soft microgels. *EPL (Europhysics Letters)*, 47(6):729, 1999.

[51] Dimitris Vlassopoulos and Michel Cloitre. Tunable rheology of dense soft deformable colloids. *Current Opinion in Colloid & Interface Science*, 19(6):561–574, 2014.

[52] Michel Cloitre, Régis Borrega, Fabrice Monti, and Ludwik Leibler. Structure and flow of polyelectrolyte microgels: from suspensions to glasses. *Comptes Rendus Physique*, 4(2):221–230, 2003.

[53] M Pelaez-Fernandez, Anton Souslov, LA Lyon, Paul M Goldbart, and A Fernandez-Nieves. Impact of single-particle compressibility on the fluid-solid phase transition for ionic microgel suspensions. *Physical Review Letters*, 114(9):098303, 2015.

[54] Mitsuhiro Ebara, Yohei Kotsuchibashi, Koichiro Uto, Takao Aoyagi, Young-Jin Kim, Ravin Narain, Naokazu Idota, and John M Hoffman. Smart Hydrogels. In *Smart Biomaterials*, pages 9–65. Springer, 2014.

[55] Ilaria Sanzari, Elena Buratti, Ruomeng Huang, Camelia G Tusan, Franco Dinelli, Nicholas D Evans, Themistoklis Prodromakis, and Monica Bertoldo. Poly (n-isopropylacrylamide) based thin microgel films for use in cell culture applications. *Scientific Reports*, 10(1):1–14, 2020.

[56] Serguei V Vinogradov. Colloidal microgels in drug delivery applications. *Current Pharmaceutical Design*, 12(36):4703–4712, 2006.

[57] Maxim Dirksen, Carina Dargel, Lukas Meier, Timo Brändel, and Thomas Hellweg. Smart microgels as drug delivery vehicles for the natural drug aescin: Uptake, release and interactions. *Colloid and Polymer Science*, pages 1–14, 2020.

[58] Guanyu Hao, Zhi Ping Xu, and Li Li. Manipulating extracellular tumour pH: An effective target for cancer therapy. *RSC Advances*, 8(39):22182–22192, 2018.

[59] Bingyuan Lu, Mark D Tarn, Nicole Pamme, and Theoni K Georgiou. Fabrication of tailorable ph responsive cationic amphiphilic microgels on a microfluidic device for drug release. *Journal of Polymer Science Part A: Polymer Chemistry*, 56(1):59–66, 2018.

[60] Hossein K Heris, Jamal Daoud, Sara Sheibani, Hojatollah Vali, Maryam Tabrizian, and Luc Mongeau. Vocal fold tissue regeneration: Investigation of the viability, adhesion, and migration of human fibroblasts in a hyaluronic acid/gelatin microgel-reinforced composite hydrogel for vocal fold tissue regeneration. *Advanced Healthcare Materials*, 5(2):188–188, 2016.

[61] Dalong Ni, Wenbo Bu, Emily B Ehlerding, Weibo Cai, and Jianlin Shi. Engineering of inorganic nanoparticles as magnetic resonance imaging contrast agents. *Chemical Society Reviews*, 46(23):7438–7468, 2017.

[62] Alan R Denton. Counterion penetration and effective electrostatic interactions in solutions of polyelectrolyte stars and microgels. *Phys. Rev. E*, 67:011804, 2003.

[63] Alan R Denton and Mohammed O Alziyadi. Osmotic pressure of permeable ionic microgels: Poisson-Boltzmann theory and exact statistical mechanical relations in the cell model. *The Journal of Chemical Physics*, 151(7):074903, 2019.

[64] James M Griffin, Ian Robb, and Alexander Bismarck. Preparation and characterization of surfactant-free stimuli-sensitive microgel dispersions. *Journal of Applied Polymer Science*, 104(3):1912–1919, 2007.

[65] Andrij Pich and Walter Richtering. *Chemical Design of Responsive Microgels*, volume 234. Springer, 2010.

[66] Virtanen O L J, Brugnoni M, Kather M, Pich A, and Richtering W. The next step in precipitation polymerization of n-isopropylacrylamide: Particle number density control by monochain globule surface charge modulation. *Polymer Chemistry*, 7(32):5123–5131, 2016.

[67] Zou DM, Ma S, R Guan, M Park, L Sun, J J Aklonis, and R Salovey. Model filled polymers. V. Synthesis of crosslinked monodisperse polymethacrylate beads. *Journal of Polymer Science Part A: Polymer Chemistry*, 30(1):137–144, 1992.

[68] Robert Pelton. Temperature-sensitive aqueous microgels. *Advances in Colloid and Interface Science*, 85(1):1–33, 2000.

[69] X Wu, R H Pelton, A E Hamielec, D R Woods, and W McPhee. The kinetics of poly (n-isopropylacrylamide) microgel latex formation. *Colloid and Polymer Science*, 272(4):467–477, 1994.

[70] Todd Hoare and Robert Pelton. Functional group distributions in carboxylic acid containing poly (n-isopropylacrylamide) microgels. *Langmuir*, 20(6):2123–2133, 2004.

[71] Ingo Berndt, Jan Skov Pedersen, Peter Lindner, and Walter Richtering. Influence of shell thickness and cross-link density on the structure of temperature-sensitive poly-n-isopropylacrylamide- poly-n-isopropylmethacrylamide core- shell microgels investigated by small-angle neutron scattering. *Langmuir*, 22(1):459–468, 2006.

[72] P Hazot, J P Chapel, C Pichot, A Elaissari, and T Delair. Preparation of poly (n-ethyl methacrylamide) particles via an emulsion/precipitation process: The role of the crosslinker. *Journal of Polymer Science Part A: Polymer Chemistry*, 40(11):1808–1817, 2002.

[73] David Duracher, Abdelhamid Elaïssari, and Christian Pichot. Preparation of poly (n-isopropylmethacrylamide) latexes kinetic studies and characterization. *Journal of Polymer Science Part A: Polymer Chemistry*, 37(12):1823–1837, 1999.

[74] Tae Gwan Park and Allan S Hoffman. Synthesis and characterization of pH-and/or temperature-sensitive hydrogels. *Journal of Applied Polymer Science*, 46(4):659–671, 1992.

[75] Qunhui Sun and Yulin Deng. In situ synthesis of temperature-sensitive hollow microspheres via interfacial polymerization. *Journal of the American Chemical Society*, 127(23):8274–8275, 2005.

[76] Janine Dubbert, Katja Nothdurft, Matthias Karg, and Walter Richtering. Core–shell–shell and hollow double-shell microgels with advanced temperature responsiveness. *Macromolecular Rapid Communications*, 36(2):159–164, 2015.

[77] Janine Dubbert, Tobias Honold, Jan Skov Pedersen, Aurel Radulescu, Markus Drechsler, Matthias Karg, and Walter Richtering. How hollow are thermoresponsive hollow nanogels? *Macromolecules*, 47(24):8700–8708, 2014.

[78] Shengqing Xu, Zhihong Nie, Minseok Seo, Patrick Lewis, Eugenia Kumacheva, Howard A Stone, Piotr Garstecki, Douglas B Weibel, Irina Gitlin, and George M Whitesides. Generation of monodisperse particles by using microfluidics: control over size, shape, and composition. *Angewandte Chemie*, 117(5):734–738, 2005.

[79] R H Pelton, H M Pelton, A Morphesis, and R L Rowell. Particle sizes and electrophoretic mobilities of poly (n-isopropylacrylamide) latex. *Langmuir*, 5(3):816–818, 1989.

[80] Henk G Merkus. *Particle Size Measurements: Fundamentals, Practice, Quality*, volume 17. Springer Science & Business Media, 2009.

[81] Hironori Suzuki, Benlian Wang, Ryo Yoshida, and Etsuo Kokufuta. Potentiometric titration behaviors of a polymer and gel consisting of n-isopropylacrylamide and acrylic acid. *Langmuir*, 15(12):4283–4288, 1999.

[82] Ainara Imaz and Jacqueline Forcada. Synthesis strategies to incorporate acrylic acid into n-vinylcaprolactam-based microgels. *Journal of Polymer Science Part A: Polymer Chemistry*, 49(14):3218–3227, 2011.

[83] Niren Murthy, Mingcheng Xu, Stephany Schuck, Jun Kunisawa, Nilabh Shastri, and Jean M J Fréchet. A macromolecular delivery vehicle for protein-based vaccines: Acid-degradable protein-loaded microgels. *Proceedings of the National Academy of Sciences*, 100(9):4995–5000, 2003.

[84] X C Xiao. Effect of the initiator on thermosensitive rate of poly (n-isopropylacrylamide) hydrogels. *EXPRESS Polymer Letters*, 1(4):232–235, 2007.

[85] Xian-Zheng Zhang, Yi-Yan Yang, Fan-Jing Wang, and Tai-Shung Chung. Thermosensitive poly(n-isopropylacrylamide-co-acrylic acid) hydrogels with expanded network structures and improved oscillating swelling—deswelling properties. *Langmuir*, 18(6):2013–2018, 2002.

[86] Todd Hoare and Robert Pelton. Highly pH and temperature responsive microgels functionalized with vinylacetic acid. *Macromolecules*, 37(7):2544–2550, 2004.

[87] Mariano E Brito, Alan R Denton, and Gerhard Nägele. Modeling deswelling, thermodynamics, structure, and dynamics in ionic microgel suspensions. *The Journal of Chemical Physics*, 151(22):224901, 2019.

[88] Alan R Denton. Coarse-grained modeling of charged colloidal suspensions: From Poisson-Boltzmann theory to effective interactions. *Electrostatics of Soft and Disordered Matter*, page 201, 2014.

[89] Andrea Ninarello, Jérôme J Crassous, Divya Paloli, Fabrizio Camerin, Nicoletta Gnan, Lorenzo Rovigatti, Peter Schurtenberger, and Emanuela Zaccarelli. Advanced modelling of microgel structure across the volume phase transition. *arXiv preprint:1901.11495*, 2019.

[90] Matthew Urich and Alan R Denton. Swelling, structure, and phase stability of compressible microgels. *Soft Matter*, 12(44):9086–9094, 2016.

[91] Norman Hoffmann, Christos N Likos, and Hartmut Löwen. Structure and phase behavior of polyelectrolyte star solutions. *The Journal of Chemical Physics*, 121(14):7009–7021, 2004.

[92] Monia Brugnoni, Anne C Nickel, Leif C Kröger, Andrea Scotti, Andrij Pich, Kai Leonhard, and Walter Richtering. Synthesis and structure of deuterated ultra-low cross-linked poly (n-isopropylacrylamide) microgels. *Polymer Chemistry*, 10(19):2397–2405, 2019.

[93] Mary M Hedrick, Jun Kyung Chung, and Alan R Denton. Structure and osmotic pressure of ionic microgel dispersions. *The Journal of Chemical Physics*, 142(3):034904, 2015.

[94] Hideki Kobayashi and Roland G Winkler. Structure of microgels with Debye–Hückel interactions. *Polymers*, 6(5):1602–1617, 2014.

[95] Hideki Kobayashi and Roland G Winkler. Universal conformational properties of polymers in ionic nanogels. *Scientific Reports*, 6(1):1–8, 2016.

[96] U Gasser, A Scotti, and A Fernandez-Nieves. Spontaneous deswelling of microgels controlled by counterion clouds. *Physical Review E*, 99(4):042602, 2019.

[97] Irene Adroher-Benítez, Alberto Martín-Molina, Silvia Ahualli, Manuel Quesada-Pérez, Gerardo Odriozola, and Arturo Moncho-Jordá. Competition between excluded-volume and electrostatic interactions for nanogel swelling: Effects of the counterion valence and nanogel charge. *Physical Chemistry Chemical Physics*, 19(9):6838–6848, 2017.

[98] Irene Adroher-Benítez, Silvia Ahualli, Alberto Martin-Molina, Manuel Quesada-Pérez, and Arturo Moncho-Jorda. Role of steric interactions on the ionic permeation inside charged microgels: Theory and simulations. *Macromolecules*, 48(13):4645–4656, 2015.

[99] David Haložan, Christophe Déjugnat, Milan Brumen, and Gleb B Sukhorukov. Entrapment of a weak polyanion and h+/na+ exchange in confined polyelectrolyte microcapsules. *Journal of Chemical Information and Modeling*, 45(6):1589–1592, 2005.

[100] Weijun Tong, Wenfei Dong, Changyou Gao, and Helmuth Möhwald. Charge-controlled permeability of polyelectrolyte microcapsules. *The Journal of Physical Chemistry B*, 109(27):13159–13165, 2005.

[101] Jun Kyung Chung and Alan R Denton. Effective electrostatic interactions in mixtures of charged colloids. *Phys. Rev. E*, 88:022306, 2013.

[102] P González-Mozuelos. Effective electrostatic interactions among charged thermo-responsive microgels immersed in a simple electrolyte. *The Journal of Chemical Physics*, 144(5):054902, 2016.

[103] Jonas Riest, Priti Mohanty, Peter Schurtenberger, and Christos N Likos. Coarse-graining of ionic microgels: Theory and experiment. *Zeitschrift für Physikalische Chemie*, 226(7-8):711–735, 2012.

[104] Tyler J Weyer and Alan R Denton. Concentration-dependent swelling and structure of ionic microgels: Simulation and theory of a coarse-grained model. *Soft Matter*, 14(22):4530–4540, 2018.

[105] S Förster and Manfred Schmidt. Polyelectrolytes in solution. In *Physical Properties of Polymers*, pages 51–133. Springer, 1995.

[106] Håkan Wennerström and Björn Lindman. Micelles. physical chemistry of surfactant association. *Physics Reports*, 52(1):1–86, 1979.

[107] Xiao-Lin Wang, Toshinori Tsuru, Shin-ichi Nakao, and Shoji Kimura. The electrostatic and steric-hindrance model for the transport of charged solutes through nanofiltration membranes. *Journal of Membrane Science*, 135(1):19–32, 1997.

[108] R A Marcus. Calculation of thermodynamic properties of polyelectrolytes. *The Journal of Chemical Physics*, 23(6):1057–1068, 1955.

[109] Charles Kittel and Paul McEuen. *Introduction to Solid State Physics*, volume 8. Wiley New York, 1976.

[110] Hideki Kobayashi, Rene Halver, Godehard Sutmann, and Roland G Winkler. Polymer conformations in ionic microgels in the presence of salt: Theoretical and mesoscale simulation results. *Polymers*, 9(1):15, 2017.

[111] Jonas Landsgesell and Christian Holm. Cell model approaches for predicting the swelling and mechanical properties of polyelectrolyte gels. *Macromolecules*, 52(23):9341–9353, 2019.

[112] Alberto Martín-Molina and Manuel Quesada-Pérez. A review of coarse-grained simulations of nanogel and microgel particles. *Journal of Molecular Liquids*, 280:374–381, 2019.

[113] Yannick Hallez, Joseph Diatta, and Martine Meireles. Quantitative assessment of the accuracy of the Poisson–Boltzmann cell model for salty suspensions. *Langmuir*, 30(23):6721–6729, 2014.

[114] Håkan Wennerström, Bo Jönsson, and Per Linse. The cell model for polyelectrolyte systems. exact statistical mechanical relations, Monte Carlo simulations, and the Poisson–Boltzmann approximation. *The Journal of Chemical Physics*, 76(9):4665–4670, 1982.

[115] James E Mark et al. *Physical Properties of Polymers Handbook*, volume 1076. Springer, 2007.

[116] Paul J Flory and John Rehner Jr. Statistical mechanics of cross-linked polymer networks i. Rubberlike elasticity. *The Journal of Chemical Physics*, 11(11):512–520, 1943.

[117] Paul J Flory. Molecular theory of rubber elasticity. *Polymer Journal*, 17(1):1–12, 1985.

[118] Carlos G Lopez and Walter Richtering. Does Flory–Rehner theory quantitatively describe the swelling of thermoresponsive microgels? *Soft Matter*, 13(44):8271–8280, 2017.

[119] Markus Deserno and Christian Holm. Cell model and Poisson-Boltzmann theory: A brief introduction. In *Electrostatic Effects in Soft Matter and Biophysics*, pages 27–52. Springer, 2001.

[120] Tomer Markovich, David Andelman, and Rudi Podgornik. Charged Membranes: Poisson-Boltzmann theory, DLVO paradigm and beyond. *arXiv preprint:1603.09451*, 2016.

[121] Alan R Denton. Poisson–Boltzmann theory of charged colloids: Limits of the cell model for salty suspensions. *Journal of Physics: Condensed Matter*, 22(36):364108, 2010.

[122] Sahin Buyukdagli and Ralf Blossey. Beyond Poisson–Boltzmann: Fluctuations and fluid structure in a self-consistent theory. *Journal of Physics: Condensed Matter*, 28(34):343001, 2016.

[123] C N Likos and N W Ashcroft. Self-consistent theory of freezing of the classical one-component plasma. *Physical Review Letters*, 69(2):316, 1992.

[124] Marc Baus and Jean-Pierre Hansen. Statistical mechanics of simple Coulomb systems. *Physics Reports*, 59(1):1–94, 1980.

[125] Setsuo Ichimaru, Hiroshi Iyetomi, and Shigenori Tanaka. Statistical physics of dense plasmas: Thermodynamics, transport coefficients and dynamic correlations. *Physics Reports*, 149(2-3):91–205, 1987.

[126] M J Grimson and M Silbert. A self-consistent theory of the effective interactions in charge-stabilized colloidal dispersions. *Molecular Physics*, 74(2):397–404, 1991.

[127] J Hafner. *From Hamiltonians to Phase Diagrams*. Springer, 1987.

[128] René van Roij, Marjolein Dijkstra, and Jean-Pierre Hansen. Phase diagram of charge-stabilized colloidal suspensions: van der Waals instability without attractive forces. *Physical Review E*, 59(2):2010, 1999.

[129] Hao Wang and Alan R Denton. Effective electrostatic interactions in solutions of polyelectrolyte stars with rigid rodlike arms. *The Journal of Chemical Physics*, 123(24):244901, 2005.

[130] Alan R Denton. Phase separation in charge-stabilized colloidal suspensions: Influence of nonlinear screening. *Physical Review E*, 73(4):041407, 2006.

[131] Robert J Hunter. *Foundations of Colloid Science*. Oxford University Press, 2001.

[132] Dennis C Rapaport and Dennis C Rapaport Rapaport. *The Art of Molecular Dynamics Simulation*. Cambridge University Press, 2004.

[133] S. Plimpton. Fast parallel algorithms for short-range molecular dynamics. *Journal of Physics: Condensed Matter*, 117:1–19, 1995.

[134] Kurt Binder, Dieter Heermann, Lyle Roelofs, A John Mallinckrodt, and Susan McKay. Monte Carlo simulation in statistical physics. *Computers in Physics*, 7(2):156–157, 1993.

[135] Harvey Gould, Jan Tobochnik, and Wolfgang Christian. *An Introduction to Computer Simulation Methods*, volume 1. Addison-Wesley New York, 1988.

[136] Raj Kumar Pathria. *Statistical Mechanics*, volume 45. Pergamon, 1972.

[137] Richard A L Jones. *Soft Condensed Matter*, volume 6. Oxford University Press, 2002.

APPENDIX

This Appendix contains Mathematica notebooks, Java classes, and LAMMPS scripts that we developed for our Poisson-Boltzmann cell model calculations, Monte Carlo simulations, and molecular dynamics simulations.

The below notebook was used to solve the Poisson-Boltzmann equation for a surface-charged microgel in a spherical cell with counterions and salt ions. The microgel was modeled as a surface-charged sphere. Boundary conditions: the electric field is zero at the center and edge of the cell. The electrostatic potential is continuous at the microgel surface.

```
Clear["Global`*"];
λB = 0.714`20; (* Bjerrum length in nm *)
Z = 1000; (* microgel valence = number of osmotically active counterions *)
χ = 0.5; (* Flory-Huggins chi (solvency) parameter *)
a0 = 10; (* dry/collapsed microgel radius in nm *)
Avogadro = 6.0221413`20 * 10^-7; (* 1 microM=6.0221413 10^-7 nm^-3 *)
c0 = 0.001; (* reservoir salt concentration [μM] *)
(* Nmon=((a0^3)/(1.5)^3)*0.63(* number of monomers per microgel *)*)
(* Nch=Nmon*0.0005 (* number of chains per microgel, proportional to number of cross-linkers *)*)
Nmon = 2 * 10^5;
Nch = 100;
γ0 = λB / a0; (* dry electrostatic coupling *)
ϕ0 = 0.01; (* dry/collapsed microcapsule volume fraction *)
ϵ = $MachineEpsilon ;
(*Solve the PB equation inside and outside the microgel
 with boundary conditions at the center and at  outer surface:*)
ps = ParametricNDSolveValue[{ψ''[r] + 2 ψ'[r] / r == κ2 Sinh[ψ[r]], ψ[ϵ] == ψ0, ψ'[ϵ] == 0, WhenEvent[r == 1, ψ'[r] → ψ'[r] + Z γ]},
    {ψ, ψ'}, {r, ϵ, R}, {ψ0, γ, κ2 }, Method → "StiffnessSwitching",
    AccuracyGoal → 20, PrecisionGoal → 40, WorkingPrecision → 40];
(* Loop over the microgel swelling ratio α: *)

Do[
 a = α a0; (* microgel radius *)
 ϕ = α^3 ϕ0; (* microgel volume fraction *)
 R = Rationalize[ϕ^-1/3, 0] ; (* cell radius in a unit of a *)
 γ = Rationalize[λB / (α a0), 0]; (* electrostatic coupling constant *)
 n0 = c0 Avogadro (α a0)^3; (* reduced number density of salt ion pairs by a^3*)
 κ2 = Rationalize[8 π n0 γ, 0]; (* square of reduced screening constant *)
 sol = Quiet@FindRoot[Last[ps[ψ0, γ, κ2 ]][R], {ψ0, -12, 0}, Evaluated → False][[1, 2]];
 (* total number of counterions inside *)
 Ncounterionsin = 4 π n0 NIntegrate[r^2 Exp[-First[ps[sol, γ, κ2 ]][r]], {r, 0, 1}];
 (* total number of coion in the cell *)
 Ncoion = 4 π n0 NIntegrate[r^2 Exp[First[ps[sol, γ, κ2 ]][r]], {r, 0, R}];
 Ncoionin = 4 π n0 NIntegrate[r^2 Exp[First[ps[sol, γ, κ2 ]][r]], {r, 0, 1}];
 (* salt concentration in the cell *)
 csalt = 3 c0 NIntegrate[r^2 Exp[First[ps[sol, γ, κ2 ]][r]], {r, 0, R}];
 (* total number of counterions outside *)
 Ncounterionsout = 4 π n0 NIntegrate[r^2 Exp[-First[ps[sol, γ, κ2 ]][r]], {r, 1, R}];

 pe = γ (Z^2/6 - Z/3 (Ncounterionsin - Ncoionin));
 (* Flory-Rehner approximation for (gel) contribution
   to osmotic pressure inside the microgel [units of kBT/microgel volume] *)
 pg = -Nmon (α^3 Log[1 - 1/α^3] + χ α^-3 + 1) - Nch (α^2 - 1/2);
 ptot = pe + pg ; (* total osmotic pressure *)
 Ntot = Ncounterionsin + Ncounterionsout - Ncoion ; (* total counterions *)
 Print[NumberForm[α, 6], "  ", NumberForm[pg, 10], "  ",
  NumberForm[pe, 10], "  ", NumberForm[ptot, 10], "   " , NumberForm[Ncounterionsin, 10], "  ",
  NumberForm[Ncounterionsout, 10], "  ", NumberForm[Ntot, 10], "  ", NumberForm[Ncoion, 10]];

 Write[file, NumberForm[α, 6], "  ", NumberForm[pg, 10], "  ",
  NumberForm[pe, 10], "  ", NumberForm[ptot, 10], "   ", NumberForm[Ncounterionsin, 10], "  ",
  NumberForm[Ncounterionsout, 10], "  ", NumberForm[Ntot, 10], "   ", NumberForm[Ncoion, 10]];,
 {α, 2.95, 3.2, 0.01} (* loop over swelling ratio *)
]
```

The below notebook was used to solve the Poisson-Boltzmann equation for cylindrical microgels in a cylindrical cell with counterions and salt ions. The microgel was modeled as an infinitely long cylinder with uniform surface charge.

```
ClearAll["Global`*"];
B = 7.14`20; (* Bjerrum length in A *)
a0 = 300; (* cylinder dry radius in A *)
γ0 = B / a0;
ϕ0 = 0.01; (* cylinder volume fraction *)
R = Rationalize[a0 / ϕ0^(1/2), 0]; (* cell radius *)
λ0 = 200; (* reduce charge per unit dry length times dry radius a0 *)
a0R = Rationalize[a0 / R, 0]; (* cylinder dry radius in R *)
c0 = 500; (* concentration of salt reservoir in microM/l *)
n0 = c0 a0^3 6.02214`20*^-10; (* concentration of salt reservoir in a0^-3 *)
(*κ2=Rationalize[8π n0 (γ0/x) ,0];(* Screening constant squared *)*)
rm = 1.5; (* radius of monomer in A *)
Nmon = 0.61 (3 / 4) (a0^3 / rm^3) ; (* number of monomer per dry length times dry radius a0 *)
Nch = Nmon * 0.0005; (* number of chain per dry length times dry radius a0*)
χ = 0.5; (* Flory-Huggins chi (solvency) parameter *)
ϵ = $MachineEpsilon ;
pb = ParametricNDSolveValue[{ψ''[r] + ψ'[r] / r == (8 π n0 γ0 / (a0R)^2) Sinh[ψ[r]],
    ψ[ϵ] == ψ0, ψ'[ϵ] == 0, WhenEvent[r == a0R x, ψ'[r] → ψ'[r] + 2 (γ0 / x) (λ0 / (ϕ0^(1/2) y))]},
   {ψ, ψ'}, {r, ϵ, 1}, {ψ0, x , y}, Method → "StiffnessSwitching", WorkingPrecision → 40];
pb1[ψ0_?NumericQ, x_?NumericQ, y_?NumericQ] := Last[pb[ψ0, x, y]];
sol[x_?NumericQ, y_?NumericQ] := ψ0 /. FindRoot[pb1[ψ0, x, y][1], {ψ0, -41/32, 0}];
Nin[x_?NumericQ, y_?NumericQ] :=
  2 π n0 / (a0R)^3 NIntegrate[r Exp[-First[pb[sol[x, y], x, y]][r]], {r, 0, a0R x}];
Nco[x_?NumericQ, y_?NumericQ] := 2 π n0 / (a0R)^3 NIntegrate[r Exp[First[pb[sol[x, y], x, y]][r]], {r, 0, a0R x}];
Ninn = Quiet[Interpolation[Flatten[ParallelTable[{{x, y}, Nin[x, y]}, {x, 2, 4, 1}, {y, 2, 4, 1}], 1]]];
Ncoin = Quiet[Interpolation[Flatten[ParallelTable[{{x, y}, Nco[x, y]}, {x, 2, 4, 1}, {y, 2, 4, 1}], 1]]];
h = z - x / y ((γ0 / x) λ0 / π) ((x λ0 / (2 y)) - (x ϕ0^(1/2)) (Ninn[x, y] - Ncoin[x, y])) -
   x / (y π) (-Nmon (x^2 y Log[1 - 1 / (x^2 y)] + χ / (x^2 y) + 1) - Nch (x^2 - 1/2));
g = z + x / y ((λ0 (γ0 / x)) / π) Log[x ϕ0^(1/2)] ((x λ0 / y) - 2 x ϕ0^(1/2) (Ninn[x, y] - Ncoin[x, y])) -
   x / (y π) (-Nmon (x^2 y Log[1 - 1 / (x^2 y)] + χ / (x^2 y) + 1) - Nch (y^2 - 1/2));
Quiet[ContourPlot3D[{h == 0, g == 0}, {x, 2, 4}, {y, 2, 4}, {z, 0, 5}, PlotTheme → "Detailed",
  MeshFunctions → {Function[{x, y, z, f}, h - g]}, AxesLabel → {x, y, z}, MeshStyle → {{Thick, Blue}},
  Mesh → {{0}}, ContourStyle → Directive[Orange, Opacity[0.4], Specularity[White, 30]]]]
```

The LAMMPS code below initializes the microions on a Face-centered cubic (FCC) lattice. The script below is a sample LAMMPS input script, used to run the MD simulation.

```
1
2  # Spherical cell model of a surface charged microgel dispersion with explicit
       counterions AND no salt.
3  # Centered spheres, fixed boundary conditions, and doubled Coulomb cutoff!
4  # System parameters: microgel and microion valences, microgel and cell radii
5  units           real
6  timestep        1
7  atom_style      charge
8  dimension       3
9
10 # Microgel valence (NOTE: electroneutrality requires Z/q = counterion number)
11 variable Z equal 1000
12
13 # Counterion valence:
14 variable q equal 1
15
16 # Microgel radius (real units):
17 variable a equal 250
18
19
20 # Microgel volume fraction:
21 #variable phi equal ($a/$R)^3 or (phi0)(alpha)^3
22 variable phi equal 0.3125
23
24 # Cell radius (real units):
25 #variable R  equal 500
26 variable R equal $a/${phi}^(1./3.)
27
28 # Microgel volume fraction:
29 #variable phi equal ($a/$R)^3
30
31 # Lattice constant (real units):
32 variable L equal 55
33
```

```
# Cell radius (lattice units):
variable Rc equal $R/$L

# Initial radius (lattice units):
variable Ri equal 0.61*${Rc}

# Microgel radius (lattice units):
variable Rm equal $a/$L
# Pair potential cutoff radius (real units):
variable Rcut equal 2*$R

# Force unit conversion:
# epsilon=80:
variable C equal 4.1508
# epsilon=78:
#variable C equal 4.257

lattice         fcc $L
#lattice         bcc $L

# Fixed boundary conditions on cubic simulation cell
boundary f f f

#region ID style args; style = sphere; args = x y z radius
region          sphere1in sphere ${Rc} ${Rc} ${Rc} ${Rm} side in
region          sphere1out sphere ${Rc} ${Rc} ${Rc} ${Rm} side out
region          sphere2 sphere ${Rc} ${Rc} ${Rc} ${Ri} side in
region          sphere3 sphere ${Rc} ${Rc} ${Rc} ${Rc} side in

#create_box N region-ID; N = # of atom types
create_box      2 sphere3

#create_atoms type style; type = atom type; style = region args = region-ID
#fcc lattice:
create_atoms    1 region sphere2 basis 1 1 basis 2 1 basis 3 1 basis 4 1
#bcc lattice:
```

```
#create_atoms    1 region sphere2 basis 1 1 basis 2 2

#set counterions number
set      atom 1*1000 type 1
set      atom 1001*5000 type 2

group counterion type 1
group extra type 2
delete_atoms group extra

# set mass of atoms for atom_style charge
mass            1 1.0
mass            2 1.0
#set             type 1 mass 1

# set charge of atoms for atom_style charge
set   type 1 charge $q
set   type 2 charge $q




velocity        all create 293.0 87287

# Hybrid pair potential: repulsive LJ potential, cut off at minimum [rcut=sigma
   *2^(1/6)]
# and Coulomb potential cut off at twice the cell radius:
#pair_style      hybrid/overlay lj/cut 1.122462048 coul/cut ${Rcut}
#pair_style      hybrid/overlay lj/cut 2.244924096 coul/cut ${Rcut}
pair_style      hybrid/overlay lj/cut 3.367386145 coul/cut ${Rcut}
# parameters: epsilon, sigma=rcut/2^(1/6)
#pair_coeff      * * lj/cut 30. 1.
#pair_coeff      * * lj/cut 30. 2.
pair_coeff      * * lj/cut 30. 3.
pair_modify shift yes
pair_coeff      * * coul/cut ${Rcut}
```

```
105 dielectric      80.
106 #dielectric      78.
107
108 neighbor        0.3 bin
109 neigh_modify    every 20 one 50000 delay 0 check no  page 1000000
110
111 #variable fx1in atom -($C*$Z*$q/$a^3)*(x-$R)
112 #variable fy1in atom -($C*$Z*$q/$a^3)*(y-$R)
113 #variable fz1in atom -($C*$Z*$q/$a^3)*(z-$R)
114 #variable fx2in atom ($C*$Z*$q/$a^3)*(x-$R)
115 #variable fy2in atom ($C*$Z*$q/$a^3)*(y-$R)
116 #variable fz2in atom ($C*$Z*$q/$a^3)*(z-$R)
117
118 variable r3 atom ((x-$R)^2+(y-$R)^2+(z-$R)^2)^1.5+1.e-20
119
120 variable fx1out atom -($C*$Z*$q/v_r3)*(x-$R)
121 variable fy1out atom -($C*$Z*$q/v_r3)*(y-$R)
122 variable fz1out atom -($C*$Z*$q/v_r3)*(z-$R)
123 #variable fx2out atom ($C*$Z*$q/v_r3)*(x-$R)
124 #variable fy2out atom ($C*$Z*$q/v_r3)*(y-$R)
125 #variable fz2out atom ($C*$Z*$q/v_r3)*(z-$R)
126
127 #fix             1 counterion addforce v_fx1in v_fy1in v_fz1in region sphere1in
128 #fix             2 coion addforce v_fx2in v_fy2in v_fz2in region sphere1in
129 fix             3 counterion addforce v_fx1out v_fy1out v_fz1out region
      sphere1out
130 #fix             4 coion addforce v_fx2out v_fy2out v_fz2out region sphere1out
131
132 fix             5 all nvt temp 293.0 293.0 100.0
133 fix             6 all wall/region sphere3 lj126 30 1 1.122462048
134
135 dump            1 all atom 1000 dump.surface_charged_microgel_op_0.02
      _1000_alpha_2.5
136 thermo          1000
137 run             10000000
```

The Java code below was used to compute the bulk osmotic pressure and swelling ratio of surface-charged microgel suspensions in our Monte Carlo simulations.

```
  calculateTotalEnergy(); // initial energy
 }

 /**
 * Place particles on sites of an fcc lattice.
 */
 public void setFCCPositions() {
  int ix, iy, iz;
  double dnx = Math.cbrt(N/4.);
  d = side / dnx; // lattice constant
  nx = (int) dnx;
  if (dnx - nx > 0.00001) {
   nx++; // N/4 is not a perfect cube
  }

  int i = 0;
  for (ix = 0; ix < 2*nx; ix++) { // loop through particles in a row
   for (iy = 0; iy < 2*nx; iy++) { // loop through particles in a column
    for (iz = 0; iz < 2*nx; iz++) { // loop through particles in a layer
     if (i < N) { // check for remaining particles
      if ((ix+iy+iz)%2 == 0) { // check for remaining particles
      x[i] = ix * d/2.;
      y[i] = iy * d/2.;
      z[i] = iz * d/2.;
      i++;
     }
    }
   }
  }
 }
 calculateTotalEnergy(); // initial energy
}

/**
```

```
* Do a Monte Carlo simulation step.
*/
public void step() {
 steps++;
 double dxtrial, dytrial, dztrial, atrial;
 double newEnergy, HertzEnergy;
 double dx, dy, dz, de, r, r2, sigma, aMean, R;
 double vbare, vind, voverlap, A, YukawaEnergy;
 double a3, mixF, elasticF, elecF, totalF, selfU, volU, K, ka;

 // trial move
 for (int i = 0; i < N; ++i) {

  dxtrial = tolerance*2.*(Math.random()-0.5);
  dytrial = tolerance*2.*(Math.random()-0.5);
  dztrial = tolerance*2.*(Math.random()-0.5);
  atrial = atolerance*2.*(Math.random()-0.5);

  x[i] = PBC.position(x[i]+dxtrial, side); // trial displacement
  y[i] = PBC.position(y[i]+dytrial, side);
  z[i] = PBC.position(z[i]+dztrial, side);
  a[i] += atrial; // trial radius change

  newEnergy = 0;

  for (int j = 0; j < N; ++j) {
   if(j != i) {
    dx = PBC.separation(x[i]-x[j], side);
    dy = PBC.separation(y[i]-y[j], side);
    dz = PBC.separation(z[i]-z[j], side);
    r2 = dx*dx+dy*dy+dz*dz;
    r = Math.sqrt(r2);
    sigma = a[i] + a[j];
    aMean = 0.5*sigma;
    R = r/aMean;
    ka = k*aMean;
```

```
71      if (r < sigma){
72
73       // CHANGE vbare and vind: [Mohammed Alziyadi]
74       // For surface-charged microgel
75       voverlap = Z*Z*gamma*(1-Math.exp(-k*r)-Math.exp(-2*ka)*Math.sinh(k*r))/(2*
    ka*ka*r);
76
77       HertzEnergy = B*Math.pow(1-r/sigma,2.5);
78       newEnergy += voverlap + HertzEnergy; // pair energy
79       newPairEnergy[i][j] = voverlap + HertzEnergy;
80      }
81      else {
82       // CHANGE A: [Mohammed Alziyadi]
83       //  A = gamma*Math.pow(Z*Math.sinh(k*a[i])/(k*a[i]),2);
84       A = gamma*(Z*Math.sinh(k*a[i])/(k*a[i]))*(Z*Math.sinh(k*a[j])/(k*a[j]));
85       YukawaEnergy = A*Math.exp(-k*r)/r;
86       newEnergy += YukawaEnergy; // pair energy
87       newPairEnergy[i][j] = YukawaEnergy;
88      }
89     }
90    }
91    a3 = Math.pow(a[i],3);
92    mixF = nMon*((a3-1)*Math.log(1-1/a3)+chi*(1-1/a3));
93    elasticF = 1.5*nChains*(a[i]*a[i]-Math.log(a[i])-1);
94
95    K = k*a[i]; // screening constant (units of inverse swollen radius)
96    // CHANGE selfU and volU:  [Mohammed Alziyadi]
97
98    //
99    selfU = 0.5*Z*Z*gamma/a[i]; // self energy of a single ionic microgel for
     surface-charged
100 [Mohammed Alziyadi]
101
102   // microion volume energy (neglecting constants independent of a[i])
103   // For surface-charged microgel : [Mohammed Alziyadi]
104
```

```
105    volU = -0.5*gamma*Z*Z*(Math.exp(-2*K)-1+2*K)/(2*K*a[i]);
106    elecF = selfU + volU; // electrostatic free energy
107
108    totalF = mixF + elasticF + elecF; // single-particle free energy
109    newEnergy += totalF;
110
111    de = newEnergy-energy[i];
112
113    if(Math.exp(-de) < Math.random() || a[i] < 1) {
114     x[i] = PBC.position(x[i]-dxtrial, side); // reject move
115     y[i] = PBC.position(y[i]-dytrial, side);
116     z[i] = PBC.position(z[i]-dztrial, side);
117     a[i] -= atrial;
118    }
119    else { // accept move and update energies
120     energy[i] = newEnergy;
121     for (int j = 0; j < N; ++j) { // update energies of other particles
122      if(j != i) {
123       energy[j] += newPairEnergy[i][j]-pairEnergy[i][j];
124       pairEnergy[i][j] = newPairEnergy[i][j];
125       pairEnergy[j][i] = newPairEnergy[i][j];
126      }
127     }
128    }
129   }
130   calculateTotalEnergy(); // new total energy
131  }
132
133  // total energy and pressure
134  public void calculateTotalEnergy() {
135   double dx, dy, dz, r, r2, sigma, aMean, R;
136   double vbare, vind, voverlap, A, YukawaEnergy;
137   double a3, mixF, elasticF, elecF, totalF, selfU, volU, volP, K, ka;
138   double fOverR, fx, fy, fz;
139   double fbare, find, foverlap;
140   double derivPart, HertzEnergy;
```

```
141   double pairEnergySum, energySum, virial1, virial2, virialSum;
142
143   totalEnergy = 0;
144   totalVirial = 0;
145
146   for(int i = 0; i < N; ++i) { // sum over particles
147    pairEnergySum = 0;
148    energySum = 0;
149    virialSum = 0;
150    for(int j = 0; j < N; ++j) { // sum over pairs of particles
151     if(j != i) {
152      dx = PBC.separation(x[i]-x[j], side);
153      dy = PBC.separation(y[i]-y[j], side);
154      dz = PBC.separation(z[i]-z[j], side);
155      r2 = dx*dx+dy*dy+dz*dz;
156      r = Math.sqrt(r2);
157      sigma = a[i]+ a[j];
158      aMean = 0.5*sigma;
159      R = r/aMean;
160      ka = k*aMean;
161      if (r < sigma){
162
163       // CHANGE vbare and vind:
164 [Mohammed Alziyadi]
165
166
167       voverlap = Z*Z*gamma*(1-Math.exp(-k*r)-Math.exp(-2*ka)*Math.sinh(k*r))/(2*
    ka*ka*r);
168       // CHANGE fbare and find: [Mohammed Alziyadi]
169
170
171       //  foverlap = 0;
172       foverlap = -Z*Z*gamma*(-1+Math.exp(-k*r)*(1+k*r)+Math.exp(-2*ka)*(-k*r*
    Math.cosh(k*r)+Math.sinh(k*r)))/(2*ka*ka*r*r);
173
174
```

```
175       derivPart = B*Math.pow(1-r/sigma,1.5);
176       HertzEnergy = derivPart*(1-r/sigma);
177       pairEnergy[i][j] = voverlap + HertzEnergy; // pair energy of particles i
    and j
178       pairEnergySum += voverlap + HertzEnergy; // total pair energy of particle
    i
179       fOverR = ((2.5/sigma)*derivPart+foverlap)/r;
180       fx = fOverR*dx; // force in x-direction
181       fy = fOverR*dy; // force in y-direction
182       fz = fOverR*dz; // force in z-direction
183       virial1 = (dx*fx+dy*fy+dz*fz)/3.; // standard virial contribution to
    pressure
184       // contribution from density-dependent effective electrostatic pair
    potential
185       // CHANGE virial2: [Mohammed Alziyadi]
186       virial2 = -(Z*Z*gamma/(2*r))*((1-Math.exp(-r*k)-Math.exp(-2*ka)*Math.sinh(
    r*k))/(ka*ka)-(Math.exp(-r*k)*k*r-Math.exp(-2*ka)*k*r*Math.cosh(k*r)+2*ka*
    Math.exp(-2*ka)*Math.sinh(r*k))/(2*ka*ka));
187       //  virial2 = 0;
188       virialSum += virial1 + virial2;
189      }
190      else {
191
192       A = gamma*(Z*Math.sinh(k*a[i])/(k*a[i]))*(Z*Math.sinh(k*a[j])/(k*a[j]));
193       YukawaEnergy = A*Math.exp(-k*r)/r;
194       pairEnergy[i][j] = YukawaEnergy; // pair energy of particles i and j
195       pairEnergySum += YukawaEnergy; // pair energy
196       fOverR = (YukawaEnergy/r)*(k+1/r);
197       fx = fOverR*dx; // force in x-direction
198       fy = fOverR*dy; // force in y-direction
199       fz = fOverR*dz; // force in z-direction
200       virial1 = (dx*fx+dy*fy+dz*fz)/3.; // standard virial contribution to
    pressure
201       // contribution from density-dependent effective electrostatic pair
    potential
202       // CHANGE virial2: [Mohammed Alziyadi]
```

```
203       virial2 =Z*Z*gamma*Math.exp(-k*r)*(Math.sinh(ka)*Math.cosh(ka)/(ka*r)-Math
    .pow(Math.sinh(ka),2)/(ka*ka*r)-Math.pow(Math.sinh(ka),2)*k/(2*ka*ka));
204       // virial2 = 0;
205       virialSum += virial1 + virial2;
206      }
207     }
208   } // end of j loop over particles
209
210   virialSum *= 0.5; // correct for double-counting pairs
211
212   a3 = Math.pow(a[i],3);
213   mixF = nMon*((a3-1)*Math.log(1-1/a3)+chi*(1-1/a3));
214   elasticF = 1.5*nChains*(a[i]*a[i]-Math.log(a[i])-1);
215
216   K = k*a[i]; // screening constant (units of inverse swollen radius)
217   // CHANGE selfU and volU:
218
219   selfU = 0.5*Z*Z*gamma/a[i]; // self energy of a single ionic microgel for
    surface-charged
220   // microion volume energy (neglecting constants independent of a[i])
221   // For surface-charged microgel
222   volU = -0.5*gamma*Z*Z*(Math.exp(-2*K)-1+2*K)/(2*K*a[i]);
223   //
224   elecF = selfU + volU; // electrostatic free energy
225
226   totalF = mixF + elasticF + elecF; // single-particle free energy
227
228   energy[i] = pairEnergySum + totalF;
229   energySum += 0.5*pairEnergySum + totalF; // correcting for double-counting
    pairs
230
231   // microion volume pressure
232   // CHANGE volP: [Mohammed Alziyadi]
233   volP = -0.5*Z*Z*gamma*Math.exp(-2*K)*(-1+Math.exp(2*K)-2*K)/(4*K*a[i])+Z+2*
    Nsalt;                          // added ideal-gas constribution in the
    above line.
```

```
234   //       volP = -0.5*Z*Z*gamma*Math.exp(-2*K)*(-1+Math.exp(2*K)-2*K)/(4*K*a[i
       ]);
235   virialSum += volP;
236     if (steps>delay){   // collect statistics after equilibrati.
237    totalEnergy += energySum;
238    totalVirial += virialSum;
239   }
240
241  }
242  // [Mohammed Alziyadi]
```